e-ISSN: 3048-460X

CNS&E Current Natural Sciences & Engineering

Peer-reviewed, Multidisciplinary Journal

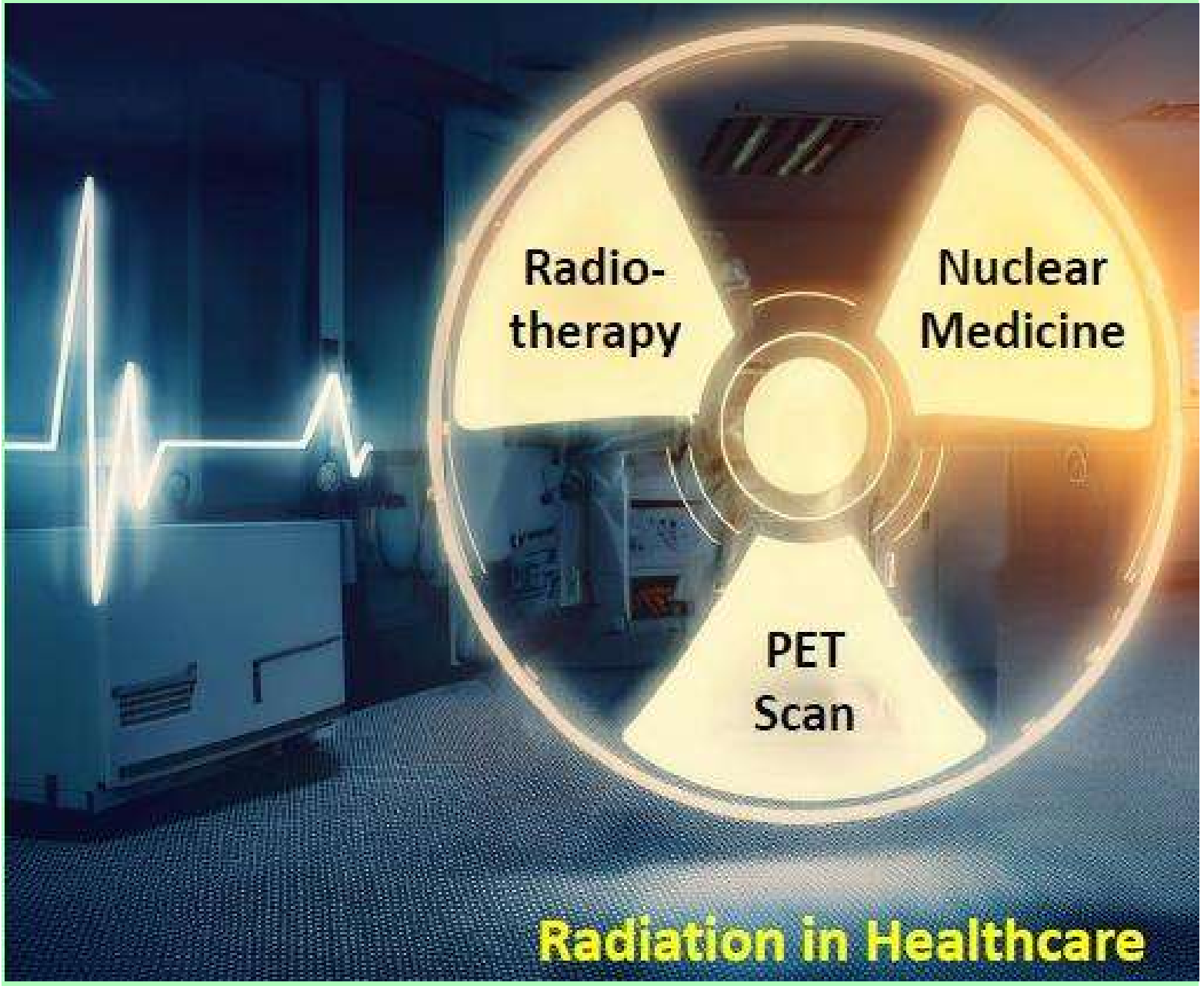

http://doi.org/10.63015/cnse-2024.1.4

Volume 1 Issue 4, July 2024

About CNS&E

Current Natural Sciences & Engineering (CNS&E) Journal publishes new, innovative and cutting-edge research in Natural sciences including physical, chemical, biological, agricultural and environmental sciences, metrology, and other related interdisciplinary fields. Scientific research results in the form of high-quality manuscripts, review articles, mini-reviews, reports, news and short communications are highly welcome.

CNS&E is a hybrid, bimonthly, multidisciplinary journal published by the Vigyanvardhan Blessed Foundation (VBF), a non-profit organization working to disseminate science for the betterment of society.

Scope: CNS&E journal has a broad multidimensional scope. It publishes research in the areas of:

- ❑ Hydrogen & Renewable Energy
- ❑ Environmental Sciences & Hydroelectric Cell
- ❑ Artificial Intelligence Convergence in S&T
- ❑ Net Carbon Zero &Earth Sustainability
- ❑ Condensed Matter & Nanomaterials
- ❑ Health Science & Technology
- ❑ Nuclear Science: Health & Society
- ❑ Measurement Science & Industrial Research
- ❑ Digital & Sustainable Agriculture
- ❑ Smart Engineering Materials & Sensors

Publication Policy: The journal maintains integrity and high ethical values. Submitted manuscripts are peer-reviewed and evaluated for novel scientific content irrespective of its origin. The information about a submitted manuscript will be confidential and will not be disclosed other than Chief Editor, editorial staff, corresponding author, reviewers, and the publisher. The journal ensures that any unpublished work must not be used in Editor's, and reviewer's own research without the explicit written consent of the author(s).

Publication Decisions: The Chief Editor of the journal is responsible for deciding the publication or rejection of the submitted manuscript. The Chief Editor may take suggestion with other editors or reviewers in making decision.

Publisher: VB Foundation

CNS&E Editorial Board

CNS&E Volume 1, Issue 4, July 2024

Table of contents:

Guest Editorial

DAE's Leadership in Advancing National Healthcare through Ionizing Radiation

Dinesh K Aswal* and Anirudh Chandra

Health, Safety and Environment Group
Bhabha Atomic Research Center, Trombay, Mumbai 400085

** Email: dkaswal@yahoo.com*

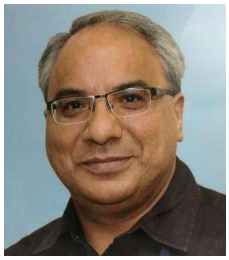

Dr. Dinesh K Aswal

Introduction: Ionizing radiation and nuclear medicine (i.e., use of radioactive substances known as radionuclides) are integral to modern healthcare, offering critical tools for diagnosing, treating, and managing a wide range of medical conditions, significantly enhancing patient care and outcomes. These technologies are indispensable in the fight against cancer, supporting everything from screening and detection to diagnosis, treatment, and palliative care. Beyond oncology, they are equally crucial for diagnosing and treating a wide range of conditions, including cardiovascular and neurological diseases, through routine medical imaging and advanced treatments. In developed countries, which represent about a quarter of the global population, approximately one in 50 people undergo diagnostic nuclear medicine procedures annually [1]. Globally, over 10,000 hospitals use radioisotopes for medical applications, with around 90% of these procedures dedicated to diagnosis. In contrast, therapeutic use of radioisotopes is less frequent, occurring at about one-tenth the rate of diagnostic procedures. This editorial explores the role of the Department of Atomic Energy (DAE) in advancing healthcare through the use of ionizing radiation in the country.

Historical Evolution of Nuclear Medicine: Dr. Homi Jehangir Bhabha, the founding father of India's nuclear program, played a pivotal role in the formation of the Atomic Energy Commission (AEC) in 1948. The growth of nuclear medicine in India is deeply intertwined with its atomic energy program. In 1954, Dr. Bhabha founded the Atomic Energy Establishment, Trombay (AEET), which was renamed Bhabha Atomic Research Centre (BARC) in 1967. BARC developed India's first research reactor, APSARA, became operational in 1956, followed by the CIRUS reactor in 1960. These reactors enabled the indigenous production of medical radionuclides like ^{131}I, ^{32}P, and ^{51}Cr, particularly enhancing clinical research with radioiodine (^{131}I). Through its extensive R&D efforts, BARC started producing and supplying radioisotopes and radiopharmaceuticals to Indian hospitals in the early 1960s. Since 1989, the Board of Radiation and Isotope Technology (BRIT) has become a key supplier of nuclear medicine throughout India. Dr. Bhabha also established a radioisotope laboratory near Grant Medical College in Byculla and secured space at Tata Memorial Hospital for the Radiation Medicine Centre (RMC), a division of BARC, which was inaugurated on September 3, 1963. Dr. K.N. Jeejeebhoy was appointed as the head, with Dr. R.D. Ganatra, Dr. S.M. Sharma, and Dr. H. DaCosta as the first physicians [2]. Nobel Laureate Dr. Ernest Lawrence donated the initial instruments for the facility. Concurrently, in 1956, the Ministry of Defence established the Radiation Cell at Safdarjung Hospital in Delhi for biomedical research using radioisotopes, led by Lt. Col. Dr. S.K. Mazumdar [2]. This eventually led to the creation of the Institute of Nuclear Medicine and Allied Sciences (INMAS), with the foundation stone laid in 1961 and the official dedication in 1964. The RMC has evolved into a premier R&D center for nuclear medicine and was the first in the country to install a medical cyclotron in 2002. Since then, many medical cyclotrons have been established across India, producing vital radioisotopes for diagnostic and therapeutic nuclear medicine procedures. Figure 1 provides an overview of how ionizing radiation and radioisotopes are generated, processed, and used in healthcare applications.

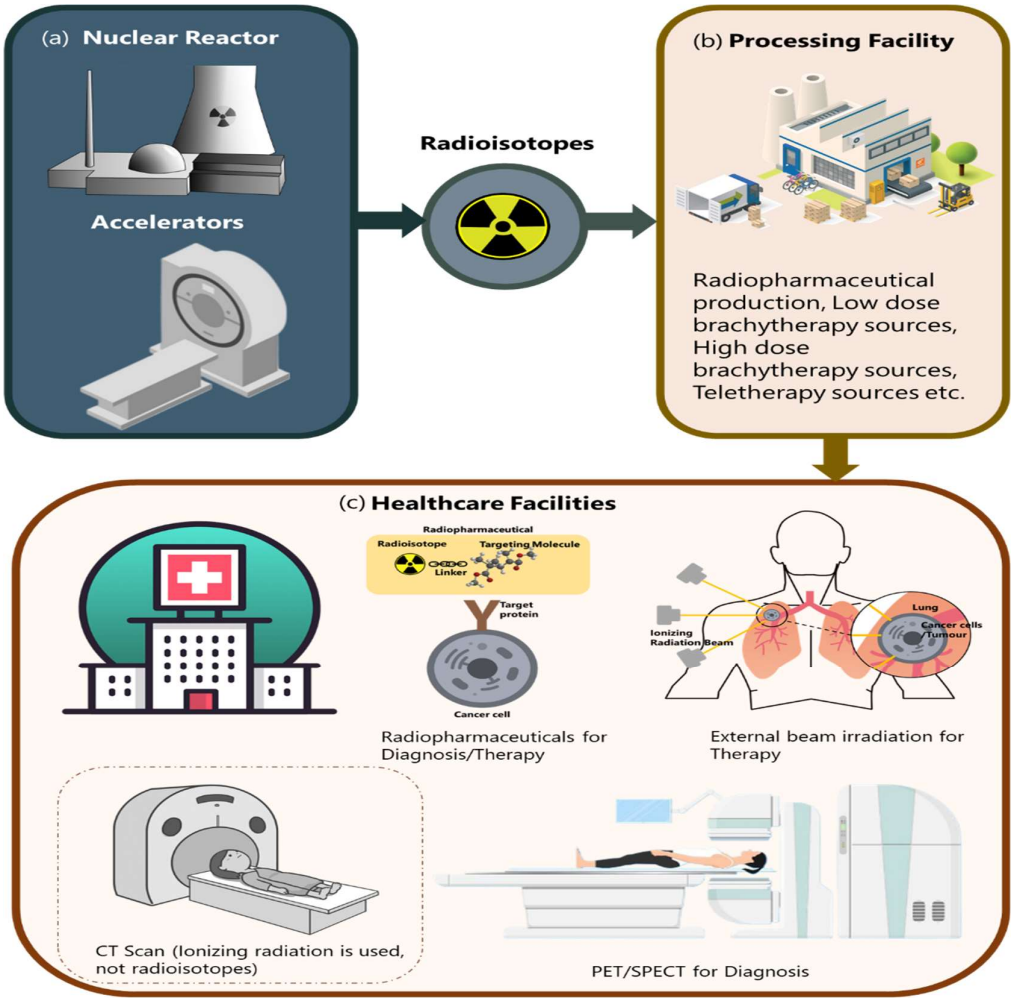

Figure 1. An illustration of how radioisotopes are produced, processed and used in healthcare. (a) Shows where radioisotopes are produced – either in nuclear reactors, such as Dhruva at BARC or accelerators – for their production for healthcare applications. (b) These radioisotopes need to be processed into usable products such as radiopharmaceuticals, brachytherapy sources, teletherapy sources etc. This happens at processing facilities such as BRIT. (c) Once processed, the various products are supplied to healthcare facilities for their varied uses as depicted in figure.

Ionizing Radiation for Diagnosis: Quality healthcare depends on accurate diagnosis and effective treatment assessment, with radiation imaging playing a vital role in this process. Diagnosis can be approached in two primary ways: externally, using ionizing radiation in diagnostic radiology, or internally, through radioisotopes introduced into the body, known as diagnostic nuclear medicine [3]. **Radiography**, a common diagnostic radiology tool, uses X-rays to capture images of bones, vessels, soft tissues, and organs. It is particularly useful for assessing the respiratory system for conditions such as tuberculosis, pneumonia, and lung diseases, as well as cardiac issues like cardiomegaly and pericardial effusions. Radiography is also critical for early fracture detection, especially in emergency and ICU settings where patient mobility is limited. **Mammography**, another key diagnostic technique, employs X-ray imaging of the breast for early breast cancer detection. It is also used to evaluate breast pathologies and monitor patients undergoing breast cancer treatment. Similarly, fluoroscopy provides real-time X-ray imaging of organs or structures, offering lower radiation doses compared to CT scans. Although it provides less detailed images, fluoroscopy is valuable for both diagnostic and therapeutic procedures. **Computed Tomography (CT)** scans use X-rays to create cross-sectional images of the body. A CT scanner consists of an X-ray source and detectors that rotate around the patient to produce

detailed images. CT scans are crucial in trauma cases for identifying intracranial bleeds, brain damage, fractures, and internal injuries not visible externally. They are also invaluable in oncology for locating tumors and assessing their relationship to surrounding structures, aiding in treatment planning. **Diagnostic Nuclear Medicine** on the other hand involves administering radioisotope-labelled pharmaceuticals to patients for diagnostic or therapeutic purposes. Diagnostic tracers typically use gamma-emitting radionuclides like technetium-99m (^{99m}Tc) or positron-emitting ones like fluorine-18 (^{18}F). These radiopharmaceuticals localize to specific organs, emitting radiation from within the body that can be detected using radiation detectors. This principle underlies many nuclear imaging procedures such as positron emission tomography (PET) and single-photon emission computerized tomography (SPECT). The metabolic tracer ^{18}F fluorodeoxyglucose (FDG) has become essential in PET imaging, particularly in oncology.

Ionizing Radiation for Therapy: Radiation therapy utilizes high-energy ionizing radiation to damage the DNA of cancer cells, preventing them from dividing and growing. It can be delivered externally through machines that direct radiation from outside the body, known as teletherapy, or internally using sealed radioactive sources placed inside or near the tumour, a method called brachytherapy. In contrast, nuclear medicine employs unsealed radioactive drugs, or radiopharmaceuticals, which contain radioisotopes that emit particles such as beta, alpha, or Auger electrons. These drugs are highly targeted to cancer cells and are used for specific therapeutic purposes. Advancements in brachytherapy have paralleled those in external radiation therapy. Early methods involved low-dose rate (LDR) brachytherapy with radium-226 (^{226}Ra) and radon-222 (^{222}Ra) sources, which required several days of treatment and posed challenges related to radiation exposure and disposal. This led to the development of high-dose rate (HDR) brachytherapy using artificially produced radionuclides like Cobalt-60 (^{60}Co) and Iridium-192 (^{192}Ir). HDR brachytherapy significantly reduced treatment time from days to hours and introduced miniature sources and remote after-loading techniques, enhancing safety and efficiency. Today, radiation therapy has expanded beyond treating inoperable tumours. It has become the preferred treatment for cancers of the nasopharynx, anal canal, and cervix, often replacing surgery due to its effectiveness [3]. Targeted radionuclide therapies and theranostics are another avenue of advances in nuclear medicine. These therapies use radiopharmaceuticals that deliver therapeutic doses of radiation—alpha, beta, Auger, or conversion electrons—directly to diseased tissues. By targeting specific biological sites with molecular vectors, these treatments effectively induce cytotoxicity in tumor cells. Recent developments include the use of radionuclides like ^{131}I, ^{32}P, ^{166}Ho, ^{188}Re, ^{177}Lu, and ^{90}Y combined with receptor-targeting or immune-derived vectors to treat various cancers.

Advances have been fuelled by new isotopes produced at the Dhruva reactor at BARC and made available through the BRIT. This has expanded therapeutic options beyond traditional isotopes like ^{131}I and ^{32}P. Most notably, Lutetium-177 (^{177}Lu) has emerged as a key player in radionuclide therapy, providing a powerful alternative to radioiodine and significantly impacting cancer treatment in India. BARC has standardized the production of ^{177}Lu and developed several ^{177}Lu-based treatments, making them a cost-effective option for patients [4]. Additionally, BARC has innovated by sourcing Yttrium-90 (^{90}Y) from Strontium-90 (^{90}Sr) recovered from high-level liquid radioactive waste, demonstrating a successful recovery of valuable resources. The development of a ^{90}Sr-^{90}Y generator and ^{90}Y-based radiopharmaceuticals has advanced clinical cancer treatment options.

Radiation Safety in Healthcare: Safety is a key concern in both nuclear medicine and radiotherapy. For patients, risks are mitigated by precisely calculating radiation doses and employing advanced technologies to minimize exposure to healthy tissues. The principles of radiation protection—time, distance, and shielding—are applied to ensure that radiation exposure remains as low as reasonably achievable (ALARA). Caregivers are also safeguarded through various safety measures. They use shielding devices, maintain a safe distance from radiation sources, and limit their exposure time. Strict safety protocols and comprehensive training are implemented to protect both caregivers and patients from unnecessary radiation. Regulatory bodies such as the Atomic Energy Regulatory Board (AERB) and international organizations like the International Commission on Radiological Protection (ICRP) establish standards and limits to ensure safety from radiation hazards in medical settings. In addition to regulations, trained experts in medical physics and radiation safety are essential for ensuring safe

radiation exposure in healthcare. The DAE supports this critical need by offering diploma in radiological physics and other radiation safety certification courses. Graduates of these programs become medical physicists in nuclear medicine centres, radiation safety officers at various facilities, and expert technicians in radiography instrumentation, among other health-care related employment opportunities.

Current State of Nuclear Medicine and Future Requirements: BRIT, a unit of the DAE, provides various products for nuclear medicine, including ^{99}Mo/^{99m}Tc generators, radioiodine, ^{177}Lu, ^{153}Sm, and cold kits for scintigraphy studies. Despite these efforts, there is an increasing reliance on imported supplies for ^{99}Mo/^{99m}Tc generators and certain therapeutic radiopharmaceuticals such as ^{177}Lu PSMA and 177Lu DOTATATE, which are used to treat prostate and neuroendocrine tumors [5]. Many major centers continue to depend on these imported resources. Additionally, ^{68}Ge/^{68}Ga generators, Thallium-201 (^{201}Tl), and alpha emitters are not produced domestically and are fully imported for PET and SPECT imaging and therapy. The demand for these isotopes is anticipated to rise significantly due to their growing use in cancer treatment.
In 2018, BARC enhanced its radioisotope production capabilities by upgrading the APSARA(U) reactor, which now produces key theranostic radioisotopes such as ^{64}Cu. Despite this, high costs and dependence on imported radioisotopes have hindered the advancement of alpha therapy in India. To address this issue, the DAE has proposed a new nuclear reactor for isotope production through a public-private partnership, aimed at advancing nuclear medicine and making radionuclide therapies more affordable for cancer patients [5]. Additionally, to address global shortages of ^{99}Mo affecting gamma imaging, India is developing a LINAC-based system to produce ^{99}Mo as an alternative. The BRIT has also set up a Fission Moly Plant to produce high-specific-activity ^{99}Mo domestically, thereby improving the country's self-reliance in nuclear medicine.

Over time, the leadership of the DAE in nuclear medicine has led to significant advancements in research on new radiopharmaceuticals and the establishment of a comprehensive network of diagnostic and therapeutic centers. Currently, India has 520 operational nuclear medicine centers, which include 24 medical cyclotrons, over 350 PET-CT scanners, 2 proton therapy machines, and more than 150 high-dose radionuclide therapy facilities. However, to address the needs of India's large population, these facilities will need to undergo further rapid expansion and enhanced in-house R&D. This effort includes advancements in equipment development and interdisciplinary research into AI-enabled theranostics, which combines therapy and diagnostics. With focused R&D and strategic planning, India is expected to achieve self-reliance in nuclear medicine by 2047, in line with the vision of Viksit Bharat.

References:
[1] World Nuclear Association, "Radioisotopes in Medicine," World Nuclear Association, 30 April 2024. [Online]. Available: https://world-nuclear.org/information-library/non-power-nuclear-applications/radioisotopes-research/radioisotopes-in-medicine. [Accessed 18 July 2024].
[2] A. R. Sharma, "Nuclear Medicine in India: A Historical Journey," Indian Journal of Nuclear Medicine, vol. 33, pp. S5-10, 2018.
[3] S. Banerjee, S. Basu, A. D. Baheti, S. Kulkarni, V. Rangarajan, P. Nayak, V. Murthy, A. Kumar, S. G. Laskar, J. P. Agarwal, S. Gupta and R. A. Badwe, "Radiation and radioisotopes for human healthcare applications," Current Science, vol. 123, no. 3, pp. 388-395, 2022.
[4] The Economic Times, "BARC develops radionuclides for inoperable cancers, arthritis," The Economic Times, 18 August 2010. [Online]. Available: https://economictimes.indiatimes.com/industry/healthcare/biotech/barc-develops-radionuclides-for-inoperable-cancers-arthritis/articleshow/6329863.cms?from=mdr. [Accessed 18 July 2024].
[5] B. Singh, G. Sahani, V. Prasad, A. Watts and R. Kumar, "India's Growing Nuclear Medicine Infrastructure and Emergence of Radiotheranostics in Cancer Care: Associated Challenges and the Opportunities to Collaborate," Indian Journal of Nuclear Medicine, vol. 38, no. 3, 2023.

Application of Internet of Things Technologies for Automation and Quality Enhancement in Radiological Metrology

K. Sreekumar*, S. K. Jha, Jaison T John, M. Harikumar

Health Physics Division, Bhabha Atomic Research Centre, Mumbai 400 085

Volume 1, Issue 4, July 2024
Received:4 April, 2024; Accepted: 24 June, 2024
DOI: https://doi.org/10.63015/6H-2424.1.4

**Corresponding Author Email: ksreekumar@barc.gov.in*

Abstract: Automation refers to the application of technology that reduces the need for human involvement [1]. It is being implemented in all aspects of modern life. Automation is also feasible in occupational radiation safety and surveillance programmes. One kind of modern automation is Internet of Things (IoT), defined as technologies with which devices with sensors, data processing units and software are linked together over internet or any other network [2]. Health Physics Units attached to various nuclear or radiological facilities all over the world are associated with radiological surveillance and protection of workers and environment. This paper briefs about application of various IoT techniques for automation in environmental and occupational radiological monitoring and surveillance programmes.

Keywords: Automation, IoT, MQTT, LoRa, dose rate

1. Introduction: The application of radiation sources and technologies are increasing with the advent of numerous beneficial applications for the society. Environmental and occupational radiological surveillances are the paramount requirement of any nuclear or radiological facility. The objective of these surveillance programs is to minimize hazards to the occupational workers, public and environment from handling radiation sources while deriving fruitful benefits. The Health Physics Units attached with various facilities across the world is mandated to ensure the safety and protection of workers and environment. The objectives of surveillance programme are to (I) protect the environment and worker against harmful effects of ionizing radiation (II) keep all radiation exposures as low as reasonably achievable and (III) ensure regulatory compliance and keep all radiation exposures to well within regulatory limits.

Radiation exposures are broadly classified into two category (a) External exposure, when radiation source is situated outside the body and (b) Internal exposure, when radiation source is situated within tissues and human beings are exposed. Radiation dose rate survey for measurement of ambient dose rate is the main method of external exposure surveillance.

Automation is a term for technology application where human input is minimized. There are infinite advantages of any automation process. The most important are (i) Increased Safety (ii) Increased throughput or productivity (iii) Improved quality (iv) Increased predictability (v) Improved robustness (vi) Reduced direct human cost and expenses (vii) Reduced cycle time (viii) Increased accuracy (ix) Relieving humans of monotonous repetitive work and (x) Increased human freedom to do other things. These advantages have important contribution in reducing radiation exposure and increasing safety in radiological installations.

Internet of Things (IoT) is a concept defined as technologies with which devices with sensors, data processing units and software are linked together over internet or any other network. Based on terrain and/ or requirements, different types of IoT techniques are utilized. Some of the most widely used IoT technologies are wide area

General Pocket Radio Services (GPRS) and local range networks. GPRS based IoT system uses telecommunication modules from third-party service providers. It is either based on Global System for Mobile (GSM) communication with Subscriber Identification Module (SIM) or Code Division Multiple Access (CDMA) with or without SIM. This has advantages of being very wide area coverage and limitation of high dependence on third part operators. On the other hand, long range private networks are for dedicated communication within pre-determined terrain or area. LoRa™ is among the most utilized private IoT networks. This has the advantage of user defined hardware and software modules as well as, independent of any third-party service provider.

There are other local area network IoT technologies like WiFi and Bluetooth that are used in systems for implementing short range connectivity. This paper briefs about application of both GPRS based and LoRa™ based IoT technologies for automation in environmental and occupational radiological surveillances programmes.

2. Development of GPRS based Indian network of environmental radiation tracking system

Outdoor external dose rate measurements are carried out for various purposes such as (a) Environmental baseline studies prior to operation of any nuclear or radiological installation (b) During operational stage to ensure that the radiation levels are within stipulated limits and the installations do not release any radioactivity to the environment (c) Radiation monitoring during Radiological Emergency situations where presence of radioactive substances or any air borne radioactive material in environment is anticipated (d) Mineral resources survey, especially for Thorium and Uranium resources and (e) Academic studies. There are different types of radiation survey meters available in this purpose. With the advancements in GPS technology like low power and compact embedded systems, Radiation survey meters for outdoor applications are designed with inbuilt Global Position System (GPS) receivers. Such systems have the provision of displaying or storing environmental dose rate data with GPS tagging. The system developed by Health Physics Unit, IREL (India) Limited, Manavalakurichi is a network of GPS tagged radiation survey meters interfaced with central server through GPRS mode of networking to display the real time dose rate data on maps or GIS based software interface.

2.1. Material and methods for GPRS based systems

The requirement was to develop a system of portable radiation survey meters with sensitive radiation detectors and integral GPS modules. The dose rate data with GPS data tagging is to be connected to the server installed at Health Physics Unit, IREL(India) Limited, Manavalakurichi with suitable IoT connectivity. The system developed was intended for pan India radiation monitoring and data communication to extend the application of the system to all nuclear and radiological facilities in the country. As GPRS network has extensive coverage and the network system is spreading across entire country, this mode of communication was adopted for the development of the system.

The objective was further enhanced to explore developing a few radiation survey meter combined environmental gamma spectrometer modules with GPS tagging and GPRS connectivity. The modules shall generate and GPS tagged dose rate data as well as ambient gamma spectrum for monitored location.

There are three different operating protocols available for GPRS based IoT applications. They are HyperText Transfer Protocol (HTPP), Constrained Application Protocol (CoAP) and Message Queuing Telemetry Transport (MQTT). Each method has advantages and limitations. A brief summary of the same is listed below [3-5].

Table 1. Brief comparison of different data sharing protocols over GPRS

HTPP	**CoAP**	**MQTT**
Advantages Widely supported and ubiquitous. Human-Readable data formats Enhanced data security Request-Response Model for web applications. Operates in Full-duplex, Bidirectional modes.	**Advantages** CoAP is specifically designed for resource-constrained devices and low-power networks. Binary format and efficient messaging. Supports multicast communication, allowing multiple devices to receive the same message. Request/Response model for synchronous mode of data transmission.	**Advantages** Efficient Publish-Subscribe Model for real time updates. Low Overhead. Low bandwidth. User defined Quality of Service. Better data security. Simplified middleware. Publish/Subscribe model for IoT uses.
Disadvantages High Overhead and inefficient for small payloads or frequent communication in IoT scenarios. HTTP relies on long-lived connections for real-time updates, which may not be ideal for constrained devices or unreliable networks. HTTP's request-response model may introduce latency, especially when multiple round-trips are required to fetch data or interact with web services. This latency may not be acceptable for real-time IoT applications.	**Disadvantages** Less Widespread Adoption. Limited Middleware. Reliability Challenges with unreliable networks. Security Considerations requiring additional layers. Less Interoperability with other protocols. Complex translation or adaptation layers may be required.	**Disadvantages** Efficiency varies with specific use cases. Relatively new concept for developers. Not as widely used/ supported as HTPP.
Typical applications Web-based uses. Security-Intensive Applications.	**Typical applications** Resource constrained systems including low power IoTs.	**Typical applications** Real-Time IoT Applications. MQTT is a reliable choice for large-scale IoT deployments, with the ability to handle numerous devices efficiently.

1

Among these protocols, Message Queuing Telemetry Transport (MQTT) was chosen as preferred protocol for our IoT communication. This has the advantages of low band width and higher data density.

The detector used in the radiation survey meters is CsI(Tl) scintillator detector of size 10 mm x 10 mm x 10 mm, coupled with temperature compensated photo diodes was chosen for radiation detection and measurement. These detectors have sensitivity of approximately 80 counts per second per micro sievert per hour (cps/µSv h^{-1}). It has a good stability up 55˚C ambient temperature that is ideal for outdoor applications. The overall power requirement is also very less and can be sourced using batteries or solar panels.

Additional IoT linkage through WiFi mode was provided to connect each survey meter with a tuned android handset (mobile phone). This feature provided secondary readout and data logging. Hence the radiation survey meters could be used as portable backpack system, The block diagram of INERTS survey meter is shown in Figure 1.

As a part of prototype system development, five sensitive environmental radiation survey meters were fabricated and integrated with server at HPU, Manavalakurichi. The instrument has the resolution of 0.001 µSv h^{-1} and operating range up to 30 µSv h^{-1}.

Schematic diagram of Indian Network of Environmental Radiation Tracking System (INERTS) is shown in Figure 2.

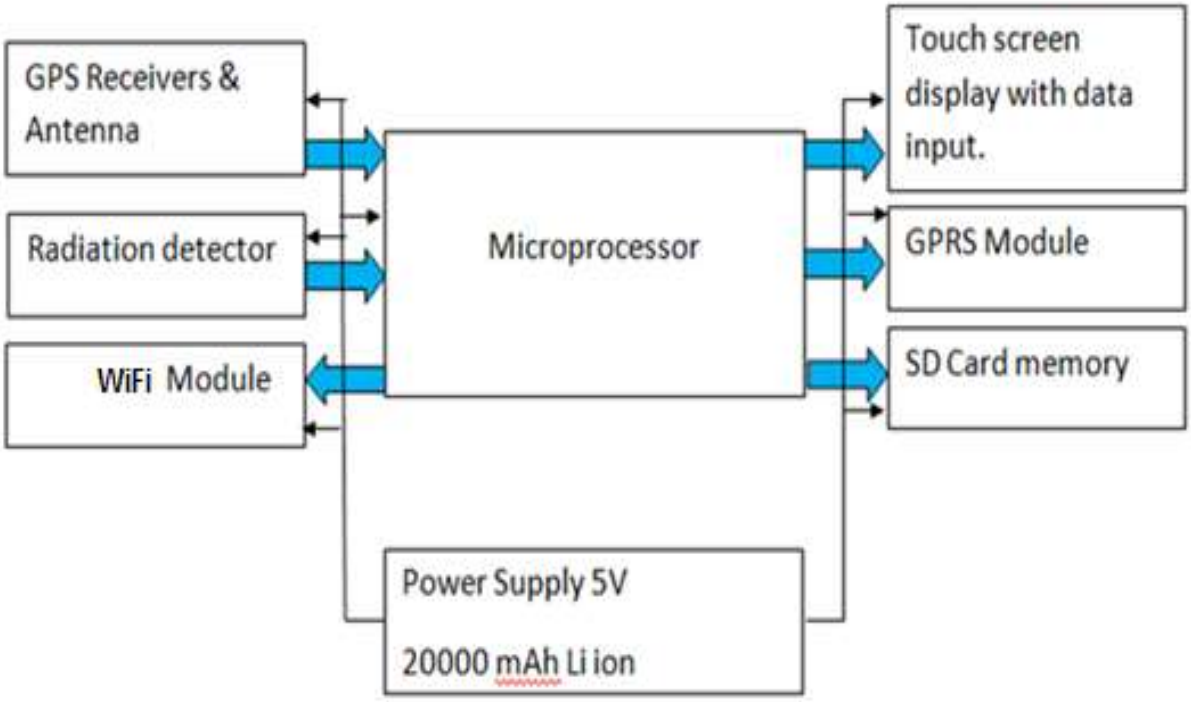

Figure 1. Block diagram of INERTS Radiation Surveymeter

Sensitive GPS module with 6-Channel receiver, u-blox 7 engine GPS/QZSS 1C/A and external antenna was used for incorporating GPS tagging to the environmental radiation data.

Image of INERTS detector module and survey meter are shown in Figure 3(A) and 3(B).

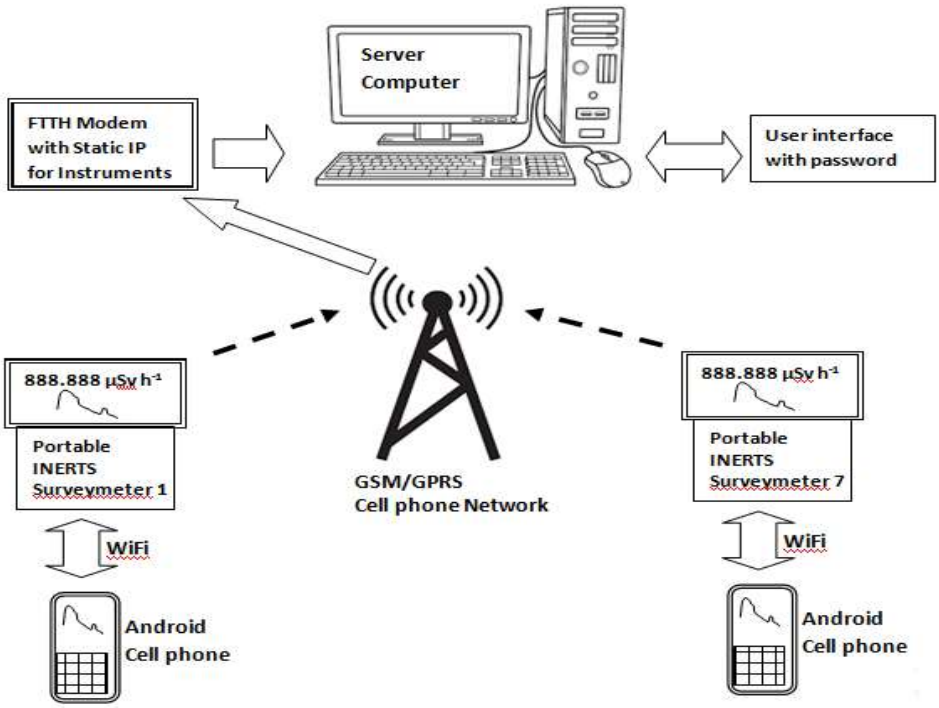

Figure 2. Schematic of Indian Network of Environmental Radiation Tracking System (INERTS).

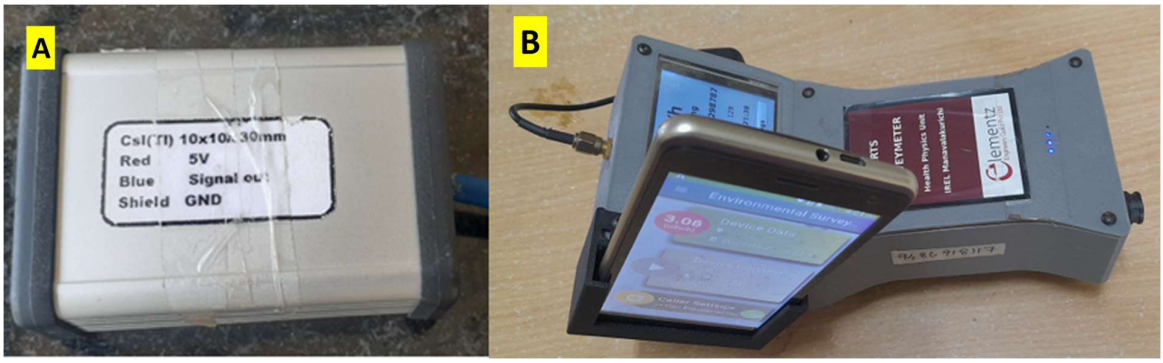

Figure 3. (A) CsI(Tl) detector module (B) INERTS Survey meter

The GPRS services by M/s Bharat Sanchar Nigam Limited was used for instrument connectivity with the server. The data generated by the instrument consisted of ambient Gamma Spectrum, dose rate (Ḣp(10)) , date & time, GPS coordinates and number of GPS satellites accessed.

Seven portable gamma spectrometers with radiation dose rate read out was also designed and fabricated using a more sensitive NaI(Tl) detector of size 25 mm x25 mm. This instrument can acquire and display ambient gamma spectrum, dose rate and GPS coordinates. Images of the same are shown in Figure 5.

The central server computer is installed at Health Physics Unit, IREL (India) Limited, Manavalakurichi. All the data generated by the portable field instruments are real time uplinked this server that has a Linux operating system (OS). The software interface for data acquisition and interface was developed using Python programming language. Both the OS and software development was done using open source software to make it adaptable across all platforms.

Date & Time	Status	Latitude	Longitude	cps	Dose rate µSv h^{-1}
09-07-2022 19:59	1	34.15835	77.58096	50	0.110
09-07-2022 19:59	1	34.15836	77.58097	48	0.110
09-07-2022 20:00	1	34.15836	77.58096	40	0.094
11-07-2022 14:48	1	34.14685	77.57451	30	0.068
11-07-2022 14:48	1	34.14685	77.57452	30	0.062
11-07-2022 14:50	1	34.14687	77.57446	28	0.060
11-07-2022 14:50	1	34.14687	77.57447	19	0.066
14-07-2022 13:44	1	33.22301	78.31491	57	0.121
14-07-2022 13:47	1	33.22298	78.31487	58	0.098
14-07-2022 13:47	1	33.22297	78.31487	41	0.095
15-07-2022 18:24	1	34.13869	77.54009	27	0.054
15-07-2022 18:24	1	34.13868	77.54009	31	0.056
17-07-2022 13:11	1	34.91456	76.79447	22	0.058
17-07-2022 13:12	1	34.91454	76.79448	29	0.061

Figure 4. Sample specimen of data generated by INERTS survey meter.

Figure 5. INERTS Gamma Spectrometer combined Radiation Surveymeter models

2.2. Data processing and application for GIS/ radiation mapping: The data generated by the Radiation Survey Meters and Portable Gamma Spectrometers were extensively used for radiation mapping of Kanyakumari and Kollam regions which is a part of Natural High Background Radiation Areas (NHBRA) in the country. To test the applicability of the system in different environmental conditions, radiation mapping of Ladakh region was also carried out. Images of the same are shown in Figure 6.

The radiation dose rate data generated by the INERTS survey meters are extensively used for generating GIS profiles. Radiation dose rate profile of NHBRA of Kanyakumari was done to test the system in different radiological conditions with wide variation in ambient dose rate as well as to quantify concentration of radioactive mineral Monazite which is the main contributor to the elevated dose rate in these locations. A specimen image of Arc GIS profile of external dose rate (µSv h^{-1}) is given in Figure 7. This demonstrates adaptability of data generated through IoT based radiation surveymeters for user interface applications.

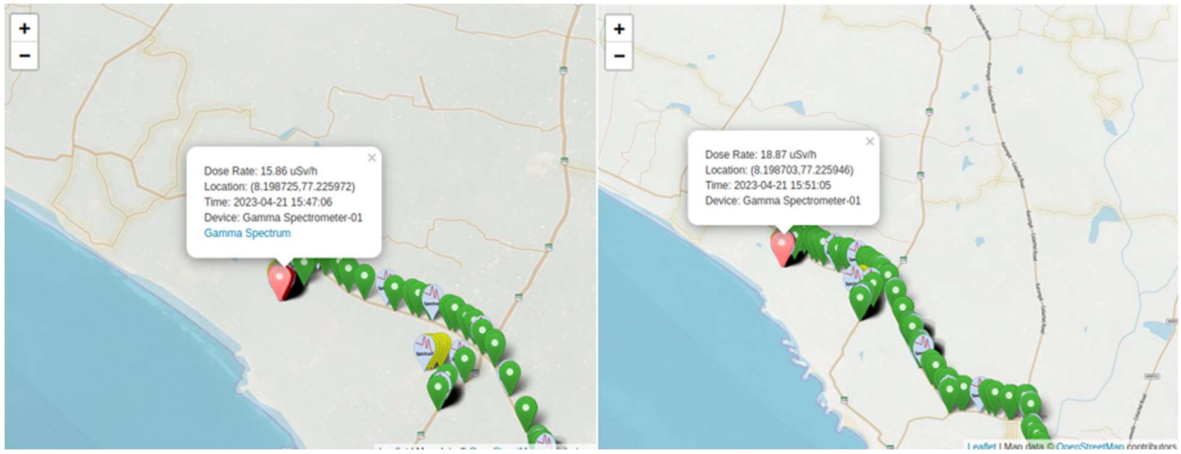

Figure 6. Radiation mapping of natural high background region of Kanyakumari

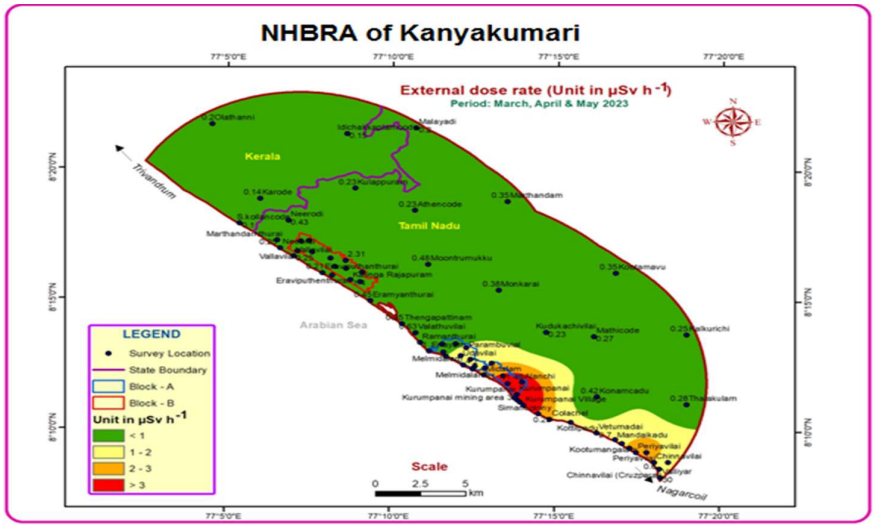

Figure 7. GIS profile of external dose rate at high background radiation area of Kanyakumari using IoT based surveymeters.

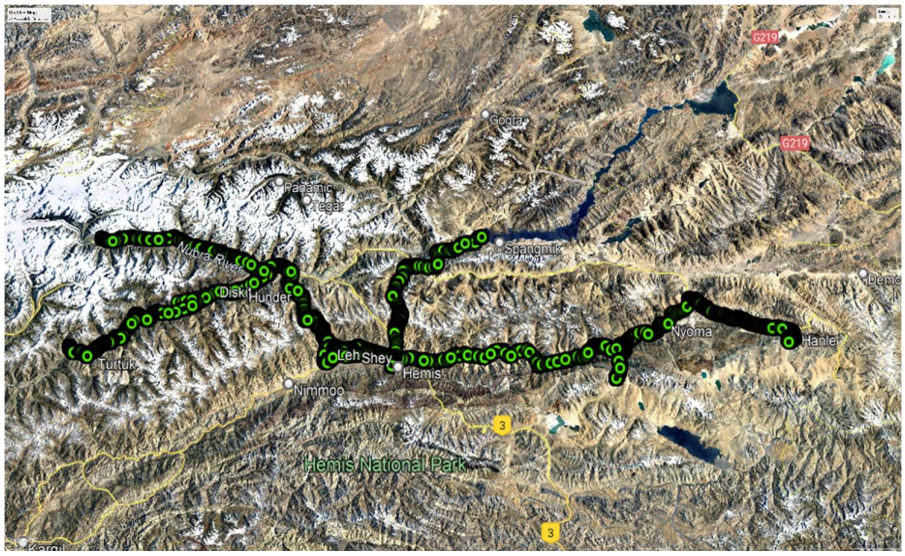

Figure 8. Radiation Mapping of Ladakh region

Radiation mapping of roads of Union Territory of Ladakh was done using INERTS surveymeter as backpack system. Real time monitoring and mapping of dose rate was done at most of the places, subjected to availability of GPRS signal.

3. Development of LoRa™ based integrated radiation monitoring system: External exposure monitoring which is an important aspect of occupational radiation protection in radiological facilities, is done by different methods. These methods include (a) Periodic radiation survey of workplaces (b) Installation of fixed Area Gamma Monitors and (c) Measurement of actual dose received by individual worker through use of active or passive dosimeters. Each methods has its distinct advantages over others and a combination of all methods are required for effective dose management of any radiation facility.

Periodic radiation survey and fixed location radiation monitoring are the two main methods for instantaneous assessment of radiation dose rate at workplace. The first method employs extensive use of human resources and later depends on the number of instruments installed at various work locations for accurate monitoring. Till date installing many fixed radiation monitors (Area gamma monitors) was impractical due to cost of instruments and difficulty in practically accessing each instrument for data collection or readout. Wired connectivity is often not feasible in large radiation facilities. The development of an IoT based Integrated system of fixed radiation monitors and accessing all through a single computer is made towards achieving better radiological monitoring and dose control at nuclear front end fuel cycle facilities. The Internet of Things (IoT) system based on LoRa™ transmitter working in Indian license free Industrial Scientific and Medical (ISM) frequency band of 865-867, 868 MHz is the most suitable module for interfacing with semiconductor-based radiation instruments. TEVISO 51 BG is a semiconductor-based radiation detector capable of measuring dose rate between 0.01 $\mu Sv\ h^{-1}$ to 100 $mSv\ h^{-1}$.

Teledosimetry or remote dosimetry is a concept of remotely measuring external dose received by a radiation worker. This tool is very effective for remote monitoring and control of doses in areas where high radiation exposure is likely. This manuscript describes the work carried out to develop a system of 15 network linked fixed area monitors and 5 teledosimeters to meet the requirement at Mineral Separation Plant, IREL (India) Limited, Manavalakurichi and to study the feasibility for adapting it for other larger nuclear and radiological installations.

3.1. Material and methods for local IoT based radiation monitoring system: The requirement was to develop a system with independent local IoT connectivity-based system where the requirement of GPRS mode of communication was not necessary. Instead, local networking options were studied for effectiveness and reliability. Various technologies like for Wireless Fidelity (Wi-Fi), Bluetooth, Zigbee, and LoRa were considered for our requirements. A brief comparison of different IoT techniques were made. Considering the relatively low volume of data, terrain profile with no line-of-sight configurations and presence of shielded walls between work areas and data receiver antenna, LoRa technique was the most suitable for IoT communication and a system using this mode of communication was developed.

Table 2. A brief comparison of different IoT techniques for local area network [6-8].

Features	**Wi-Fi**	**Bluetooth**	**Zigbee**	**LoRa**
Data Rate	High	Low to Mod	Low to Mod	Low to Mod
Frequency (India)	2.4 GHz, 5 GHz	2.4 GHz	865, 915 MHz, 2.4 GHz	865 MHz
Range	Short	Short	Short to Mod	Long
Power Consumption	Mod to High	Low to Mod	Low	Low
Network Topology	Varied	Varied	Mesh, Star, Tree	Star, P2P, P2MP
Data Security	Strong	Strong	Strong	Basic
Advantages	High data rates for data intensive uses. Ubiquitous and Wide availability. Supports multiple devices.	Versatile for personal area networking. Low to moderate power consumption.	Low power, suitable for battery driven devices. Mesh network for enhanced reliability. Strong security features with AES-128 encryption.	Exceptional low power and long-range coverage. Well suited for sensor- heavy applications. Cost- effective
Disadvantages	Limited range mainly for indoor use. Higher power consumption. High risk of interference in crowded bands.	Shorter range compared to Wi-Fi and LoRa. Moderate data rates High risk of interference in crowded 2.4 GHz band.	Limited range, typically up to 100 m indoors. Lower data rates compared to Wi-Fi. Relatively complex network setup.	Lower data rates compared to Wi-Fi Slower data transmission. Limited use cases outside of long-range IoT.

1

TEVISO 51 BG is a semiconductor-based radiation detector with sensitivity 5 counts per minute per microsievert per hour (5 cpm per µSv h^{-1}) capable of measuring dose rate between 0.01µSv h^{-1} to 100 mSv h^{-1}. Images of LoRA module and BG51 are shown below.

Table 3. Technical specifications of LoRa™ transceiver

Transmitter Details	
Transceiver	1W E byte E220
Modulation	LoRa TM
Frequency	865-867, 868 ISM
Legal requirement	License free
Weight	3 g+ 10 g for 2.5 dBi antenna
Power: Standalone/ Transmitting mode	20 mW / 1W
Operating Voltage	3.7 V Dc
Range	Max 7 km, typical 3km
Data transmission	0.018- 62.5 kbps
Receiver	8 Channel LoRa WAN with 12dBi antenna
Dose & Dose rate Data refreshing	Once in 10 Second (Maximum)
Number of dosimeters/ area gamma monitors linked	Maximum 08 @ 10 second data refreshment. 128 @ 3600 second data refreshment

1

Table 4 Technical specifications of radiation detector

Model	Teviso BG 51
Type of detector & Sensitivity	Si PIN Diode & 5 cpm/(µSv h^{-1})
Size & Weight	30mm, 15mm, 7 mm & 2.2g
Power	<0.01W
Operating Voltage	5-15 V Dc
Measurement Range	
Dose rate	0.001-100 mSv/h
Dose	**0.01-100 v**

1

Figure 9. (A) LoRa™ module, (B) TEVISO BG 51

This system consists of 08 No of outdoor fixed location monitors, 07 No of Indoor fixed location monitors for work area monitoring and 05 No of portable Teledosimeter for individual dose monitoring purposes. Salient features of the system are given below.

3.1.1. Fixed Area Outdoor Monitors: These are standalone system designed for fixing at outdoor locations without power supply access. This system consists of a radiation measurement unit with sensitive semiconductor detector (Sensitivity: 5 cpm per µSv h^{-1} dose rate) integrated with LoRa

TM based IoT module. The LoRa™ module is made up of 1W Ebyte E220 series (865-867 MHz) transceiver with 5dBi LoRa antenna. The power supply for the same is provided through an internal 4000mAh Li ion battery and charged by 3W Mono crystalline solar panel. The entire system including radiation measurement unit, IoT module, battery and solar cell is housed in an ABS enclosure with IP65 protection standard. Radiation dose rate data along with battery status, enclosure internal temperature and humidity is transmitted once in every 60 minutes through LoRa™ modulation. The system consumes very low power (≤ 20mW) during non-transmission time and inbuilt power supply can power the system for two days in the absence of charging from solar panels.

3.1.2. Fixed Area Indoor Monitors: Indoor monitors are identical with outdoor devices except that solar panel is replaced with 1" OLED display for dose rate. This module also is fitted with 4000 mAh Li ion battery, charged through external C type USB port. This instrument is designed for installation at indoor locations where external power supply (230 VAC) is available. However, for locations with sufficient light illumination, provision to easily convert to solar powered system through externally mounted panel adaptors is made. Both outdoor and Indoor monitors are programmed to transmit averaged dose rate data every 60 minutes and has a sensitivity of 0.01µSv h^{-1} and upper limit of 100 mSv h^{-1}. The dimension of both the monitors are 22 cm x 21 cm x 6 cm. and weight approximately 0.8 kg without clamp attachment.

3.1.3. Teledosimeters: LoRa™ based IoT technology is adapted for real time dose monitoring of radiation workers at Monazite Mineral Separation Plant. Teledosimeters also uses sensitive semiconductor detector (sensitivity: 5 cpm per µSv h^{-1} dose rate) and 1W EByte LoRa module with internally mounted 3 dBi antenna. Internal 4000mAh Li ion battery is charged through a C-type USB port. Cumulative dose and dose rate are transmitted once in every 15 second. Teledosimeter has dimension 9 cm x 6 cm x 3cm and weight approximately 0.1 kg. Images of Outdoor and Indoor monitors are shown in Figure 10 (A) and (B).

Images of dose rate display of Indoor monitor and LoRa based Teledosimeters are shown in Figure 11(A) and (B) respectively.

3.1.4. Installation of fixed monitors and LoRa receiver gateway: Installation of all the fixed area monitors were done as per monitoring requirements. Seven indoor monitors are installed within Mineral Separation Plant locations, considering potential for presence/accumulation of Monazite rich material. All the eight outdoor monitors are installed at various important environmental locations. One outdoor monitor is specially installed over Intertidal zone at Kadiapattanam – Valliyar river mouth location where monazite rich sand is deposited. This location is known for high natural high radiation background ranging 20 – 60 µSv h^{-1}.

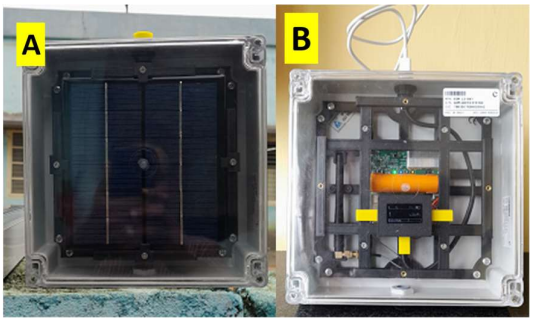

Figure 10. (A) Outdoor monitor with solar panel, (B) Indoor Monitor with OLED display

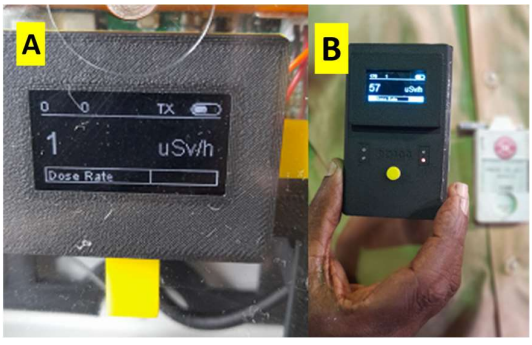

Figure 11. (A) Indoor monitor OLED display, (B) Teledosimeters

Location of installation of LoRa gateway for dose & dose rate reception is chosen in such a way to minimize structure or building shielding in between field instruments and receiver. Hence rooftop of tallest buildings was chosen for installation of LoRa Gateway system. It was operated continuously, powered by a 85Ah Lead acid battery connected with 65 W solar panel for charging.

The Health Physics Unit, where server computer is situated is approximately 80 m away from LoRa gateway installation. As this distance is on the higher side for Ethernet cabling, additional pair of 5 Ghz N300 Outdoor Wireless Bridge (802.11a) CPEs were installed between LoRa gateway and HPU server. Output of the Wireless bridge is fed to the server computer at Health Physics Unit. Among the Licence free ISM band of 865 -867 MHz, in-house frequency allocation of eight channels were assigned for fixed area monitors and mobile teledosimeters to avoid data interference. Installation at Valliyar river mouth and LoRa Receiver at tallest building top are shown in Figure 13(A) and (B).

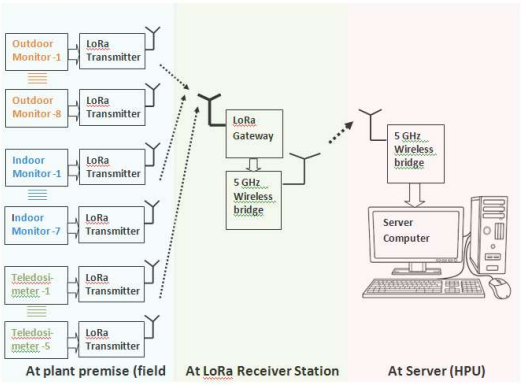

Figure 12. Schematic diagram of LoRa based Integrated Radiation Monitoring System

Table 5. In-house frequency allocation for LoRa™ based radiation monitors

Channel No	Frequency Hz	Device
0	865062500	Fixed Area Gamma Monitors
1	865402500	Fixed Area Gamma Monitors
2	865985000	Fixed Area Gamma Monitors
.3	865742500	Teledosimeters
4	866185000	Teledosimeters
5	866385000	Teledosimeters
6	866585000	Teledosimeters
7	866785000	Teledosimeters

1

Figure 13. (A) Monitor at Valliyar river mouth, (B) Solar powered LoRa receiver

3.1.5. Data reception, logging, and analysis: The receiver unit consist of an 8 channel RAK Wireless LoRa™ Gateway attached with 13 dBi antenna. Radiation data from eight outdoor monitors, seven indoor monitors and five Teledosimeters are received through LoRa gateway and stored in the central server kept at Health Physics Unit. Software for the data reception and

processing is done in PYTHON JANGO Programming on LINUX Operating System.

3.1.6. Data server and utility software: A common server is installed at Health Physics

Figure 14. Welcome screen for combined INERTS and IRMS utilities

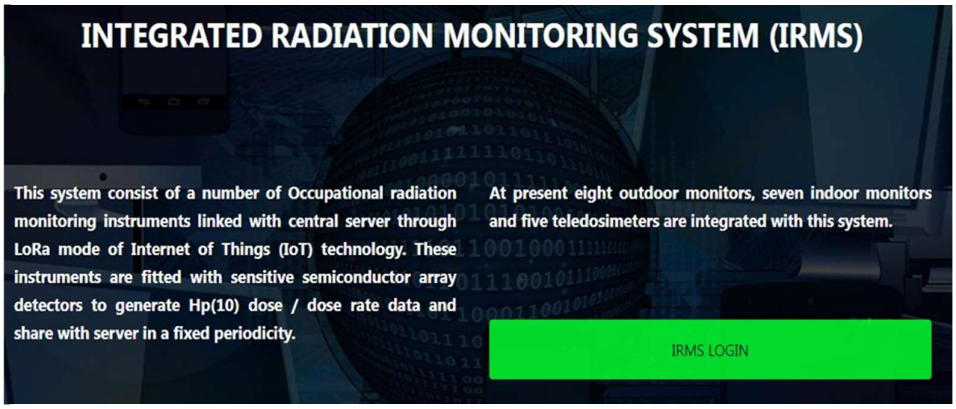

Figure 15. Login screen for IRMS

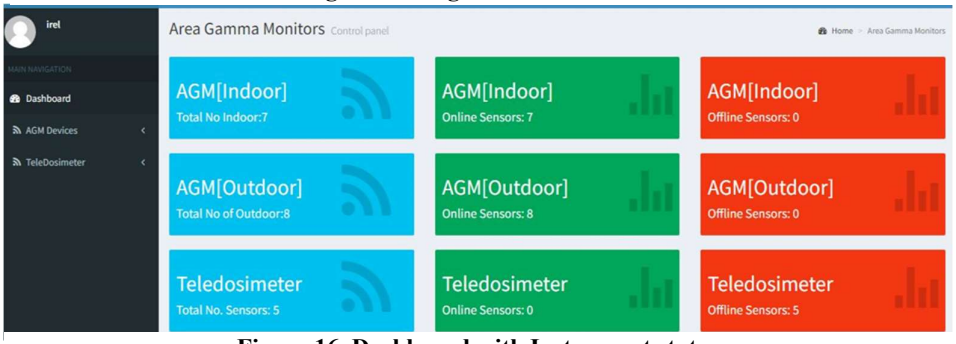

Figure 16. Dashboard with Instrument status

Figure 17. Status of radiation instruments

Unit to receive data from both MQTT based Indian Network of Radiation Tracking System (INERTS) and LoRa based Integrated Radiation Monitoring System (IRMS). Figures 14 and 15 shows welcome screen.

Further navigation to both features is password protected. On accessing Integrated Radiation Monitoring system, data from all the 20 radiation instruments are obtained. are obtained.

The radiation dose rate data can be fetched from the server and various functions like trend analysis, averaging, peak identification etc can be carried as required. Each instrument transmits dose rate data in every 60 minute and the same is recorded at the server. Outdoor monitors provide relatively consistent dose rate data since environmental variations are mostly negligible. However, location like Valliyar river mouth manifest dynamic dose rate profile during Monsoon months due to significant deposition and removal of Monazite mineral by strong sea currents. Images of dose rate profiles of different locations are shown in Figures 18 and 19.

Indoor monitors display ambient dose rate caused due to processing of Monazite mineral. Any increase in dose rate can be attributed to spilled or stagnant monazite rich material at plant locations or within equipment. A visual alarm is set to display readings in red if current hourly reading exceeds 1.5 times daily average value.

Similarly, data from teledosimeters consist of average dose rate and cumulative dose. This date is transmitted to the server in every 15 – 20 second. This data is very useful for understanding the dose rate profile of the radiation worker during the monitoring period. Dose rate profile of different work group are shown in Figure 20 and 21.

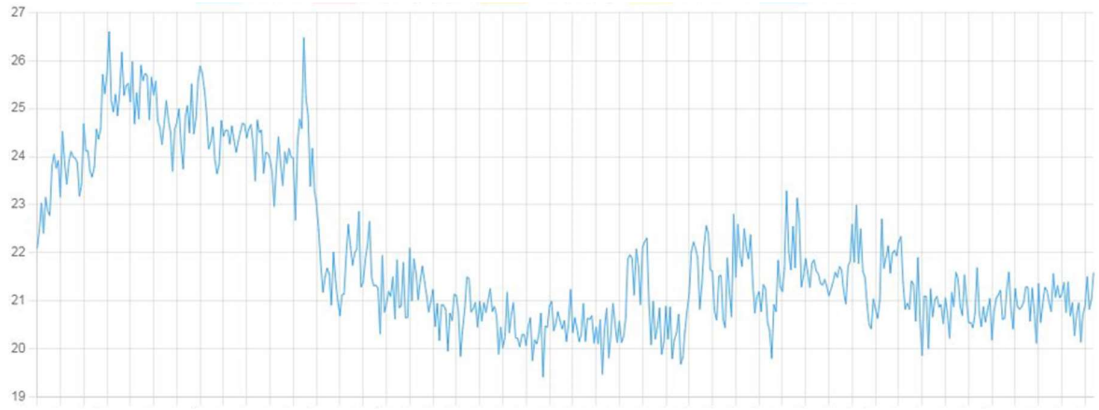

Figure 18. Observed variation of radiation dose rate (µSv h-1) at Valliyar river mouth

Figure 19. Observed variation of radiation dose rate (µSv h^{-1}) at Monazite reprocessing plant

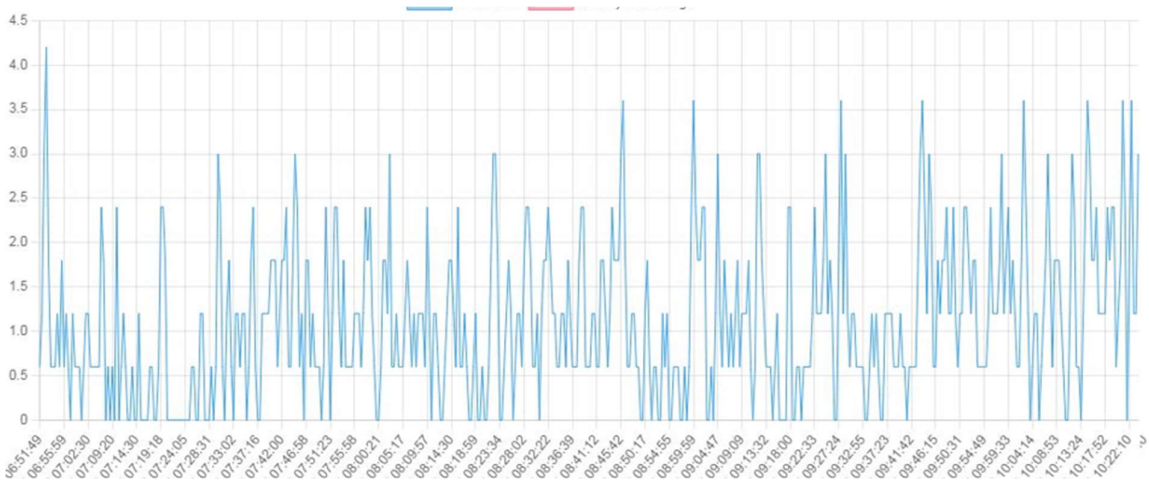

Figure 20. Observed radiation dose rate profile of HPU personnel on a monitoring day.

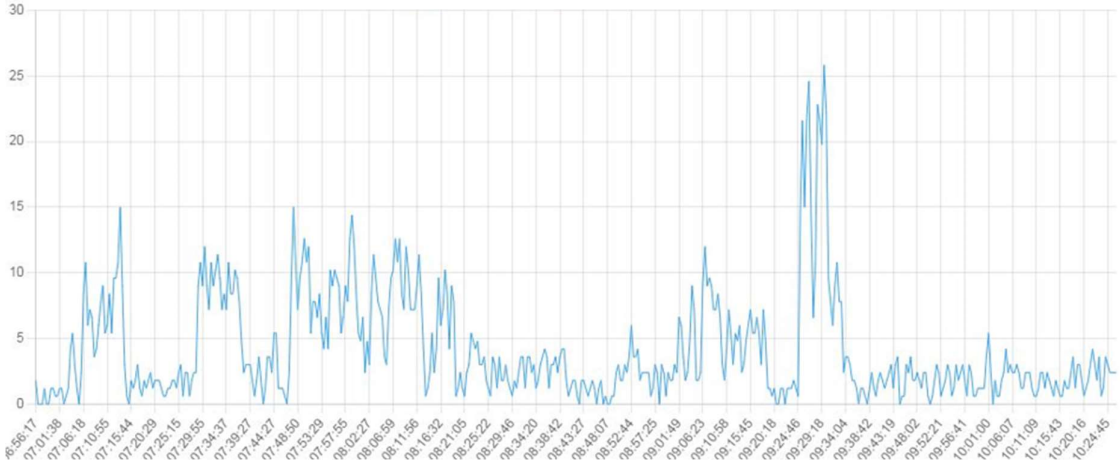

Figure 21. Observed radiation dose rate (µSv h^{-1}) profile of Monazite processing plant operator staff

Plant personnel spend more time within vicinity of Monazite rich material. Hence dose rate profile as well as cumulative dose received by them would be higher than other staff. Real time monitoring of their dose and dose rate is an effective tool for radiation exposure control.

4. Accuracy, error and failure analysis of the IOT based radiation measuring systems: All the radiation dose/ dose rate measuring instruments are calibrated with accuracy of ≤10%. Calibration of the fabricated instruments are done at an external facility with necessary accreditation. The estimated standard deviation (3σ) as well as least count for portable surveymeters is 0.001 µSv h^{-1} which is acceptable for environmental monitoring. The estimated standard deviation (3σ) as well as least count for fixed area monitors (both indoor and outdoor) is 0.1 µSv h^{-1} which also is acceptable for occupational monitoring whim facility. Accuracy of GPS modules used for INERTS Surveymeters is approximately 3 m and subjected to connectivity with satellites.

All the portable instruments are tested for shock, humidity, static electric and magnetic field for interference. All the components are shielded against radio frequency noises including system generated ones. The radiation detectors are temperature compensated up to 55°C. All the fixed area monitors and teledosimeters are specially designed against system generated RF noises as well as wide ambient temperature.

Allt portable surveymeters are inbuilt with internal storage device for primary data logging. Secondary and tertiary data logging is done independently at linked Android phone (WiFi) and at central server computer (GPRS- MQTT).

5. Conclusions: Internet of Things (IoT) techniques are very useful tool for automation. Effective utilization of these tools in radiological monitoring, with special emphasis to very wide area environmental monitoring (nationwide) and site specific occupational monitoring are briefed in this report.

Development and implementation of automation techniques is demonstrated for real-time monitoring of occupational and environmental radiation dose rate through effective adaptation of latest Internet of Things (IoT) concepts. GPRS based real-time tracking system was developed for environmental radiation dose rate mapping using CsI(Tl) detector with geo –tagging features. This was further enhanced with Spectrometric capabilities using NaI(Tl) detector. Application of IoT techniques is demonstrated by monitoring at Natural High Background radiation Areas in Kanyakumari, TN of southernmost India. For a comparison the Ladakh region of northernmost India was also monitored and mapped.. Portable Gamma Spectrometer Radiation Survey meter system with sensitive spectroscopic NaI(Tl) detectors and geo –tagging capability for real-time monitoring were also designed, fabricated, tested and demonstrated.

In addition to above, LoRa based IoT system was developed for real-time radiological monitoring of plant and premise locations with semiconductor radiation detector of dose rate measuring range between 0.01μSv h^{-1} to 100mSv h^{-1}. This included indoor and solar powered outdoor monitors; the latter is useful for remote location monitoring where power source is not available like coastal or unmanned areas. LoRa based IoT system was further used for developing Tele-dosimeters for real-time monitoring of external dose received by a radiation worker. This tool is for effective monitoring and controlling doses during high dose consuming jobs. The indigenous software developed for interface of these automation systems is also illustrated. This multiple types detectors and systems interface using IoT automation methodology is a unique developmental work that has not been reported worldwide in radiation monitoring applications. This developmental work can find numerous applications in various radiological facilities with challenging monitoring requirements.

Application of IoT concepts to the radiological monitoring has brought a measurable level of automation and improvement within. Important radiation instruments are in real time interface with the computer and measured parameters are analysed continuously. Various data analysis techniques like mapping, GIS Profiling, trend, alerts, reporting etc are easily done without any manual data input. Monitoring of radiological parameters at remote or difficult locations are made possible by exploring wireless data transmission, either through GPRS or LoRa devices. Measured parameters are also monitored at different hierarchy levels for better assessment.

The developments brought forward in this manuscript would enhance radiological metrology and bring in appreciable level of automation in different radiations safety and monitoring facilities and applications to meet occupational and environmental radiological measurements.

Acknowledgement

The authors are thankful to Shri. N.Nagaraj and Shri John Rose , Health Physics Unit, IREL (India) Limited, Manavalakurichi and Shri. S. Ajesh umar, Health Physics Unit, IREL (India) Limited, Udyogamandal for valuable support for this developmental work.

The authors are thankful to Dr. D.K. Aswal, Director, Health Safety and Environment

Group, B.A.R.C and Shri. Vivek Bhasin, Director, Bhabha Atomic Research Centre. The valuable support and encouragement from Shri. N.Selvarajan, Chief General Manager and Head, IREL (India) Limited, Manavalakurichi are also thankfully acknowledged.

Authors are thankful to the development partner for this project M/s Elements Engineers Guild Pvt Limited, Thiruvananthapuram, Kerala, for the valuable contribution in fabrication and assembly of the systems.

References:

[1] https://www.isa.org/about-isa/what-is-automation
[2] https://www.ibm.com/topics/internet-of-things
[3] Comparison between the Messaging Protocols: CoAP and MQTT Protocol. Amit Sharma et.al. www.jetir.org (ISSN-2349-5162), 2020 JETIR July 2020, Volume 7, Issue 7
[4] https://www.hivemq.com/article/mqtt-vs-coap-for-iot
[5] https://bytebeam.io/blog/choosing-the-right-iot-protocol-a-comprehensive-guide-on-mqtt-coap-and-http/
[6] https://www.hivemq.com/article/mqtt-vs-coap-for-iot/
[7] Neeraj Chhabra, Comparative Analysis of Different Wireless Technologies, nt. J. Sci. Res. in Network Security and Communication
[8] https://www.ijsrnsc.org/pub_paper/IJSRNSC/3-%20IJSRNSC-00117.pdf
[9] https://www.mokolora.com/lora-and-wireless-technologies/
[10] https://www.eclipse.org/community/eclipse_newsletter/2014/february/article2.php
[11] https://ovyl.io/insights-and-news/wireless-technologies

Investigating the DC Performance of Ni/Au and Pt/Au Schottky Gate Contacts on GaN HEMTs for Ku-band Applications

Chanchal[1,2], Khushwant Sehra[1,3]*, Amit Malik[2], Robert Laishram[2], D. S. Rawal[1], and Manoj Saxena[4]

[1]*Department of Electronic Science, University of Delhi, Delhi, India*
[2]*Solid State Physics Laboratory, Defence Research & Development Organization, Delhi, India*
[3]*Department of Electronics and Communication Engineering, Faculty of Technology, University of Delhi, Delhi, India*
[4]*Department of Electronics, Deen Dayal Upadhyaya College, University of Delhi, Delhi, India*

Volume 1, Issue 4, July 2024
Received:13 March, 2024; Accepted: 27 June, 2024
DOI: https://doi.org/10.63015/10S-2421.1.4

**Corresponding Author Email: khushwantsehra@fot.du.ac.in*

Abstract: This manuscript investigates the DC performance of Ni/Au and Pt/Au Schottky Gate contacts on 150 nm AlGaN/GaN HEMTs for Ku band applications. Comparison in terms of the short channel effects (SCEs), in particularly the drain-induced barrier lowering (DIBL), demonstrate the long-term stability of Ni/Au Schottky contacts for mm-wave applications. To assess the reliability of the Schottky metal scheme, the fabricated devices were subjected to a high gate reverse bias step stress of – 30 V with a step of – 5 V. A higher degree of ON–state resistance (R_{ON}) degradation for the Pt/Au Schottky contact evinces remarkable performance of Ni/Au Schottky contacts for mm-Wave applications.

Keywords: AlGaN/GaN HEMT, Barrier Height, Inhomogeneities, Threshold Voltage Shift, OFF – State Stress, Reliability

1. Introduction: The unique intrinsic properties of III – Nitrides, in particularly, the GaN have captured the semiconductor market for future mm – Wave applications [1]. The ability to exhibit high carrier mobilities along with high saturation velocities, make GaN based devices suitable for mm – Wave applications [2]. The apparent high performance of GaN based devices as claimed [3][4], essentially depend upon various factors. These include the quality of the epi – layer stack [5][6], along with the quality and the metal scheme implemented for the Ohmic and Schottky contacts [7][8]. The epi – layer engineering is focused towards minimizing grain boundaries and epitaxial defects for boosting the RF performance [6][9]. On the other hand, Ohmic metal engineering is specifically focused towards the reduction of contact resistance for compatibility towards high – speed operation [7][10], as opposed to the Schottky contact engineering which has a specific target towards achieving a lower gate leakage current all the while ensuring good adhesion towards the underlying epi – layer stack [8][11]. Commonly used metals include Ti [12], Pt [13], Ni [12], as possible candidates among the traditional metal stacks to improve the Schottky parameters such as the barrier height (Φ), ideality factor (η), thermal stability, and gate leakage current in an effort to improve the device reliability for mm – Wave applications. A Pt - based contact, for instance, as reported exhibits a higher Schottky barrier height [14][15] compared to the standard choice employing Ni - based contacts [16-18], and in essence would benefit power devices for mm – Wave operation specifically with short gate lengths as a courtesy of reducing the gate leakage current. As such, the demand for high frequency applications propels aggressive scaling of the GaN HEMTs in an attempt to target high frequency applications. This, however, is coupled with short channel effects (SCEs) due to which, a shorter gate loses its control over the 2D electron gas (2DEG)

channel. In this regard, to ascertain long - term reliability of GaN based devices, good quality Schottky contacts are required, which is the basis of this work.

This manuscript focuses on the reliability of Gate contacts for mm – Wave GaN HEMT devices sporting a gate length (L_G) of 150 nm. In this regard, two Schottky metal schemes based on Ni/Au and Pt/Au are considered, and the Gate contacts of the fabricated devices are subjected to a high field reverse bias step stress in an attempt to deliberately push the devices towards high gate leakage region. The manuscript is structured as follows. Section 2 gives a brief description about the fabrication aspects of the GaN HEMT devices considered in this work, while the reliability-based studies considering the two metal schemes are compiled in Section 3. Finally, the findings of this study are summarized in Section 4.

2. Experimental Methodology: The epi-layer structure of the Metal – Organic Chemical Vapor Deposition (MOCVD) based AlGaN/GaN HEMTs fabricated in this work is shown in Fig. 1(a). Starting from the SiC substrate, a 100 nm AlN nucleation layer is grown to reduce the lattice mismatch. Post the AlN growth, a 2.2 µm thick GaN buffer is grown which supports a 22 nm AlGaN barrier with an Aluminium concentration of 25%. The SEM micrograph depicting the Gate, Source, and Drain pad is shown in Fig. 1(b). Characterizing the epi – layer stack through hall measurements, reveal a 2DEG concentration of 1.1×10^{13} cm^{-2} and a carrier mobility of 1910 $cm^2V^{-1}s^{-1}$. The experimental processing steps are detailed in author's previous works [7][8]. A standard Ohmic metal scheme based on Ti, Al, Ni and Au is employed which is treated in rapid thermal annealing (RTA) in N_2 Ambient at 820 °C for 60 sec, for subsequent alloying. Passivation of the device is done by SiN_x using the plasma-enhanced chemical vapour deposition technique (PECVD) and gate slit opening. This is followed up by the Gate metal deposition with metal schemes Ni/Au (left - half) and Pt/Au (right - half) of 3" wafer (as shown in Fig. 2) with gate length, L_G = 150 nm, using the e-beam evaporation technique [19].

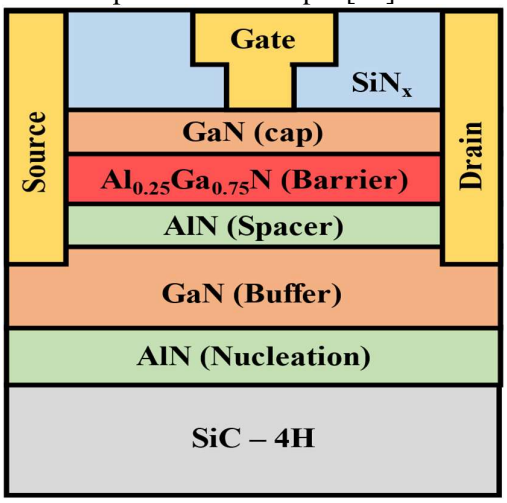

(a)

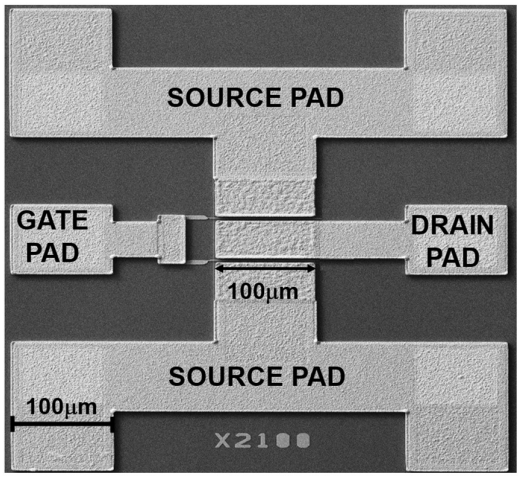

(b)

Figure 1. (a) Schematic representation, and (b) SEM Micrograph of the fabricated device having a Gate Length of 150 nm.

The source-drain terminals are 4 µm apart with a central gate placement. The DC – IV characterization of the fabricated devices was carried out using Keysight's Parametric Analyzer B1500A, revealing a high current density (I_{DS}) of 1.05 A/mm and a transconductance (g_m) of 250 mS/mm. The threshold voltage (V_{TH}) of the device as extracted from the transfer characteristics is – 5.8 V, and the ON – Resistance as extracted from the output characteristics is 3.3 Ω.mm.

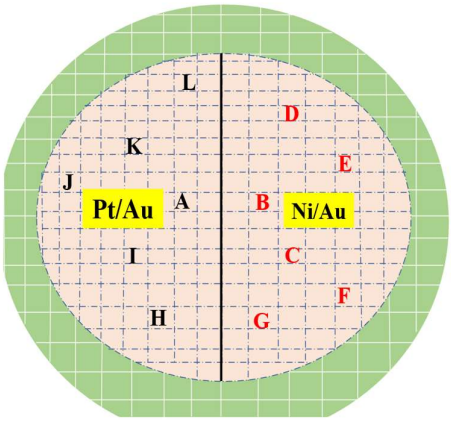

Figure 2. Schematic representation of 3-inch wafer with both (Pt/Au and Ni/Au) metal schemes.

To check the uniformity of the fabricated devices, six devices were characterized on each side of the wafer as shown in Fig. 2. The resulting DC characteristics of these devices are summarized in Table 1. It is observed that the maximum drain current (I_{DS}), peak transconductance (g_m), and the pinch – off voltage (V_{TH}) measured across 6 locations on each side of the wafer have a lower degree of deviation from their mean values, indicating a higher degree of uniformity throughout the wafer.

Table 1. List of parameters of measured devices at different positions with both the metal schemes

Location	Parameters		
	I_{DS} (A/mm)	g_m (mS/mm)	V_{TH} (V)
A	1.050	250	-5.80
I	1.045	248	-5.82
H	1.040	245	-5.82
J	1.044	248	-5.85
K	1.048	246	-5.80
L	1.042	244	-5.83
B	1.035	245	-5.80
C	1.032	243	-5.85
D	1.031	240	-5.80
E	1.028	241	-5.95
F	1.035	242	-5.80
G	1.030	238	-5.82

3. Results & Discussions

This section compares the Ni/Au and Pt/Au Schottky metal schemes in terms of two and three terminal characteristics followed by the reliability assessment as a means of validating and testing the fabricated AlGaN/GaN HEMT devices for mm-Wave applications.

3.1. Two terminal diode measurements

Forward and reverse characteristics of the Schottky diode of metal Ni/Au and Pt/Au are shown in Fig. 3. The Schottky parameters (Φ_B and η) of the two metal schemes were extracted (compiled in Table 2) using the thermionic emission (TE) [20] model at room temperature (T = 27 °C) by employing the standard diode Equation (1) and Equation (2):

$$I = I_S \left[\exp\left(\frac{qV - IR_D}{\eta kT}\right) - 1\right] \quad (1)$$

$$I_S = AA^*T^2 \exp\left(-q\,\Phi_B / kT\right) \quad (2)$$

Where, q : carrier charge,
k : Boltzmann's constant,
T : Temperature,
Φ_B : Schottky barrier height,
η : ideality factor,
A : diode area,
IR_D : voltage drop across the diode,
I_S : reverse saturation current, and
A* : Richardson constant for AlGaN

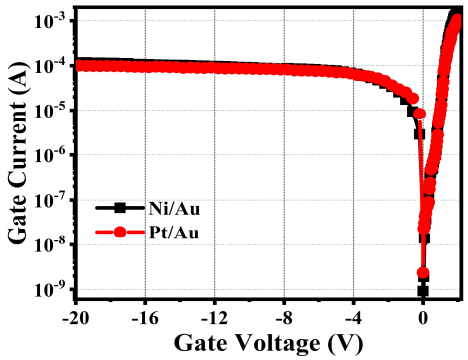

Figure 3. Two terminals forward and reverse characteristics for Ni/Au and Pt/Au Schottky metal schemes.

Table 2. Comparison of Schottky Parameters for the two metal schemes.

Schottky Metal	Parameters	
	ϕ_B (eV)	η
Ni/Au	0.562	1.28
Pt/Au	0.635	1.25

As shown in Table 2, Pt/Au metal has a higher barrier height and lower ideality factor compared to Ni/Au. This is due to the high work function of Pt metal [21, 22]. From Fig. 3, Pt/Au metal scheme has a lower leakage current compared to Ni/Au. This is due to metal-semiconductor surface inhomogeneities

and the higher metal work function of Pt metal [23-25].

3.2. Three terminal device measurements

Output Characteristics of L_G = 150 nm, W_G = 6 × 100 µm AlGaN GaN HEMT are shown Fig. 4 (a) and (b). The maximum drain current is 1.050 A/mm and 1.035 A/mm and transconductance is 250 mS/mm and, 245 mS/mm with Pt/Au and Ni/Au metal schemes, respectively.

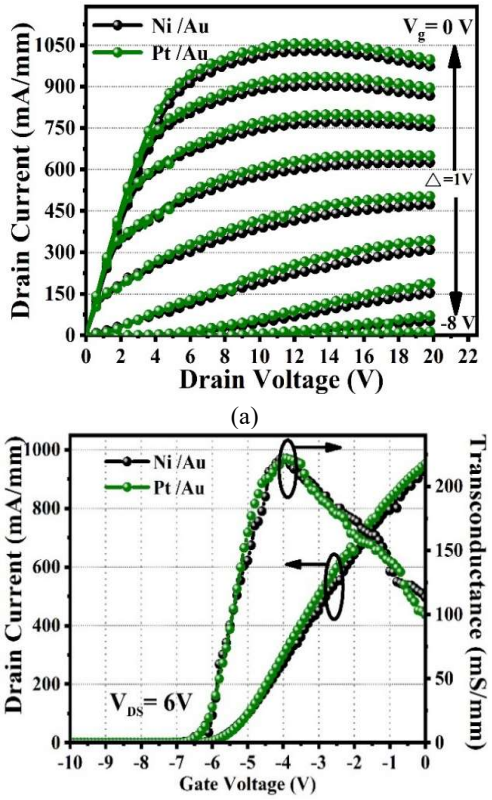

Figure 4. Impact of Ni/Au and Pt/Au Schottky metal schemes on (a) Output, and (b) Transfer characteristics of AlGaN/GaN HEMTs.

When the gate length is small in comparison to the barrier layer, aspect ratio ($L_G/t_{Barrier}$) ≤ 15, Short channel effects play a very important role [26, 27]. Here, with L_G = 150 nm and a barrier with 25 nm, the aspect ratio is 6. At higher drain to source voltage, V_{DS} (>10V), the confinement of the charge carrier becomes poor [27]. As shown in Fig. 5, with the increase in V_{DS}, a strong V_{TH} shift is observed. To pinch off the channel, the gate depletion region needs to be extended which results in a shift in V_{TH}. In shorter gate length devices, as V_{DS} increases, a high electric field drifts the charge carriers and the gate loses the control of flow of charge carriers and this phenomenon is known as drain-induced barrier lowering (DIBL) [24-27].

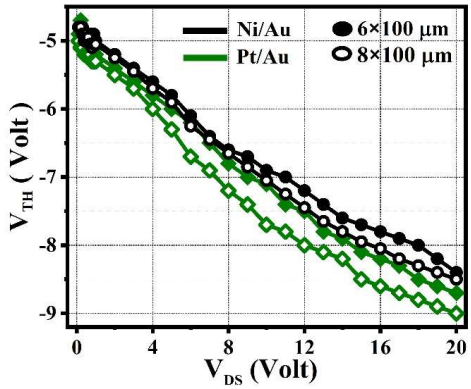

Figure 5. Spread of V_{TH} extracted at 1 mA/mm as a function of drain bias (V_{DS}) for the two Schottky metal schemes for large periphery GaN HEMT devices.

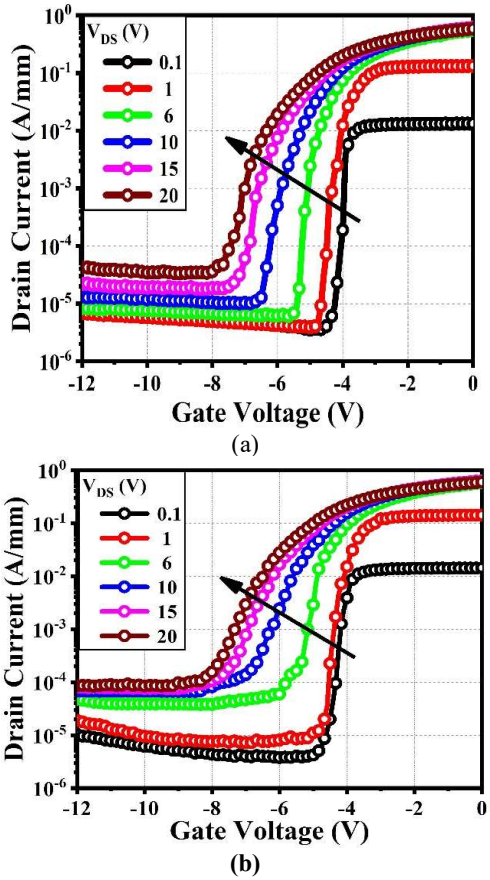

Figure 6. Transfer characteristics of 6×100 µm AlGaN/GaN HEMT at different V_{DS} (0.1, 1, 6, 10, 15 and 20 V) with L_G=150nm (V_{GS} swept from -12 to 0

V), for (a) Ni/Au, and (b) Pt/Au Schottky Gate contacts.

Figures 6 (a) and (b) show that Pt/Au has a higher V_{TH} compared to Ni/Au. This may be due to Metal - Semiconductor interface inhomogeneities [21, 22]. This shows that, in high voltage applications, the device with Pt/Au-based Schottky contact, shows a degradation in the device performance against the Ni/Au-based contact.

3.3. RF characterization

The device current gain($|H_{21}|$) of both the metal schemes is shown in Fig. 7. The device with Ni/Au and Pt/Au metal schemes has cutoff frequencies (F_T) of 38 GHz and 36 GHz, respectively. The maximum unilateral gain (MUG) indicates the maximum oscillating frequency (F_{MAX}) of the device, which is 60 GHz for the Ni/Au and 54 GHz for the Pt/Au scheme. Accordingly, the Ni/Au based metal scheme points towards achieving a better RF performance owing to its lower gate resistance compared to the Pt/Au metal scheme.

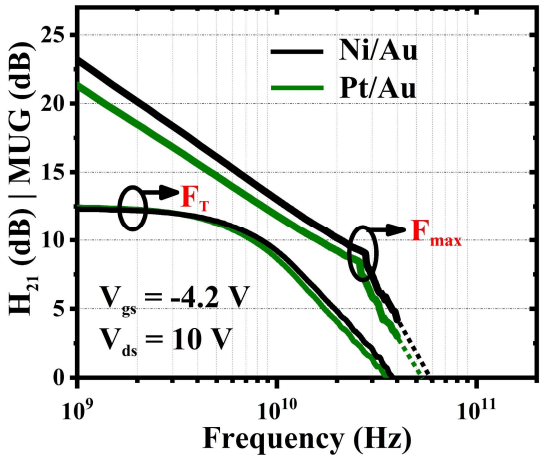

Figure 7. RF characteristics of the devices with Ni/Au and Pt/Au metal schemes.

3.4. Reverse bias step stress measurement

In the step stress measurement method, stress is applied to the gate terminal over some time, and gate current is observed. In this experiment, the V_{GS} is stepped up by -5V, and the gate current is observed for 120 seconds. The results of high reverse bias gate voltage step stress are shown in Fig. 8 (a) and (b). The findings suggest that leakage remains recoverable up to a gate voltage of -20V, attributed to the trapping of electrons beneath the gate region. Above -20V, the gate current becomes noisy and undergoes a significant increase, signaling degradation in device performance in both the metal scheme Ni/Au and Pt/Au as shown in Fig. 8(a). Gate voltage exceeding 25V (absolute value) shows irreversible degradation.

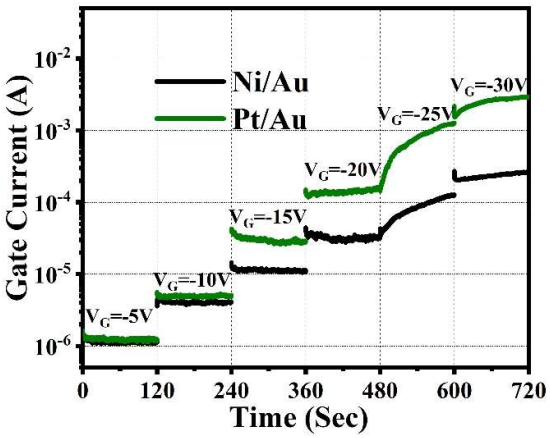

(a)

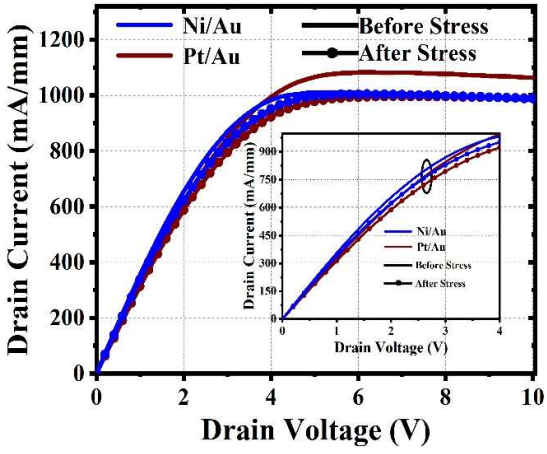

(b)

Figure 8. Reverse bias step stress scheme depicting (a) evolution of Gate current as a function of transient time, and (b) impact on R_{ON} calculated post high field stress.

As high voltage is applied to the gate terminal, the vertical electric field in the device increases which induces paths for current and rise in the gate current is observed [30-33]. Also, a high electric field deteriorates the crystallography of the barrier layer and induces an inverse piezoelectric phenomenon. However, due to M-S interface inhomogeneities, Pt/Au shows a higher leakage current rise compared to Ni/Au.

Also, Zanoni *et al*. [32] reported through electroluminescence (EL) analysis that hot spot formation at the gate edge under high reverse bias contributes to the rise in leakage current. DC characterization is carried out before and after each step of stress. To observe the current collapse phenomenon, or more appropriately an increase in the On-resistance (R_{ON}) of the device. Fig. 8(b) shows the increase in the R_{ON} after stress in both cases. Table 3, summarizes the change in the parameter after stress.

Table 3. Change in device parameters before and post high field electrical stress.

Parameters		Metal Scheme	
		Ni/Au	Pt/Au
I_{DS} (mA/mm)	Before Stress	1000	1060
	After Stress	980	980
	Change (%)	2	8
R_{ON} (Ω·mm)	Before Stress	3.65	3.62
	After Stress	4.50	5.0
	Change (%)	23.28	38.12

A significant change (in %) with Pt/Au-based contact is observed compared to Ni/Au post-high voltage reverse bias step stress. Chakraborty *et al*. [34] have also reported that Pt/Au-based Schottky gate contact tends to degrade with temperature and electrical stress compared to Ni/Au-based contacts.

4. Conclusions

Ni/Au and Pt/Au-based Schottky Gate contacts were realized on epi–layer stack consisting of AlGaN/GaN HEMTs for targeting mm–Wave applications. While the initial comparison based on Schottky parameters points towards Pt/Au to be the preferred choice for Gate contacts due to comparatively higher barrier height and lower gate leakage current, the Ni/Au-based contacts as investigated exhibit better reliability when subjected to a high field stress. A reverse bias strep stress subjected to two metal schemes reveals a degradation of 8% and ~38% in I_{DSS} and R_{ON}, respectively in the case of Pt/Au contacts against the 2% and ~24% degradation recorded in Ni/Au contacts for the I_{DSS} and R_{ON}, respectively. In addition to these, due to the improvement in barrier inhomogeneities with the Ni/Au-based contact, the GaN HEMT with Ni-based contacts demonstrate a smaller spread in V_{TH} with applied drain bias, pointing towards a better suppression of the SCEs compared to the Pt-based contacts. These results point towards the remarkable performance of Ni/Au-based Schottky metal contacts for Ku–band applications.

Acknowledgement

The authors would like to acknowledge Dr. Meena Mishra (Director) of SSPL, DRDO for providing the facilities and necessary support. The authors are thankful to the GaN fabrication group of SSPL for technical support and discussion.

CRedit Author Statement

Chanchal: Conceptualization, Methodology, Visualization, Data analysis and interpretation, Investigation and Writing – Original Draft.
Khushwant Sehra: Methodology, Writing-Reviewing and Editing, Proofreading.
Amit Malik: Visualization, Supervision, Technical Inputs.
Robert Laishram: Technical Inputs and Proofreading.
Dipendra Singh Rawal: Supervision, Writing- Reviewing and Editing, Validation, Technical Inputs and Resources.
Manoj Saxena: Supervision, Proofreading, Writing- Reviewing and Editing, Technical Inputs.

Conflict of Interest

Authors declare No conflicts of interest.

References

[1] S. Krause *et al.,* "AlScN/GaN HEMTs Grown by Metal-Organic Chemical Vapor Deposition With 8.4 W/mm Output Power and 48 % Power-Added Efficiency at 30 GHz," in IEEE Electron Device Letters, vol. 44, no. 1, pp. 17-20, Jan. 2023, doi: 10.1109/LED.2022.3220877.

[2] N. Collaert *et al.,* "III-V/III-N technologies for next generation high - capacity wireless communication," in International Electron Devices Meeting (IEDM), pp. 11.5.1-11.5.4, Dec. 2022, doi: 10.1109/IEDM45625 .2022.10019555.

[3] P. Wang *et al.,* "Evaluation of Power and Linearity at 30 GHz in AlGaN/GaN HEMT Fabricated by Integrating Transistors With Multiple Threshold Voltages," in IEEE Transactions on Electron

Devices, vol. 71, no. 3, pp. 1421-1427, March 2024, doi: 10.1109/TED.2023.3347710.

[4] A. Hickman *et al.*, "2.2 W/mm at 94 GHz in AlN/GaN/AlN High Electron Mobility Transistors on SiC," in Physica Status Solidi A, vol. 220, no. 16, January 2023, doi: 10.1002/pssa.202200774.

[5] A. S. Razeen *et al.*, "Structural, optical, and electrical characterization and performance comparison of AlGaN/GaN HEMT structures with different buffer layers," in Vacuum, vol. 219, art. no. 112704, January 2024, doi: 10.1016/j.vacuum.2023.112704.

[6] D.-Y. Chen *et al.*, "Impact of the Channel Thickness on Electron Confinement in MOCVD-Grown High Breakdown Buffer-Free AlGaN/GaN Heterostructures," in Physica Status Solidi A, vol. 220, no. 16, art. no. 2200496, September 2022, doi: 10.1002/pssa.202200496.

[7] A. K. Visvkarma *et al.*, "Ohmic contact morphology improvement with reduced resistance using Si/Au/Ti/Al/Ni/Au (AlGaN) and Si/Au/Ti/Al/Ni/Au (InAlN) stack layers in III-Nitride HEMTs," in Semiconductor Science and Technology, vol. 37, no. 8, art. no. 085006, June 2022, doi: 10.1088/1361-6641/ac6f79.

[8] A. K. Visvkarma *et al.*, "Comparative study of Au and Ni/Au gated AlGaN/GaN high electron mobility transistors," in AIP Advances, vol. 9, no. 12, art. no. 12531, December 2019, doi: 10.1063/1.5116356.

[9] D. M. Fleetwood *et al.,* "Low-Frequency Noise Due to Iron Impurity Centers in GaN-Based HEMTs," in IEEE Transactions on Electron Devices, vol. 71, no. 2, pp. 1024-1030, Feb. 2024, doi: 10.1109/TED.2023.3347212.

[10] Z. Xie *et al.,* "Ta/Al/CuW low temperature ohmic contacts for GaN-on-Si HEMT," in Microelectronic Engineering, vol. 286, art. no. 112132, March 2024, doi: 10.1016/j.mee.2024.112132.

[11] X. Ding *et al.*, "Gate leakage mechanisms of the AlGaN/GaN HEMT with fluorinated graphene passivation," in Materials Science in Semiconductor Processing, vol. 162, art. no. 107502, August 2023, doi: 10.1016/j.mssp.2023.107502.

[12] A. E. Islam *et al.*, "Effect of High Temperature on the Performance of AlGaN/GaN T-Gate High-Electron Mobility Transistors With ~140-nm Gate Length," in IEEE Transactions on Electron Devices, vol. 71, no. 3, pp. 1805-1811, March 2024, doi: 10.1109/TED.2024.3353694.

[13] S. Alam *et al.,* "Estimation of electrostatic, analogue, Linearity/RF figures-of-merit for GaN/SiC HEMT," in Micro and Nanostructures, vol. 186, art. no. 207738, February 2024, doi: 10.1016/j.micrna.2023.207738.

[14] E. Akso *et al.*, "Schottky Barrier Gate N-Polar GaN-on-Sapphire Deep Recess HEMT With Record 10.5 dB Linear Gain and 50.2% PAE at 94 GHz," in IEEE Microwave and Wireless Technology Letters, vol. 34, no. 2, pp. 183-186, Feb. 2024, doi: 10.1109/LMWT.2023.3345531.

[15] N. Miura *et al.*, "Effects of interfacial thin metal layer for high-performance Pt-Au-based Schottky contacts to AlGaN-GaN," in IEEE Transactions on Electron Devices, vol. 51, no. 3, pp. 297-303, March 2004, doi: 10.1109/TED.2003.822472.

[16] L. Liu *et al*., "Comparison of DC performance of Pt/Ti/Au- and Ni/Au-gated AlGaN/GaN high electron mobility transistors," in Journal of Vacuum Science & Technology B, vol. B29, art. no. 042202, July 2011, doi: 10.1116/1.3607601.

[17] S. Bouzid-Driad *et al.*, "Optimization of AlGaN/GaN HEMT Schottky contact for microwave applications," in European Microwave Integrated Circuit Conference, pp. 119-122, 2012.

[18] K. Floros *et al.,* "Dual barrier InAlN/AlGaN/GaN-on-silicon high-electron-mobility transistors with Pt- and Ni-based gate stacks: Dual barrier InAlN/AlGaN/GaN-on-silicon high-electron-mobility transistors" in Physica Status Solidi (A) Applications and Materials, vol. 214, no. 8, art. no. 1600835, July 2017, doi: 10.1002/pssa.201600835.

[19] Chanchal *et al*., "Physical insights into the reliability of sunken source connected field plate GaN HEMTs for mm-wave applications", in Microelectronics Reliability, vol. 148, art. no. 115170, 2023, doi: 10.1016/j.microrel.2023.115170.

[20] Wu Mei *et al.,* "Schottky forward current transport mechanisms in AlGaN/GaN HEMTs over a wide temperature range", in Chinese Phys. B, vol. 23, no. 9, art. no. 097307, 2014, doi: 10.1088/1674-1056/23/9/097307.

[21] Sun *et al.,* "Review of the recent progress on GaN-based vertical power Schottky barrier diodes (SBDs)," in Electronics, vol. 8, no. 5, pp. 1 – 15, 2019, doi: 10.3390/electronics8050575.

[22] B. Ofuonye *et al.,* "Electrical and microstructural properties of thermally annealed Ni/Au and Ni/Pt/Au Schottky contacts on AlGaN/GaN heterostructures," in Semiconductor Science and Technology, vol. 29, no. 9, pp. 1 – 10, 2014, doi: 10.1088/0268-1242/29/9/095005.

[23] A. K. Visvkarma *et al.*, "Improvement in Schottky barrier inhomogeneities of Ni/AlGaN/GaN Schottky diodes after cumulative γ-ray irradiation", in Semiconductor Science and Technology, vol. 36, no. 6, art. no. 065012, pp. 1 – 10, 2021, doi: 10.1088/1361-6641/abf46d.

[24] M. A. Laurent *et al.*, "Barrier height inhomogeneity and its impact on (Al,In,Ga)N Schottky diodes", in Journal of Applied Physics, vol. 119, no. 6, art. no. 064501, pp. 1 – 7, 2016, doi: 10.1063/1.4941531.

[25] S. Karboyan, *et al.,* "Analysis of barrier inhomogeneities in AlGaN/GaN HEMTs' Schottky diodes by I-V-T measurements," in European

Microwave Integrated Circuit Conference, Nuremberg, Germany, pp. 240-243, 2013.

[26] O. Breitschädel *et al.*, "Short-channel effects in AlGAN/GaN HEMTs," in Materials Science and Engineering B-advanced Functional Solid-state Materials, vol. 82, no. 1 – 3, pp. 238 - 240, 2001, doi: 10.1016/S0921-5107 (00)00747-9.

[27] M. Nuo *et al*., "Gate/Drain Coupled Barrier Lowering Effect and Negative Threshold Voltage Shift in Schottky-Type p-GaN Gate HEMT," in IEEE Transactions on Electron Devices, vol. 69, no. 7, pp. 3630 - 3635, July 2022. doi:10.1109/ TED.2022.3175792.

[28] Charu *et al.,* "Suppression of Short-channel Effects by Double-gate Double-channel Device Design in Normally-off AlGaN/GaN MIS-HEMTs," in IETE Journal of Research, vol. 67, no. 3, pp. 425 – 432, 2021, doi: 10.1080/03772063.2018. 1541764.

[29] K. Harrouche *et al*., "Low Trapping Effects and High Electron Confinement in Short AlN/GaN-on-SiC HEMTs by Means of a Thin AlGaN Back Barrier," in Micromachines, vol. 14, no. 2, pp. 1 - 7, 2023, doi: 10.3390/mi14020291.

[30] Meneghesso *et al.,* "Degradation of AlGaN/GaN HEMT devices: Role of reverse-bias and hot electron stress," in Microelectronic engineering, vol. 109, pp. 257-261, 2013, doi: 10.1016/j.mee. 2013.03.017.

[31] Meneghesso *et al.,* "Reliability of GaN high-electron-mobility transistors: State of the art and perspectives," in IEEE Transactions on Device and Materials Reliability, vol. 8, no. 2, pp. 332 – 343, 2008, doi: 10.1109/TDMR.2008.923743.

[32] E. Zanoni *et al.,* "Localized damage in AlGaN/GaN HEMTs induced by reverse-bias testing," in IEEE Electron Device Letters, vol. 30, no. 5, pp. 427 – 429, 2009, doi:10.1109/LED.2009. 2016440.

[33] J. A. del Alamo *et al.*, "GaN HEMT reliability," in Microelectronics Reliability, vol. 49, no. 9 – 11, pp. 1200 – 1206, 2009, doi:10.1016/j.microrel. 2009.07.003.

[34] S Chakraborty *et al.,* "Comprehensive Schottky Barrier Height Behavior and Reliability Instability with Ni/Au and Pt/Ti/Pt/Au on AlGaN/GaN High-Electron Mobility Transistors," in Micromachines, vol. 13, no. 1, pp. 1 – 10, 2022, doi:10.3390/ mi13010084.

Synthesis and Characterization Techniques of Nanocomposite Polymer Electrolytes Membranes: An Overview

Markandey Singh[1], Ubaid Ahmad Khan[2], Anshuman Srivastava[2], Nidhi Asthana[3,4*]

[1]*Department of Applied Science, Buddha Group of Institution, GIDA, CL-1, Sector 7, Gorakhpur-273209*
[2]*Mechanical Engineering Department, SIET, Prayagraj, India.*
[3]*Department of Physics, Babasaheb Bhimrao Ambedkar University, Lucknow, U.P. India.*
[4]*Department of Physics, Graphic Era (Deemed to be University), Dehradun, Uttarakhand, India.*

Volume 1, Issue 4, July 2024
Received:10 June, 2024; Accepted: 6 July, 2024
DOI: https://doi.org/10.63015/5N-2432.1.4

**Correspondence Author:* asthananidhi27@gmail.com

Abstract: The nanocomposite polymer electrolytes (NCPEs) are receiving special attention, especially within the realm of Solid-State Ionics by virtue of potential applications in innovative ionic devices (electrochemical devices) like Smart windows, sensors, high-powered batteries, fuel cells, and supercapacitors. etc. Using nanocomposite constituents, a versatile and robust approach has been developed to achieve novel nanocomposite polymer electrolytes (NCPEs) with tailored structural, thermal, mechanical, electrical, and electrochemical characteristics. This study describes the techniques used for the synthesis of inorganic fillers such as ceramic, ferrites nanoparticle, and nanocomposite polymer electrolyte films and their characterizations with emphasis on the sol-gel technique as it pertains to in this work. Different characterizing techniques related to current investigations like XRD, Optical Microscopy, SEM, IR(FTIR), DSC, CV and electrical characterization techniques like Wagner's polarization, impedance spectroscopy, dielectric spectroscopy and modulus spectroscopy have been briefly discussed to allow an amateur to understand the importance of these techniques in materials research in general.

Keywords: Nanocomposite Polymer Electrolytes, Electrochemical Devices, Impedance Spectroscopy, Modulus Spectroscopy.

1. Introduction: Materials science, organic chemistry, inorganic chemistry, polymer science, and electrochemistry are all included in the highly specialised multidisciplinary topic of polymer nanocomposite electrolyte science. This field has attracted the attention of both academics and industry professionals for the last three decades due to the bright applications of these electrolytes. The synthesis and characterization of polymer nanocomposite electrolyte involves various physio-chemical experimental techniques [1-3]. Synthesis techniques that affect the regulation of particle size distribution, dispersion, and interfacial interactions are essential to realising the unique features of polymer nanocomposite electrolytes. Because each system differs in physiochemistry, it is impossible to create a single, universal technique for generating polymer nanocomposites. Instead, synthesis techniques for nanocomposites are very different from those for ordinary micro scale-filled composites. To form, each polymer system could need a unique set of processing conditions, and different synthesis methods might generally provide non-equivalent outcomes. Keeping this fact in mind all the techniques used in the present investigation for development of nanocomposite polymer electrolytes have been briefly overviewed to enable a fresher to understand the basics of these techniques. To develop a material with desirable properties, it is essential to characterize it. Characterization of materials encompasses the delineation of all attributes pertaining to the composition, structure, and other relevant properties of a specific material

composition that are necessary for replicating a material with a desired characteristic. Within the framework of nanocomposite polymer electrolytes, it is essential to study interaction among components, their morphology, thermal behavior, electrochemical behavior, and ion conducting properties. Thus, all the techniques associated with these investigations have also been reviewed to make the presentation comprehensive. Because of its potential use in cutting-edge electrochemical devices such as efficient fuel cells, high-performance batteries, supercapacitors, sensors, and smart windows, nanocomposite polymer electrolyte materials (NCPEs) have drawn interest recently.

When it comes to thin-film electrolytes (NCPEs), there are several benefits over liquid electrolytes. These include reduced corrosion and superior thermal stability, lightweight with excellent mechanical properties, flexibility, ease of manufacturing and processing, and the ability to establish effective electrode-electrolyte contact. A polymer electrolyte based on polyethylene oxide (PEO) and utilising plasticizer, inorganic filler, and alkali salts has been thoroughly investigated. Anion/cation mobility has been demonstrated to occur in the amorphous phase, and its dispersion is facilitated by a multifaceted process involving PEO segmental mobility. To prevent crystallisation, the pure polymer structure must be altered, salt must be added, or regular packing must be inhibited by one or more plasticizers or fillers. Filler added to the PEO/(PEO+salt) matrix is expected to improve PEO's polar properties and increase its electrical conductivity. Filler could be in different places in this system. It can preferentially enter amorphous areas of the polymer and substitute itself on the polymer chain at crystalline or amorphous borders. Furthermore, Magnetic resonance imaging contrast agents, DNA separation, tissue engineering, hyperthermia and magnetic drug targeting have all demonstrated the value of nanoparticles. Because of their special electrical, magnetic, and optical properties, materials with nanoscale microstructures—also known as nanocrystalline materials or nano-composites—are currently seemly more and more significant in terms of technology. Composite polymer electrolytes, such as nano-composite polymer electrolytes (NCPEs), have undergone thorough investigation within the field of electrochemical applications, owing to their capability to improve ionic conductivity. Incorporating another component into these electrolytes, like inorganic/ceramic material, a ferroelectric substance is a common practice in composite polymer electrolytes (CPE). This augmentation aims to enhance the mechanical, electrical, and optical characteristics of the electrolytes. This multifunctional response of material may hold great promise for the development of better materials for electrical and mechanical devices, such as Seals, sensors, loudspeakers, dampers, and magneto-resistive damping. High magneto-electronic sensitivity is seen in polymer ferrite nano-composite films due to the strong magnetism of the filler components. These polymer magnets are widely employed in many different industries, such as audio equipment, home tools, and electronic and communications devices. Ferrites' characteristics render them an effective filler for the creating nano-composites intended for electrochemical uses, including PEM fuel cells and regulated medication distribution systems. We have explored how drug delivery systems can be designed to adjust their delivery rate in response to changes in the surrounding environment, which is one of two approaches. Specifically, our research has focused on understanding the transport properties and structure of nano-dispersed proton-conducting polymer composite electrolytes (NCPEs) under varying conditions. The soft chemical process (sol-gel method) was used to create the material at the nanoscale. SEM, optical microscopy, DSC, and X-ray diffraction (XRD) have all been used in morphological and structural studies of CPE. Impedance spectroscopy was utilized to assess the electrical conductivity of the solution.

2. Materials and Methodology: Polymeric nanocomposite electrolytes based on polyethylene oxide (PEO) (M.W. ~6×10^5, ACROS Organics) have garnered extensive

research attention. This is primarily attributed to their singular helical structure, which promotes rapid ion transport and facilitates ionic conduction [4-6]. PEO has an inverse solubility relationship in the vicinity of the water's boiling point, despite being fully soluble in both warm and cold water [7]. Thus, at 98°C, the resin becomes insoluble in water and precipitates. In solution, PEO gives a pH ranging from 6.5 to 7.5 and is completely soluble in certain organic solvents such as chlorinated hydrocarbons. Limited solubility exists in a wide variety of other organic solvents *e.g.* acetone, anisole, butanol, butyl acetate, ethanol, isopropanol etc. The degree of crystallinity is likely to vary during material processing such as shearing and tableting. Electrochemically, they are classified as non - ionic polymers. The decomposition products of PEO are carbon monoxide and carbon dioxide [8]. They have a bulk density of, 500 kg/m^3 and contain less than 3% of silicon dioxide and 1% of volatiles. PEOs are tough, crystalline polymers at room temperature, and their glass transition temperature decreases slightly with increasing molecular weight from -45 to -53 °C. They are nontoxic, nonirritant, and do not generate residue, sediment, or vaporous elements [9]. Nonetheless, the conductivity of the electrolyte based on PEO is restricted by high crystalline phase concentration. This phenomenon primarily arises from the fundamental necessity for conduction, wherein the motion of ions is intricately linked to the segmental motion of flexible amorphous polymer phases [10–12]. Despite PEO's widespread industrial use and significance, the ionic conduction mechanism is still unclear. These favorable properties, unresolved condition mechanism and broad applicability of this polymer ranging from drug delivery systems [13] to super capacitors and solid-state batteries prompted to consider PEO as the host matrix for formation of nanocomposite polymer electrolytes. With the mindset of developing proton conducting electrolytes among various alkali salts ammonium salt namely Ammonium thiocyanate (NH_4SCN, Rankem India) of AR grade was selected for synthesis of polymer electrolytes and nanocomposite polymer electrolytes [14, 15]. Preference to NH_4SCN was given owing to its following distinctive properties. It readily dissolves in water, alcohol, methanol, and acetone. It is possessing low dissociation energy and easily dissociated on the application of small DC potential. It also contains smaller cation size and bigger anionic size. It is easily melted at 149.5ºC temperature and PH ranging between 4.5 to 6.0. Among the varieties of solvent water was taken as solvent to prepare polymer electrolytes and nanocomposite polymer electrolytes. The most prevalent substance on Earth, water was chosen as a protic and polar solvent for the creation of electrolytes because of its advantageous formation film-forming qualities. According to survey of literature varieties of inorganic oxides have been tried to develop composite polymer electrolytes like NiO_x, TiO_2, SiO_2, Al_2O_3, $BaTiO_3$, $SrTiO_3$ etc. [16-26]. Among these dispersoids, SiO_2 was undertaken as dopant filler for the development of NCPE owing their most abundance on Earth surface and it's possessing acidic behavior of filler particles. Besides the new varieties of dispersoid, namely, ferrites, was chosen in present studies. Among the various inorganic/organic inert fillers, ferroelectric fillers (ferrites) can be used as filler particles due their unique properties. Within the class of inorganic fillers, ferrite is thought to be another strong candidate for the formation of NCPE due to its fascinating structural and electrical properties. Filler particles are drawn to ferrite's high dielectric constant below the Curie temperature. Additionally, it exhibits super paramagnetic behaviour, which opens new uses for polymer electrolytes in the biomedical, tissue engineering, and drug delivery fields. After the materials selection, the next stage of experimental investigation involves synthesis of nanoparticles followed by development of electrolytes.

2.1. Synthesis of Nano Dispersoids: Over the year's variety of techniques have involved for the development of nano fillers and electrolytes as outlined under Chemical

reaction technique, heat-assisted chemical reaction technique, sol-gel technique, chemical precipitation, hydrothermal technique, chemical vapor deposition, laser ablation technique, arc dis-arc technique, ball milling technique, solution combination method, and ultrasonic technique. Among these techniques sol gel technique is relatively low-cost simple technique and has been preferred for present investigations. In general, ceramic oxides can be produced using the sol-gel method, employing both ex-situ and in-situ approaches. In the current study, an ex-situ process has been selected for the development of ferrite filler nanoparticles. However, silica nano-dispersoids were synthesized using an in-situ process. The nano size ferrite powder was synthesized following wet chemistry route (sol-gel process). A variety of nitrates, such as $Al(NO_3)2{\cdot}6H_2O$, $Mg(NO_3)2{\cdot}6H_2O$, $Fe(NO_3)3{\cdot}9H_2O$, and $Zn(NO_3)2{\cdot}6H_2O$ (all in AR grade), have been employed as starting reagents to generate Al_2+, Mg_2+, Fe_3+, Zn^2+, and Fe^2+ ions in a liquid solution. In this process, Al, Zn, Mg, and Fe nitrates (Rankem India) were dissolved in a mixture of water and ethanol, followed by the gradual addition of tetraethoxysilane (TEOS) and mixing at room temperature for a duration of 50-60 hours, with the molar ratio of EtOH = 3: 1: 10 TEOS: H2O [27,28]. The solution's pH was maintained between two and three. At 40ºC, the sols were left to gel. Following jellification, it was dried for fifty hours at 150 degrees Celsius. The powdered gels were then heated in a Canthal high temperature furnace to 700ºC for three hours and 1000ºC for two hours. To create fine ferrite powder (such as Zn ferrite nano power, Mg-Zn ferrite, and Al-Zn ferrite), the dried material was crushed. Tetraethyl orthosilicate (TEOS, Aldrich) was utilized as the starting material, ethanol as the solvent, and ammonia solution as a catalyst to create ceramic filler (SiO_2). TEOS underwent a two-step hydrolysis process to generate nano fillers of SiO_2. Through the implementation of a two-step sol-gel method, nanosized ceramic filler (SiO_2) was created. The sol-gel solution formed was continuously agitated for a duration of ten hours while being mixed in a stoichiometric manner in PEO solution (PEO disintegrated in de-ionized (DI) water at 40°C). Afterwards, we add salt (NH_4SCN) to the PEO-SiO_2 solution in the calculated ratio. Finally, a polypropylene dish was filled with this gelatinous polymer solution. Additionally, NH_4SCN was mixed stoichiometrically to a solution of PEO and SiO_2 in DI water to synthesise the polymer electrolyte sheets. Ultimately, room temperature drying of the solution cast film produced free-standing CPE films.

2.2. Sol-Gel Technique: The so-called sol-gel process involves the addition of polymers or gellifying chemicals, the development of an accompanying network of polymeric or polymetallic species in situ during the drying phase, or both. The acronym "sol-gel" originates from the term "solution-gelling," denoting the fundamental concept of the process where a liquid phase containing dissolved precursors transforms into a solid state via series of chemical reactions, including polymerization [29–33]. The term "sol-gel," which is another name for "wet-chemical," describes a broad range of reaction techniques used in the manufacture of numerous distinct products using a diverse range of chemical precursors [34]. Kakihana states that there are basically three types of sol gel routes: (a) colloidal sol-gel route; (b) inorganic sol-gel routes and (c) organic sol-gel routes [35] and briefly outlined below.

2.2.1. Colloidal Sol-Gel Method: This method requires the dispersion of colloidal particles. By managing the steric or electrostatic transactions among the colloidal particles, the sol can be transformed into a gel [36–37]. The colloidal sol-gel method is known as a "physical" gel pathway due to the prevalence of real forces such as Van Der Waals forces, electrostatic forces, and Brownian motion in the inter particle interactions within these sols.

2.2.2. Inorganic Sol-Gel Method: There are essentially two methods for creating inorganic polymeric oxide gels: either using metal alkoxides dissolved in organic solutions or

using metal salts mixed in organic or aqueous solutions stabilised with chelating ligands. The strong electropositive nature of the metal cations dominates the chemistry in both situations.

2.2.3. Organic Sol-Gel Method: An organic polymeric network is formed in the third sol-gel pathway. There are two ways to go about doing this. The first is an "in-situ" polymerization method in which organic monomers are polymerized to create the gel network. When performed in with metal ions, it is expected that all metal ions will be uniformly distributed throughout the organic polymeric network. The term "polymerized complex method" refers to a procedure that combines "in-situ" polymerization with the creation of metal-chelate complexes. The alternative method, known as "polymer precursor method," involves forming a thick solution containing metal ions, polymers, and a suitable solvent. The procedure includes creating the initial solution, forming a gel, converting organic materials through pyrolysis, and producing an amorphous oxide with low-temperature heat treatment; followed by compaction and transformation into the desired oxide phase with high-temperature heat treatment. An adaptable strategy for producing nanocomposite materials that conduct protons involves incorporating inorganic substances into a polymer membrane through in situ synthesis using the sol-gel technique [38]. It allows for low-temperature synthesis at nano- to sub-micrometer sizes, and the membranes produced by this process are often homogenous. The procedure should ideally start at room temperature when a molecular precursor solution is infused in the polymer matrix. The aqueous solution within the membrane proceeds to interact with the inorganic molecules, leading to the hydrolysis of the penetrating inorganic precursor. Subsequently, the membranes undergo treatment with suitable reagents to complete the condensation reactions. Presently, common precursors employed in the formation of hybrid organic–inorganic composites include TMOS and TEOS. These precursors typically exhibit limited compatibility with biopolymers, posing a challenge when utilizing them. These precursors are poorly soluble in water, which makes the supplement of organic solvents necessary and the source of the constraints. Additionally, alcohol is produced during the sol-gel process, and these precursors must operate in conditions with extremely high or low pH.

The formation of silica nanocomposite materials can be shown by the following scheme:

Precursor + H_2O *Hydrolysis* → Silanols *Condensation* → Sol *Cross-linking* → Gel

The plan consists of three main phases [39-40]

(i) The hydrolysis of the alkoxide occurs following its combination with water.

(ii) Condensation of the siliconol hydrolysis products results in oligomers organised in the shape of sol particles.

(iii) The sol particles cross-linking, which causes a change into a gel state.

The following reaction provides a general illustration of hydrolysis:

$$Si(OR)_4 + nH_2O \rightarrow (HO^-)nSi(-OR)_{4-n}nHOR \quad \ldots\ldots\ldots(1)$$

Where R = hydrocarbon radical and $n \leq 4$.

An alkoxyl group is substituted with a hydroxyl group to produce a silanol group (Si-OH). A silanol group acts as the exclusive mediator of condensation, with two primary pathways identified by the general reactions that follow:

$$(RO-)_{4-n}Si(-OH)n + (HO-)_nSi(-OR)_{4-n} \rightarrow (OH)_{n-1}(RO-)_{4-n}Si-O - Si(-OR)_{4-n}(OH)_{n-1} + H_2O \ldots\ldots\ldots\ldots\ldots(2)$$

and

$$Si(-OR)_4 + (HO-)_nSi(-OR)_{4-n} \rightarrow (RO-)_3Si-O - Si(-OR)_{4-n}(OH)_{n-1} + HO - R \ldots\ldots\ldots(3)$$

The result in each case is a dimer consisting of a few silicon atoms connected by a siloxane link. Condensation reactions involving the dimer can result in the creation of a trimer,

tetramer, and further. However, the process ends there, leaving only oligomers, or oligosiloxanes, as the product. They are ordered as colloid particles with nanoscale dimensions (sol) in the bulk fluid. The resilience of the sol to the coagulation at almost neutral pH is influenced by the negative charge on the particle surface.

The linking of particles constitutes the third phase, where the sol-gel transition occurs. This is facilitated by the condensation reactions (2) and (3), which cross-link them; a catalyst is typically needed to accelerate this process. Processing is frequently started by adding acid or alkali to the solution because the coagulation's negative charge, which is pH-dependent, causes the sol stability.

2.3 Synthesis of Polymer Electrolyte/ Nanocomposite Polymer Electrolytes (NCPEs): Many methods have been developed throughout the years after the initial study on polymer electrolytes. The prominent over are, Solution cast technique, Sol-gel technique in liquid electrolyte medium, Polymerization in the presence of liquid electrolyte medium, Soaking of liquid (LML)/liquid electrolyte in polymer Electrolyte/Polymer matrix and Phase inversion method.

2.3.1. Solution Cast Technique: Many methods have been developed throughout the years after the initial study on polymer electrolytes. Solution cast method is the most common, easy to use and cheapest technique used for preparation of polymer electrolyte films. Comparative study for the synthesis of nanocomposite polymers i.e.
Sol-Gel Processing of Polymers book provides a comprehensive introduction to the sol-gel technique applied specifically to polymers. It covers fundamental principles, processing methods, and applications, including nanocomposite synthesis [41]. Sol-Gel Science: The Physics and Chemistry of Sol-Gel Processing book discusses the fundamental science behind sol-gel processes. It covers both inorganic and organic-inorganic hybrid materials, providing a solid foundation for understanding the sol-gel technique [42]. Sol-Gel Nanocomposites review article discusses the synthesis and properties of nanocomposites prepared using the sol-gel technique. It highlights the advantages of sol-gel processing in achieving nanoscale control over material properties [43]. In this method, stoichiometric proportions of the polymer and additive salt/acid are mixed separately in suitable selected solvent. The two solutions are subsequently mixed and stirred together for certain duration of time at elevated temperature to form homogeneous viscous solution. Third component filler particle are dispersed heterogeneously to achieve the composite polymer electrolyte and continuously stirred for 8-10 h. This solution is then cast on a Teflon/Polycarbonate mould to remove solvent by slow evaporation in air at room temperature. This solution cast film was first dried in a BOD incubator at a constant temperature of 30 °C to produce the solvent free-standing films of NCPEs. It was then dried in a vacuum. It is already widely known that the type of solvent used, how quickly the solvent is removed, and the presence of leftover solvent all have a substantial influence on the morphology of the resulting polymer electrolytes. In addition, present impurities (mostly water), atmospheric condition and thermal treatment history further complicated the situation. Thus, it is essential to overcome these problems so that all the complexes same type exhibits similar phase diagram and other related properties. Therefore, consistency is extremely important while using this technique for preparation of polymer complexes. However, in practice there are no universally acceptable common criteria. Although several other techniques have been adopted by various researchers, they have not gained popularity due to their inherent drawbacks. In conclusion, it is possible to produce polymer electrolyte films of the required thickness with consistent reproducibility by carefully choosing the solvents and managing the entire synthesis process. Considering this, the solution casting technique has been used in the present investigation (Figure-1).

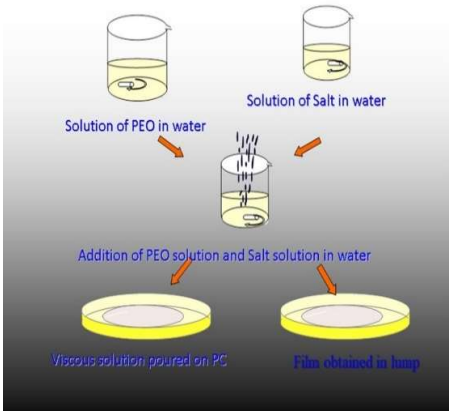

Figure-1 Synthesis of nanocomposite polymer electrolyte films

3. Characterization Techniques: As mentioned in previous section, it is necessary to characterize the material for structure, morphology, thermal behavior & mechanical, electrochemical, and electrical behavior to draw precise structure property correlation ship. This is pertinent to draw conclusion regarding applicability of materials in devices. Within the framework of ionic materials following techniques are usually employed to characteristics the material.

- ***Structure and Morphology:***

Optical microscopy, Infrared (IR) spectroscopy, Electron microscopy: SEM, TEM, and X-ray diffraction.

- ***Thermal Characterizations***

Thermo-gravimetric analysis, Differential thermal analysis and Differential scanning calorimetry, DMA/TMA, and Thermo-electrometry.

- ***Ion transport (Macroscopic)–Electrical Characterization Techniques***
- ***Transference and mobility measurement***

Wagner's polarization, Hittorf electrolysis, Coulometric analysis, combined ac/dc technique, Electro-gravimetric analysis, Transient ionic current measurement, and TCP and Electro-chemical potential measurement.

- ***Electrical Conductivity***

Complex impedance spectroscopy, two terminal dc technique with blocking electrode, four probe dc technique non-blocking electrode, two terminal ac technique or four terminal ac method, two terminal dc technique with non-blocking electrode and contact free induced torque method

- ***Diffusion Techniques***

Mass spectroscopy, Characteristic light absorption measurements, Spectro-photometric method, Electron spin resonance signal intensity measurements, radioactive tracer diffusion technique, Pulse field gradient NMR,

- ***Thermo-electric power, Electron microprobe technique,***
- ***Dielectric spectroscopy***
- ***Other conductivity related measurement***

(i)Viscosity measurement, (ii) pH measurement, (iii) Volume tracti-measurements-psychometric method (iv) Swelling and swelling kinetics

- ***Ion transport (microscopic)***

NMR line width and relaxation time, Quasi-elastic neutron scattering, Diffused x-ray and neutron scattering, Microwave and radio frequency relaxation spectroscopy, Raman scattering, Brillion scattering, Though, all these techniques have been described in standard texts, review papers and reporting of various workers, the techniques employed in the present investigation for characterization of nanocomposites polymer electrolytes would now be briefly described for coherence of presentation. A comparative study for characterization technique is cited below: Advanced Characterization Techniques for Nanocomposites review article provides an overview of advanced characterization techniques such as TEM, SEM, AFM, XRD, and spectroscopic methods applied to nanocomposites. It discusses recent advancements and their applications in understanding nanocomposite structures and properties [44]. Characterization Techniques for Polymer Nanocomposites: A Review discusses a wide range of characterization techniques used for polymer nanocomposites. It includes microscopy, spectroscopy, thermal analysis, mechanical testing, and surface analysis techniques, providing insights into their applications and advancements [45].

3.1. Structural Characterization: Structural characterization is crucial for understanding the formation of nanocomposite polymer electrolytes. In structural characterization, one can study physical/chemical structure and variety of concept describing the arrangement of building blocks of materials. Therefore, structural investigation constitutes on essential component of nanocomposite material research. As indicated earlier different scattering, spectroscopic, scanning and transmitting tools for structural characterization of materials have been developed over the decades. The morphological studies are yet other factor for the routine investigations of nanocomposite polymer electrolytes to obtain important information regarding association of structural units within nanosized structures. The techniques used for these investigations in present work would now be overviewed.

3.1.1. X-Ray Diffraction (XRD): A very efficient and widely available method for figuring out the atomic arrangement in materials is X-ray diffraction (XRD). Because of this, it is a flexible and often used instrument in solid-state physics to study the complex structures of matter. For the structural characterisation of materials in all forms, from powder, bulk, and films to single crystals, X-ray diffraction has proven to be an effective approach [46]. Besides this technique can be used in stress measurement study of phase equilibrium, determination of particle sizes and its orientations in crystal or ensembles of orientation in polycrystalline aggregate [47]. In case of polymers, polymer electrolytes and polymer nanocomposite electrolytes it has been used as routine investigation technique for elucidation of structure [48, 49]. Polymer nanocomposite electrolytes contain complex nano/micro heterogeneity scattering center with variable amount of crystalline and amorphous phases. Since the inorganic phases in nanocomposite electrolytes produced by the thermal breakdown of molecules typically have a crystalline form, wide angle X-ray powder diffraction is a straightforward method for identifying them. Such polymer-embedded nano-crystals have a broad diffraction pattern due to the small size of their crystalline domains (less than 50 nm). Furthermore, peaks in a nanocomposite sample often have modest intensities since the amount of inorganic phase in the sample is typically low. The majority of nanocomposite diffractograms have a low signal/noise ratio and only those signals that correspond to the most abundant crystallographic planes can be recognised. Only by utilising X-ray sources with sufficient anti-cathode materials and a modest angular movement of the detector can good quality diffraction data be obtained. Since nanoparticles are often single crystals, the distribution of peak intensities may also provide information about the shape of the particles, and the broadening of diffraction peaks permits an approximative assessment of crystallite size using Scherer's formula. Scherer's formula can be applied to determine the crystallite size from a diffraction pattern.

$$L = \frac{0.9\lambda}{\beta \cos\theta} \dots\dots\dots\dots (4)$$

Where L= the thickness of crystalline involved in diffraction of x-ray

λ= wavelength of X-ray

β= full width at half maxima of intensity and known as angular broadening and expressed in radians

θ= angle at maximum intensity for concerned peak

The main components of a typical XRD system are the X-ray source and detector. They are positioned around a circle known as the focusing circle, with the specimen positioned in its centre. An evacuated x-ray tube's metal target anode is the target of a high-voltage electron beam directed towards the source of x-rays. The x-ray protons of a given energy can be calculated by the detector for each angle 2θ, which is a proportionate reflection of the peak intensity. The relationship between the diffraction angle, atomic separation (d), and wavelength of the impinging X-ray beam is described by the Bragg equation (figure-2a).

$$2d \sin\theta = n\lambda \ldots\ldots\ldots (5)$$

Here, "n" represents an integer denoting the order of the diffraction peak.

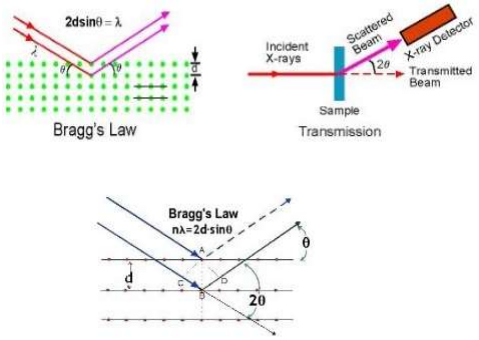

Figure 2(a). Bragg's diffraction of X-ray satisfying the interplanar distance (b) in crystalline materials [50]

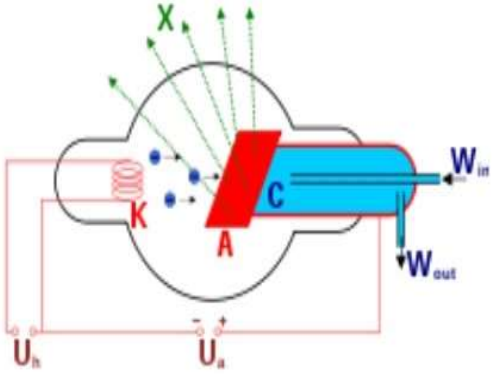

Figure 2(b). Diagram of water-cooled X-ray tube [51]

When using powder XRD, the sample is often made up of tiny grains of the single-crystalline substance that is being examined. This method is also frequently used to investigate polycrystalline solids (both bulk and thin film materials) as well as particles in liquid suspensions. This XRD technique was used in the current study to investigate the following parameters: Determining the configuration of crystalline substances involves assessing properties such as crystallographic axes, dimensions, and morphology of the fundamental unit, as well as the spatial arrangement of atoms within said unit; discerning the disparities between crystalline entities and disordered materials; and quantifying deformation and minute grain dimensions.

Using these parameters inferences would be drawn for complexation behavior of components present in nanocomposite electrolytes. The shift in peak intensity is due to change in interplanar spacing at diffraction angle (2θ) which gives information of complexation behavior and the variation in d values for diffraction pattern provide some information regarding the change in crystalline structure of samples. To distinguish the impact of broadening caused by crystallite size from that caused by strain on the Full Width at Half Maximum (FWHM) of the XRD profile, researchers use the Williamson-Hall plot method [52]. This method involves calculating the crystallite size using a relationship derived from the Sinθ vs. β Cosθ plot

$$\beta \cos\theta = \frac{C\lambda}{L} + 2\varepsilon \sin\theta \ldots\ldots\ldots (6)$$

where β =FWHM (full width at half maxima of intensity)

L= the grain size, C= the correction factor, ε = the strain λ= the wavelength of X-ray.

3.1.2. Optical Microscopy (OM): A microscope (figure-3) is a device utilized for observing tiny objects. Microscopy is the discipline dedicated to the examination of diminutive entities using such a tool. As the original and most widely used form, the optical microscope is well-known in this domain. This optical device has one or more lenses that, when an object is put in their focal plane, produce a magnified image of that thing. Using the optical theory of lenses, optical microscopes enlarge images that are produced when a wave passes through or is reflected off a material. A typical magnification of a light microscope, assuming visible range light, ranges up to 1500x, with a theoretical resolution limit of around 0.2 micrometres or 200 nanometres [53-54].

A specific type of micro-projection called photomicrography uses a detector to record

images of microscopic specimens that have been magnified by a microscope.

Figure 3. A Typical Optical Microscope [55]

The silver halide emulsion on glass or film served as the main photomicrography media for much of the 20th century. Since nearly the dawn of photography, these materials have faithfully reproduced countless images taken with an optical microscope, which has been of great assistance to the scientific community. Photomicrography is a phrase that can be used interchangeably with microphotography, which is the usual term for the technique of creating miniature images of huge items, including microfilms of books and documents. More specifically, the characteristics of the imaging device are important in defining the resolution that is obtained and the dynamics of the specimen visualisation [56].

3.1.3. Scanning Electron Microscope (SEM): An image of a specimen that has been electronically enlarged for close examination is produced by an electron microscope. The specimen is illuminated and a magnified image of it is produced by the electron beam used by the electron microscope (EM). In comparison to an optical microscope driven by light, the microscope has a higher resolving power (magnification) because it employs electrons with wavelengths that are around 100,000 times shorter than visible light (photons). Light microscopes are limited to magnifications of 1000x, but this one can reach up to 3,000,000x. A scanning electron microscope (SEM) produces various signals at the surface of solid objects by focusing a high-energy electron beam. The ray diagram of a typical scanning electron microscope is shown in the figure. SEM signals, generated by electron-sample interactions, provide information about the sample's materials, including their orientation, crystalline structure, chemical composition, and external morphology (texture). Most applications entail the collection of data across a specified portion of the sample's surface to generate a 2D image illustrating the spatial variations in these characteristics. Traditional SEM techniques are capable of investigating regions with widths ranging from approximately 1 cm to 5 microns in a scanning mode (with magnification levels from 20X to around 30,000X and spatial resolution of 50 to 100 nm). Also, the SEM can analyse points on the sample for purposes such as determining chemical compositions, crystalline structure, and crystalline orientation in a semi-quantitative or qualitative fashion. The Electron Probe Micro Analyzer (EPMA) and the SEM share many functional similarities, as well as a significant amount of capability overlap. The range of signals generated by electron-sample interactions includes Heat, secondary electrons (which create SEM images), backscattered electrons (BSE), diffracted backscattered electrons (EBSD), and photons (including distinctive X-rays used for elemental analysis). Secondary electrons and backscattered electrons are two of these radiation types that are frequently utilised to image samples. Backscattered electrons are particularly helpful for presenting morphology and topography on materials, while they also emphasise compositional contrasts in multiphase samples or for fast phase discrimination [57–58].

The SEM (depicted in Figure-4) facilitates precise measurement of exceedingly minute features and objects, with the capability to discern sizes as small as 50 nm.

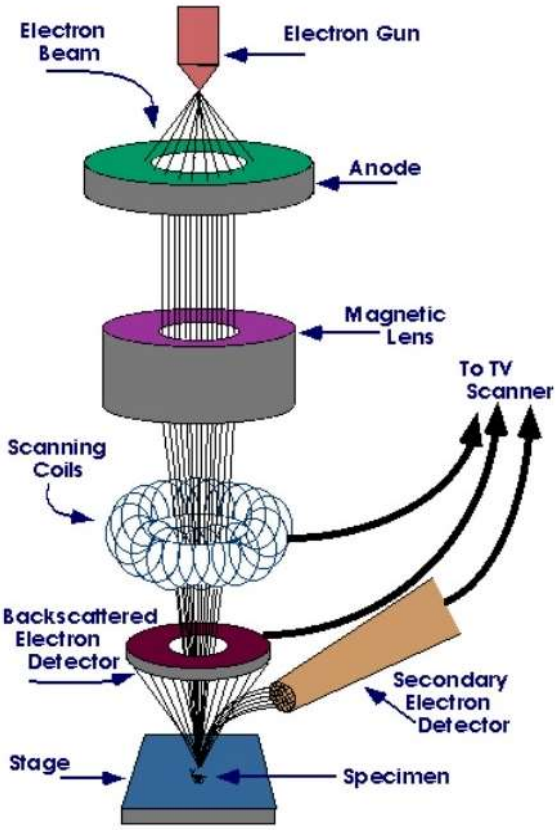

Figure 4. Ray diagram of scanning electron microscope (SEM) [59]

3.1.4. Infrared Spectroscopy: Finding the source of a pollution issue often requires first identifying an unknown material's chemical composition. The identification method might be especially difficult if the contaminant is organic in nature because there are thousands of different chemical components. Many contaminants are mixtures of two or more substances, making it more challenging to identify unknowns. Therefore, spectroscopic techniques like IR, NMR, and UV Raman Spectroscopy etc. have become many popular and most convenient probes for determination of local structure. Fourier Transform Infrared spectroscopy (FTIR) is a significant method among these spectroscopic approaches that is highly beneficial for the characterisation of organic materials. The presence of chemical structures can be inferred from the FTIR spectra [60]. It is a simple method of determining whether a molecule contains a particular functional group. Additionally, the distinct set of absorption bands can be used to identify specific contaminants or validate the identity of a pure molecule. An additional method to IR spectroscopy is Raman spectroscopy [61]. The principle behind Fourier Transform Infrared (FTIR) Spectroscopy is that nearly all molecules absorb infrared radiation. Monatomic molecules (such as He, Ne, Ar, etc.) and homopolar diatomic molecules (like H_2, N_2, O_2, etc.) are the sole types that do not absorb infrared light. Only those wavelengths of infrared light that alter a molecule's dipolar moment do molecules absorb it. The dipolar moment of a molecule is created by the variations in charges in the electronic fields of its atoms. Infrared photons can interact with molecules that have a dipolar moment, exciting them to higher vibrational states. Due to the equal electronic fields of all its atoms, homopolar diatomic molecules lack a dipolar moment. Since monatomic molecules only contain one atom, they do not have a dipolar moment. Therefore, infrared light is not absorbed by homopolar, diatomic, or monatomic molecules. Nevertheless, nearly every other molecule absorbs infrared light. Infrared spectroscopy primarily involves measuring the intensity of the infrared light spectrum that remains after passing through a sample, achieved by dispersing it using a Michelson interferometer. In FTIR spectroscopy, multiplexing allows for the simultaneous monitoring of all optical frequencies emitted by the source over a period. The electromagnetic spectrum's infrared region is typically segmented into three distinct areas: near-infrared, mid-infrared, and far-infrared, categorized based on their closeness to the visible light spectrum. The microwave region is adjace't to the low-energy far-infrared (400–10 cm−1; 1000–30 μm), which is suitable for rotational spectroscopy. Mid-infrared, roughly spanning 4000–400 cm−1 (30–2.5 μm), is where fundamental vibrations and their rotational-vibrational structures are studied. Near-infrared, with energies around 14000–4000 cm−1 (2.5–0.8 μm), can excite overtone or

harmonic vibrations. It is crucial to remember that these subregions' labels and categorization are purely traditional. They are not based on

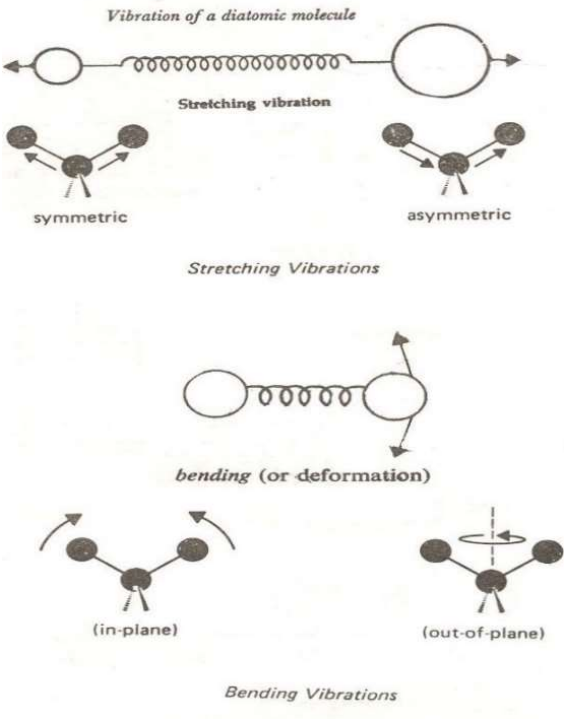

Figure 5(a). Vibration modes of molecules [62]

chemical or electromagnetic properties, nor are they well characterised. Molecules may perform stretching and bending of following type and as illustrated in figure -5(a).

The characteristics of stretching vibrations, including symmetric and asymmetric stretching vibrations, as well as bending vibrations such as Scissoring, Rocking, Wagging, and Twisting, can be observed in the absorption versus frequency profiles of infrared light passing through a sample. This serves as a unique fingerprint of the molecular structure, facilitating the identification of different compounds. To identify chemical bonds and groups in a complex molecule, molecular vibrations are detected and measured to retrieve information about structure and interaction. The compositional modification due to mass transport, heat, irradiation effect can also be detected by monitoring IR spectra [63-64]. Fraction of free ion and ion pair in polymer electrolyte can also be evaluated using IR spectra [65]. An infrared spectrum is typically analyzed in two distinct regions, namely:

(a) Finger print region 1300-650 cm^{-1}: The reason this region has its name is because no single compound absorbs in this fashion. Since both stretching and bending modes can result in absorption in the 1300–909 cm-1 area of the IR spectra, the intermediate section of the spectrum is typically complicated. Due to their nearly identical energies, single bonds are typically responsible for the formation of absorption bands in the finger print region. The absorption bands are thus composites of strong interaction which occurs between neighboring bonds and depends upon overall skeleton structure of molecule.

(b) Functional group region 4000-1300 cm^{-1} : Certain regions of the infrared spectrum correspond to characteristic stretching frequencies of significant functional groups. Infrared spectra of substances are also affected by the physical state, electronic environments, interaction that takes place between molecules, and lattice vibrations [66-68]. Therefore factors, like hydrogen bonding, coupling of oscillation and Fermi resonance electronic environment in immensely affect the position of absorption line. Table 2.1 broadly shows correlation bands to identify structure of the substance. Figure-5(b) shows basic diagram of a double beam infrared spectrometer normally used in IR studie

An infrared laser beam can be used to measure a sample's infrared spectrum. By examining the transmitted light, the quantity of energy consumed at each wavelength is calculated. This can be done with a device that measures all wavelengths simultaneously using the Fourier transform or with a monochromatic beam whose wavelength Variations over Time. A transmittance or absorbance spectrum that shows the infrared wavelengths absorbed by the material is the result. Understanding the sample's molecular structure is possible through analysis of these absorption properties.

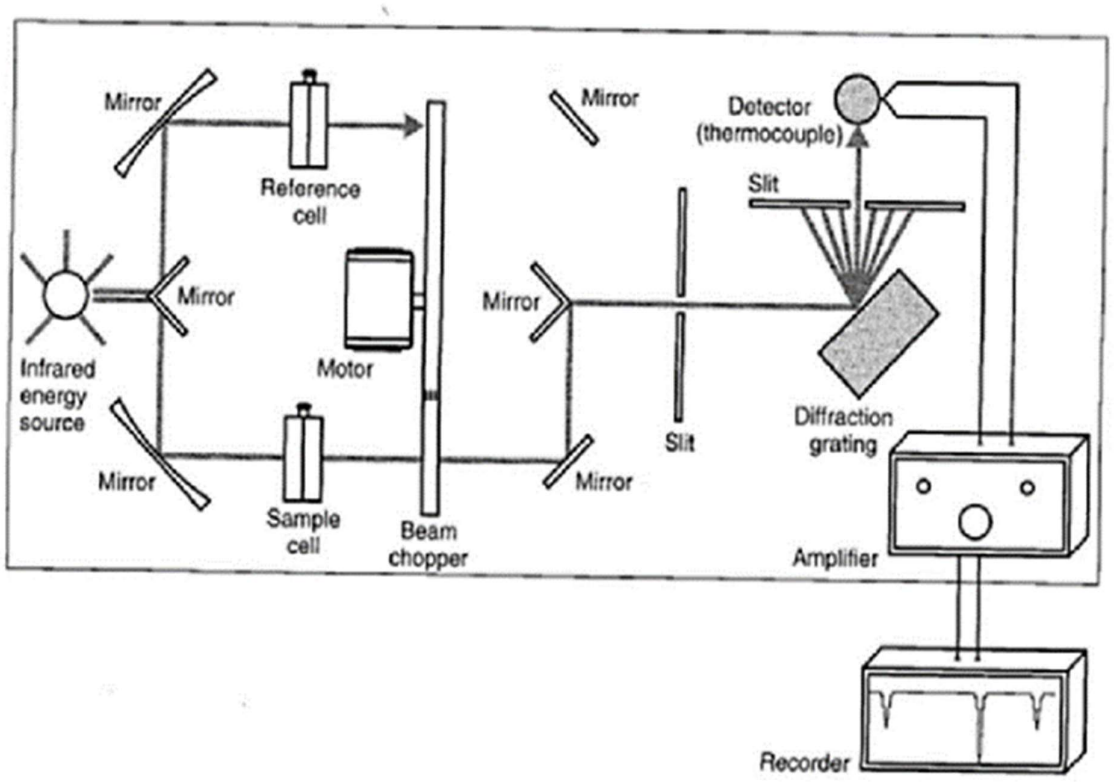

Figure 5(b). Schematic diagram of an infrared spectrophotometer [69]

3.2. Thermal Characterization: Thermo-analytical techniques offer a well-established methodology for researching the thermodynamics of numerous processes involved in a wide range of sectors encompassing both industry and research, as well as for thermal characterisation of materials. With these methods, the sample being studied is put through a predetermined cycle of heat, cool, and isothermal phases in a furnace's-controlled environment. Accurate measurements are taken of the changes that take place in various parameters of interest in a relation to temperature and pressure. The physico-chemical processes that occur with temperature are characterised by the profiles of these parameters. Many thermal analysis tools are used in various fields of materials science, chemistry, and metallurgical and chemical engineering [70-71]. Some of the widely used thermal techniques are listed below. DTA –Measures temperature excursion of sample [variable – dT/dt], DSC – Measures heal flow into or out of sample [variable – dH/dt], TGA –Measures sample weight change with temperature [variable – m; dm/dt], TMA – Measures change in physical dimensions of sample as a function of temperature [Variable – L; dL/dt], The measurement of the parameters of a material in this manner give valuable information regarding-Purity determination, Oxidative stability, Melting/crystallization behavior, Glass transitions, Solid-solid and liquid transitions, Phase transition and Morphology, Polymorphism, Crystalline Amorphous, Degree of Crystallinity, Cross-linking reactions, Specific heat, Thermo kinetics, Decomposition in Liquid Crystal Glass-ceramics polymers, Among different thermal techniques DSC would be described as it has been used practically in the present work.

3.2.1. Differential Scanning Calorimetry (DSC):

It is challenging to get quantitative information about the sample or heat of transition with conventional DTA, but it can provide strong qualitative information about temperature and a transition sign. The significance of usually

unidentified variables, such as the sample's specific heat and thermal conductivities before and after the transition, contributes to this challenge. The region beneath the endotherm or exotherm is further influenced by the rate of heating, thermocouple location, and other instrumental characteristics. By transforming the DTA apparatus's sample container into a differential scanning calorimeter, quantitative data can be achieved. An experimental method for determining the energy required creating an almost zero temperature difference between a test substance S (and its reaction products) and an inert reference material R is called differential scanning calorimetry, or DSC.

This is done by exposing the two samples to the same (heating, cooling, or constant) temperature programme. The term DSC originated from this technology, which detects energy directly and allows precise measurements of heat capacity [72–73] (figure 6).

The temperatures of the specimen (TS) and reference (TR) in power-compensation DSC are controlled independently using distinct yet identical ovens. The sample and reference temperatures are kept at zero by varying the power delivered to the two furnaces. This approach determines the changes in enthalpy or heat capacity between the test sample S and the standard R. Conversely, in Heat-flux DSC, a high thermal conductivity metallic block ensures efficient heat transfer between S and R within the same furnace as the test sample S and standard material R, typically an empty sample pan and lid. Variations in temperature compared to R are induced by alterations in the enthalpy or heat capacity of the specimen S. Because of the excellent thermal contact between S and R, this leads to a certain heat-flow between S and R, albeit one that is smaller than those in DTA.

Calibration experiments are used to record the temperature differential (DT) between S and R and then connect it to the enthalpy change in the specimen. The only significant distinction between the heat-flux DSC system and the DTA system is the improved heat-flow channel connecting the reference and specimen

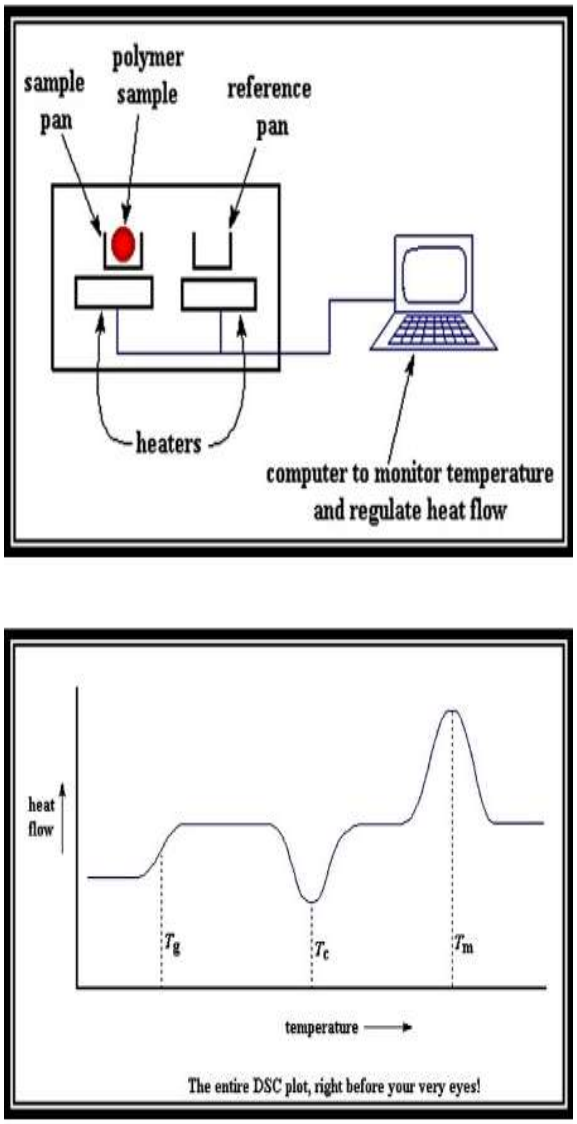

Figure 6. Block diagram Heat Flow DSC [74]

crucibles. DSC is primarily used to examine phase transitions, including exothermic decompositions, melting, and glass transitions. These transitions entail changes in energy or heat capacity, which are highly sensitively detectable by DSC. The fundamental idea behind this technique is that, to keep the reference and sample at the same temperature during a physical change like a phase transition, heat will need to enter the sample. Whether the process is exothermic or endothermic determines how much heat must flow to the sample. For instance, when a solid sample melts into a liquid, more heat must enter the sample for its temperature to rise at

the same rate as the reference. When the sample absorbs heat during an endothermic phase change from a solid to a liquid, this event takes place. Similarly, during exothermic reactions like crystallisation, less heat is needed to raise the sample's temperature. Differential scanning calorimeters can quantify the heat received or emitted during these transitions by measuring the difference in heat flow between the sample and a reference. Glass transitions and other nuances in phase changes can be observed with DSC. Because of its usefulness in assessing sample purity and researching polymer curing, it is frequently utilised in industry as a quality control device. Glass transitions may occur when the temperature of an amorphous solid is elevated. These shifts manifest as a step in the DSC signal's recorded baseline. There isn't a formal phase transition; instead, the sample's heat capacity changes as a result. An amorphous solid will become less viscous as the temperature rises. The molecules might eventually become mobile enough to spontaneously organise into a crystalline structure. We call this crystallisation (Tc). The DSC curve signal peaks because of this exothermic process, which turns the amorphous solid into a crystalline solid. The sample finally achieves its melting temperature (Tm) as the temperature rises. An endothermic peak can be seen on the DSC because of melting. To create phase diagrams for a variety of chemical systems, DSC is a crucial technique due to its capacity to assure transition temperatures and enthalpies.DSC is more limited in its upper operating temperature range (~ 800°C) than DTA, due to increasing thermal emissivity as temperature rises. This effect reduces calorimetric sensitivity and makes high temperature calibration difficult. Sample can be cooled to near liquid nitrogen temperature, which makes this an ideal technique for detecting this low temperature glass and sub-glass transitions in polymers. In DSC, sample encapsulation is extremely important. Sample can be hermetically sealed in pairs with 2-3 atmosphere bursting pressure either with maximum value or with minimum volume. When a volatile sample is used, these pans may burst at different times and bursting time may be dependent on sample size. Volatile sample in crimped (c and d) or open (e) pan will also show variable effects. In addition, parameters that can be studied in DTA, DSC can also be used to study many more parameters related to enthalpy changes and kinetics of phenomenon of material under study. Furthermore, physical phenomenon like determination of phase diagram of polymer substance, monomer purity, glass transition, fractional crystallinity, identification of crystalline phase present, liquid crystalline transition in both main or side chain of polymer, metal-stable equilibrium, free versus bound water in polymer, ferroelectric transition, effect of orientation salting out or salting in and many more parameters can be studied through DSC measurements.

3.3. Electrochemical Studies:

3.3.1. Cyclic Voltammetry Studies:

Verifying the material's electrochemical and window stability is crucial for the electrochemical device applications of nanocomposite polymer electrolytes. offers a wide range of potent voltametric and coulometric techniques for basic research on electrochemical reactions. These techniques are based on sensitive computer-controlled potentiostates and a variety of innovative stationary electrodes and microelectrodes. One of these new techniques that is most useful is cyclic voltammetry (CV), which is widely used in organic, inorganic, and materials research. It is frequently the first experiment conducted in an electrochemical study [75]. Electrochemical measurements of a general purpose are the objective of the Model 600D series CV instrument. The schematic displayed in Figure 7 below illustrates the structure of the device. Components of the system include rapid data acquisition circuitry, a high-speed digital function generator, Potentio stat, and Galvano stat (available in specific models). The device provides a current range of ±250 mA and a potential control range of ±10 V. Currents as low as tens of pico-amperes can be detected by it. It is possible to measure a 10 μm disc

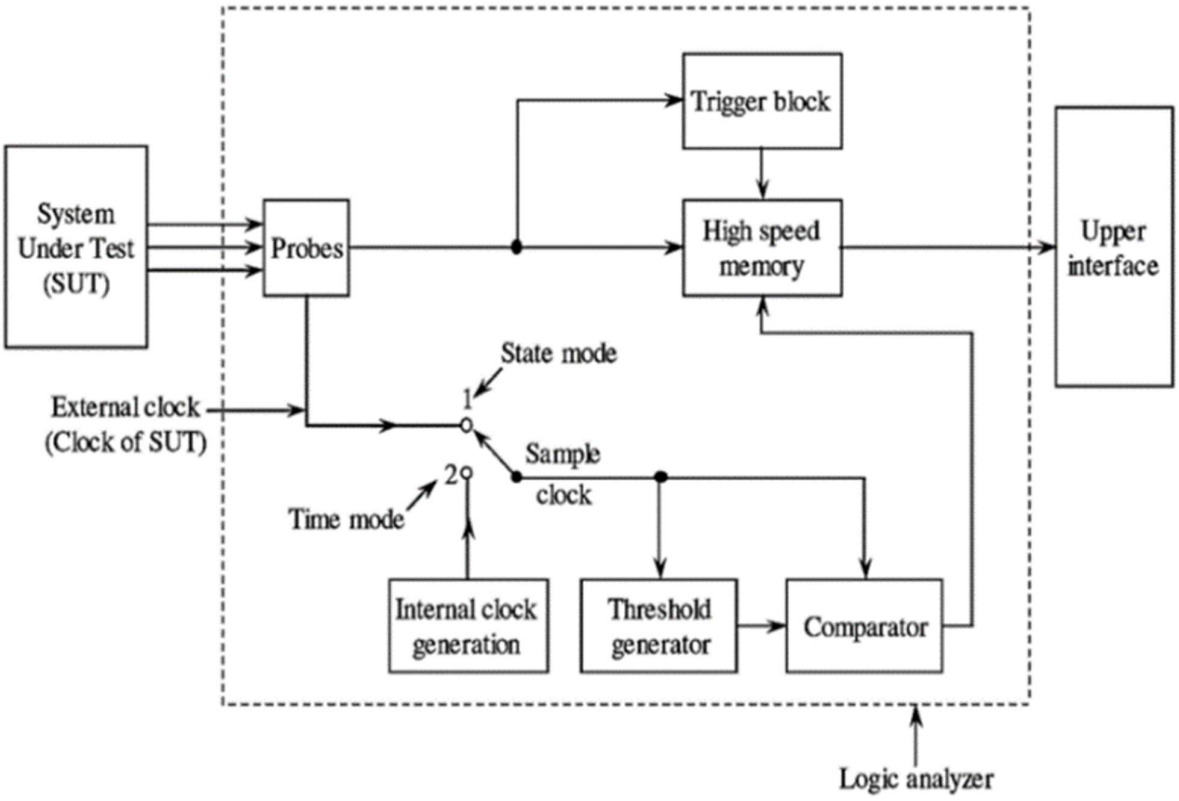

Figure 7(a). Block diagram of CH analyzer Instrument [76]

electrode's steady-state current precisely without the use of external adapters. Currents as low as 1 pA can be measured with the fully automated CHI200B Pico-amp Booster and Faraday Cage, which are compatible with the CHI600D series. The instruments demonstrate high speed capabilities with a function generator that may update at a rate of 10 MHz and a maximum sampling rate of 1 MHz at a resolution of 16 bits. This apparatus offers a wide dynamic range over multiple experimental time frames. In cyclic voltammetry, for illustration, the scan rate can be as high as 1000 V/s with a 0.1 mV potential increment or as high as 5000 V/s with a 1 mV potential increment. With its 4-electrode configuration, the Potentiostat/Galvanostat can be used for liquid-liquid interface measurements and reduces the influence of contact resistance in connections and relays when doing high current tests. The data acquisition systems provide the simultaneous recording of electrochemical data and external input signals, such as spectroscopic signals. The gadget will instantly reset the voltage and current to zero, removing the requirement for routine recalibration. Additionally, it has an authentic integrator chronocoulometric to analyse samples of polymer electrolyte under polarisation. When operating as a bipotentiostat, the second channel can be configured to maintain a constant independent voltage, replicate the voltage of the first channel, or sustain a consistent voltage differential. This additional channel accommodates various voltametric and amperometry techniques, as well as advanced electrochemical workstations and comprehensive electrochemical analyzers. This apparatus offers a range of electrochemical methods, a built-in digital CV simulator, and a program for simulating and fitting impedance. These capabilities offer robust resources for conducting both in-depth studies on electrochemical mechanisms and meticulous analysis of trace elements. The objective of utilizing this method is to thoroughly evaluate the effectiveness and

limitations of this waveform in elucidating electrode reaction mechanisms. The schematic diagram and computer-managed CH workstation are depicted in figure-7a.

Information about the stability and reaction kinetics of these electro-generated species can be obtained from the oxidation and reduction of chemical species at the electrode surface. One method of measuring is the cyclic voltammogram. Three peak currents are measured: the anodic peak current (ipa), the cathodic peak potential (E_{pc}), and the cathodic peak current (i_{pc}). These peak potentials provide information on the analyte's identity as well as the oxidation/reduction process's kinetics in electrolyte systems. Peak current providing data on the stability and analysis concentration of the electro-generated species. A pair of stable chemical compounds that interchange quickly and kinetically when the applied voltage changes at the electrode electrolyte surface is known as an electrochemical reversible redox couple [77]. The formal reduction potential (E°) for a reversible couple is determined by averaging the anodic and cathodic peak potentials, expressed by the following relation:

$$E^o = \frac{E_{pa} + E_{pc}}{2} \quad \ldots\ldots\ldots\ldots (7)$$

The degree of separation between the anodic and cathodic peak potentials can be expressed as the number of ions, n, transported during the kinetics of an electrochemically reversible reaction. This relation can be found here.

$$\Delta E_p = E_{pa} - E_{pc} = \frac{0.0592V}{n} \quad \ldots\ldots\ldots\ldots (8)$$

A cyclic voltagram with a peak separation of 0.0592 V is ideal for this reaction. By using the Randles-Sevcik equation, the cyclic voltagram's peak current magnitude can reveal information about the analyte's concentration.

$$i_p = (2.69 \times 10^5) n^{3/2} A D^{1/2} C V^{1/2} \quad \ldots\ldots\ldots (9)$$

where,

i_p = peak current, n=electron stoichiometry, eq/mol A =electrode area (cm^2), D=diffusion coefficient, cm^2/s, C = concentration, mol/cm^3, v = scan rate, V/s, in above equation, a peak current increase with square root of the scan rate and is directly proportional to concentration. The values of i_{pa} and i_{pc} should be close for a simple reversible couple. *i.e.*

$$\frac{i_{pa}}{i_{pc}} = 1 \quad \ldots\ldots\ldots\ldots (10)$$

If species are generated electrochemically and further chemical reactions take place, the peak current ratio can differ considerably from the predicted value. When waves are semi-reversible in CV the peak current ratio is less than or greater than 1, Figure 7b.

One can estimate ion insertion and extraction can be from the peak area. The area (\(A_i \)) enclosed by each cycle shows the quantity of ion inclusion in the polymeric chain.With the help of observation of the area under the CV peak, the cycle efficiency (Q_i) of electrolytic materials can be evaluated from below equation [78].

$$Q_i = \frac{A_i}{A_1} \quad \ldots\ldots\ldots\ldots (11)$$

Where Q_i *is* the cycle efficiency, A_1 is the area of the first cycle curve A_i the area of i^{th} cycle curve.

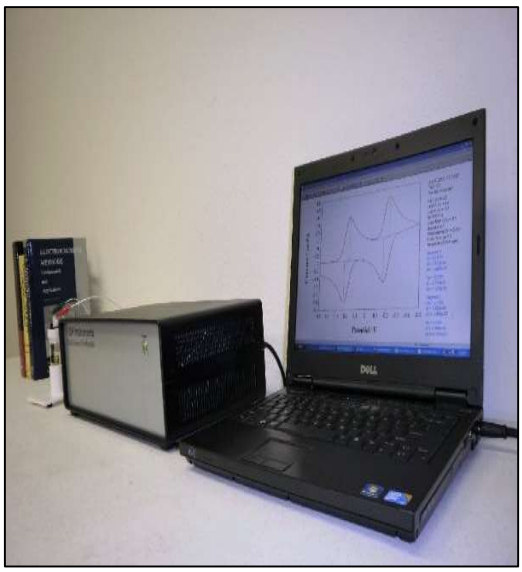

Figure 7(b). Computer controlled CH Workstation

3.4. Electrical Characterization:

3.4.1. Ion Transport Studies:

Ion dynamics of any electrolyte should be well understood before inducting them to any electro-chemical device application. Electrolytes of any form (solid/liquid/semisolid-gel) possess overall electro-neutrality but the ions are free to perform, Brownian motion resulting in net zero current. When electrolyte is subjected to electric field, these random mobile ions start drifting in certain direction viz. direction of electric field leading to conduction of ion. Ion transport dynamics can be understood macroscopically or microscopically. Microscopic ion dynamics corresponds to understanding the mechanism of ion transport at molecular/atomic level in the impact of applied electric field. Macroscopic behavior on the other hand concerns all change in concentration(s) of ion species (s) (or all type of ions) within a specific volume or ion transport through a particular cross-sectional area and it provides property of bulk. Commonly used macroscopic ion transport properties are conductivity, mobility of ionic species, ionic transference number and activation energy. To assess these properties the techniques used in present studies are discussed below.

3.4.2. Transference Number:

The ratio of current produced by ionic species migration, Ii, to the total current resulting from all conducting species, or t_i, is known.

$$t_i = \frac{I_i}{I_t} \dots\dots\dots\dots (12)$$

If we assume σ_i to be the conductivity due to all type of ions and σ_t the total conductivity encompassing ionic as well as electronic parts ($\sigma_t = \sigma_i + \sigma_e$) then ionic transference number can also be expressed as

$$t_i = \frac{\sigma_{ions}}{\sigma_{total}} = \frac{i_{ions}}{i_{total}} \dots\dots\dots\dots\dots (13)$$

In case of superionic solids, it is essential to know separately the cationic contribution (t_{cation}) and anionic contribution (t_{anion}) to total transference number t_{ion} as well.Amongst the different techniques of ionic transference number (t_{ion}) measurement applicable to polymer nanocomposite electrolyte, *dc* polarization technique has been employed in present investigation. The dc polarization technique is also known as Wagner polarisation after the name of J.B. Wagner and C. Wagner [79]. This approach, as shown in figure-8(a), applies a dc voltage below the material's breakdown potential across the sample, which is sandwiched between two blocking electrodes. The time variation of the current through the sample is subsequently recorded. Upon activating the power supply, the total current flowing through the sample experiences a rapid initial reduction due to polarisation at the electrode electrolyte interface. Eventually, the current achieves a residual constant value, as shown in Figure 8(b). Both the ionic and electronic contributions to conductivity are responsible for the initial current.

($\sigma_t = \sigma_i + \sigma_e$) whereas constant current is only due to electronic contribution (σ_e). The t_{ion}can obviously be determined by equation (2.11).

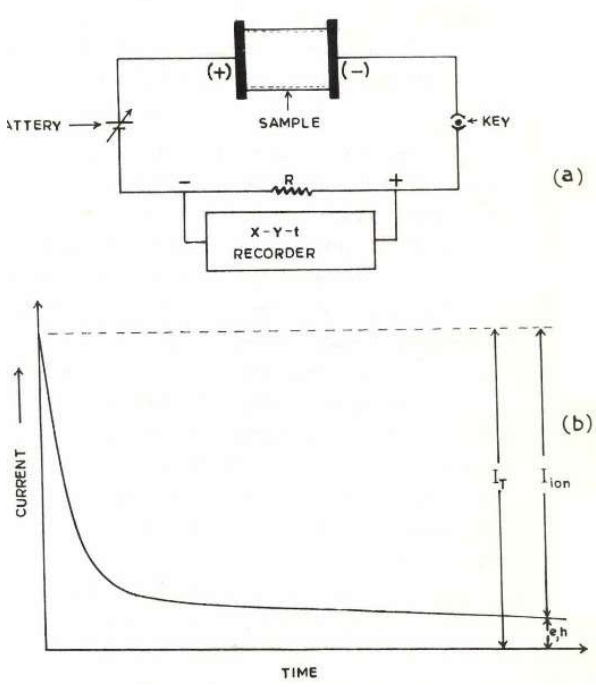

Figure -8 Schematic experimental arrangement for ionic transference number measurement using wager's DC Polarization Method (a)Blocking Electrodes (b)Typical Current vs Time Plot [80]

Though Wagner polarization method is simple to assess t_{ion} it is difficult to assess the type of charge carrier responsible for conduction i.e. anion or cation or both. Further, when electrode electrolyte interface resistance becomes comparable or more than bulk electrolyte, the residual electronic current may lead to incorrect determination of t_{ion}. Non-availability of perfect/non-blocking electrodes for proton conducting materials and inability to determine transference number of gaseous species further reduces the potential of this method. Nevertheless, a rough estimate of ionic nature of material can be made through this technique. The relationship between the initial current ($i_{initial}$) and final current (i_{final}) obtained from the I-t plots is used to compute the total ionic transference number (t_{ion}).

$$t_{ion} = \frac{i_{initial} - i_{final}}{i_{initial}} \quad \ldots\ldots\ldots\ldots\ldots (14)$$

3.5. Bulk Ionic Conductivity:

The most useful parameter associated with composite polymer gel electrolytes is its DC ionic conductivity and its variation as function of temperature and composition. This electrical parameter influences the power density of electrochemical devices and establishes the mass transport rate across the electrolyte. Therefore, conductivity of electrolyte is of prime concern itself and equal to inverse of resistivity. Section 2.3 lists some techniques of conductivity measurement of ionic conductors. Two terminal *dc* techniques are most simple but at the interface, partial blocking of ionic current leads to build up of space charge which poses problem in estimation of bulk conductivity [81,82]. Hence this charge builds up makes conductivity time dependent quantity which means σ corresponds to the value at which interval it is measured. Use of reversible electrode technique resolves the problem up to some extent by yielding consistent results but it creates error in assessing conductivity value of electrolyte precisely due to slow oxidation reduction process at the interfaces. In addition, it is often difficult to obtain good reversible electrodes possessing wide temperature window. Further, four probe cell is difficult to construct. Two terminal ac signal method with only one stimulus signal frequency is yet another easy way of determining conductivities of samples and generally it provides sufficiently accurate conductivity values. A four-probe ac configuration with independent current and voltage leads can be utilised when there is a significant charge transfer impedance. However, this approach is insufficient to accurately and completely characterise nanocomposite polymer electrolytes. The ultimate impedance of a cell is influenced by multiple factors. Because of their widely differing relaxation times, the contributions from the Charge transfer across the interface, the resulting double layer capacitance, the electrode-electrolyte interface impedance, and the movement of ions through the bulk of the electrolyte are all summed in a single frequency and respond quite differently in different frequency ranges. Heterogeneous distribution of phases in polymer electrolyte result in varying concentration gradient and grain boundaries which further complicates the situation. A common behavior of solid electrolyte conductivity (in logσ) with frequency (log f) is shown in figure-9.

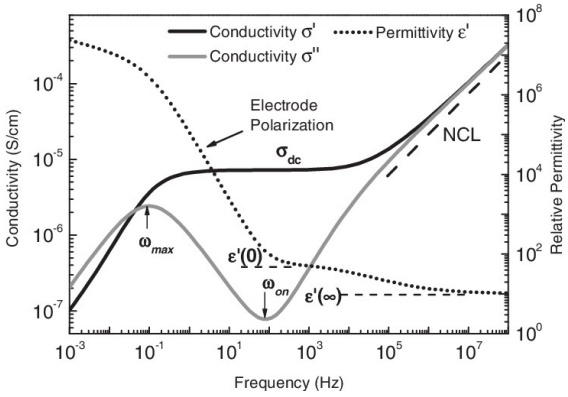

Figure -9 Variation in Conductivity with Frequency of Applied Field [83]

At very low frequencies, the electrode effects are pre-dominant. At intermediate frequency, the value corresponding to the plateau is usually taken as true *dc* conductivity. Therefore, measurement of frequency dependent conductivity or impedance is necessary to realize individual contribution.

Impedance spectroscopic technique—an ac technique with a wide range of frequency of measurement—was developed because of the systematic study of the ac response of an electrolyte or an electrochemical cell made feasible by technological and electrochemical advancements throughout time [84–85].

3.6. Impedance Spectroscopy:

Impedance spectroscopy gives range of information on electrical and other physio-chemical properties of the material and interface with their inter-relationship. Baureale [86] was the first to apply this technique for study of zirconia based solid electrolytes. In this technique, impedance is measured over a suitable frequency range. The collected data can be utilised to study the dynamics of bound and mobile charges in the bulk and interfacial area. Measurements of complex entities such as Complex impedance (Z*), complex permittivity (ε*), complex modulus (M*), and complex admittance (Y*) are all included in the scope of impedance spectroscopy. A basic formalisation of these factors and their relationships is provided in Table 2.2. Amongst these, the most common complex quantity- impedance Z* can be written as

$$Z^*(\omega) = Z'(\omega) - jZ''(\omega) \ldots\ldots\ldots (15)$$

where Z' and Z" are the real and imaginary part of impedance for simple equivalent parallel RC combination

$$Z^* = R(s) - j\omega CS \ldots\ldots\ldots (16)$$

Instead of plotting impedance Z* versus frequency, real and imaginary parts of impedance are commonly plotted as parametric function of frequency. This plot describes circular areas, which are characteristic of cell under investigation. Each of the physical process taking places in an electrochemical cell would give separate semi-circle provided their relaxation times are widely different. Theoretically, five semicircular arcs have been proposed but experimentally only three semi-circles are commonly observed [87] (figure-10).

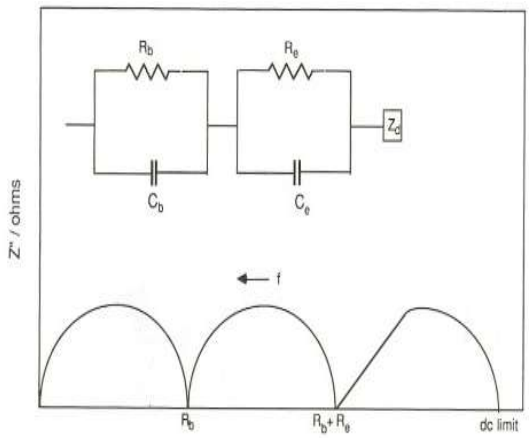

Figure -10 A typical complex plane lot and idealized circuit for a polymer electrolyte cell (non-blocking electrode for cations). R_e electrode resistance; C_e electrode capacitance R_b electrolyte resistance; C_b bulk geometric capacitance; $Z_d$diffusion-controlled impedance

The complex impedance plots of few basic circuit elements and their elementary combinations are represented in figure-11 (a) and (b).

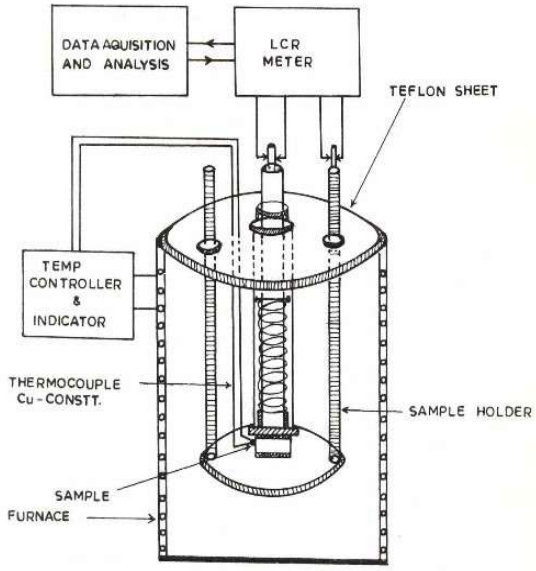

Figure -11(a) Experimental assembly used in impedance measurement for assessment of bulk ionic conductivity and dielectric parameters [88]

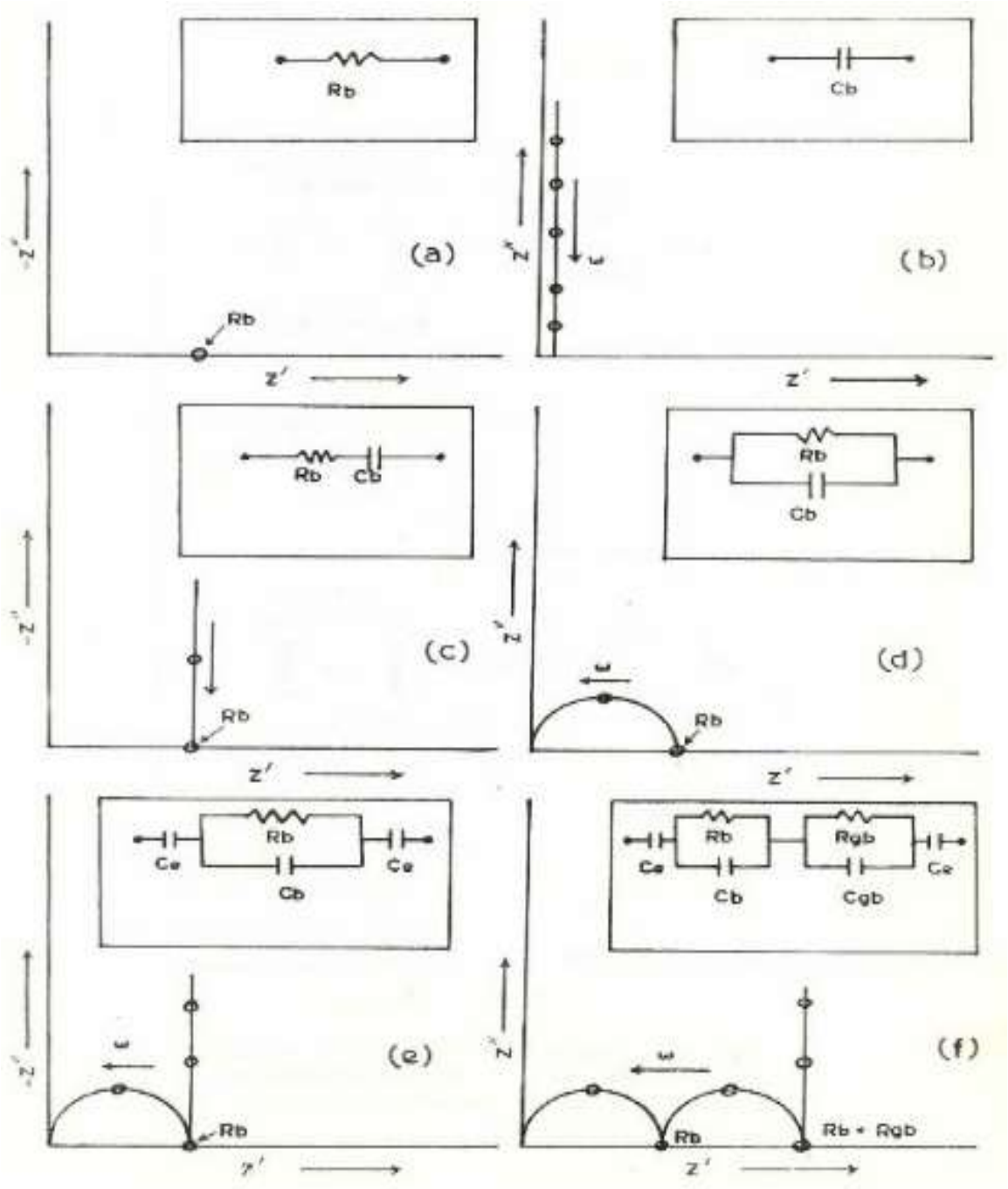

Figure 11(b). Complex impedance plots for some elementary circuit elements (a) R (b) C and (c-f) their combinations (circuits are shown in inset)

To the first approximation, each of the semicircles in the impedance diagram may be considered as the response of a lumped RC combination. From the correlation between the semicircle parameter and R and C components, the plotting of such diagrams provides straightforward determination of electrolyte resistance whatever may be the degree of electrolyte polarization. One of the biggest advantages of this method is that it does not require the use of reversible electrodes or complicated cell geometry. The equivalent circuit and impedance plot of an elementary cell with blocking as well as non-

blocking electrode is shown in figure-12. The intercept of first semicircle (high frequency) to real axis represents bulk resistance, R_b (figure-12 (a) and thus conductivity can be obviously evaluated by the relation

$$\sigma = \frac{l}{R_a A} \dots\dots\dots (17)$$

where, R_a is the bulk resistance of sample, *l*= thickness of the sample under study and A =the cross-section area of sample under study.

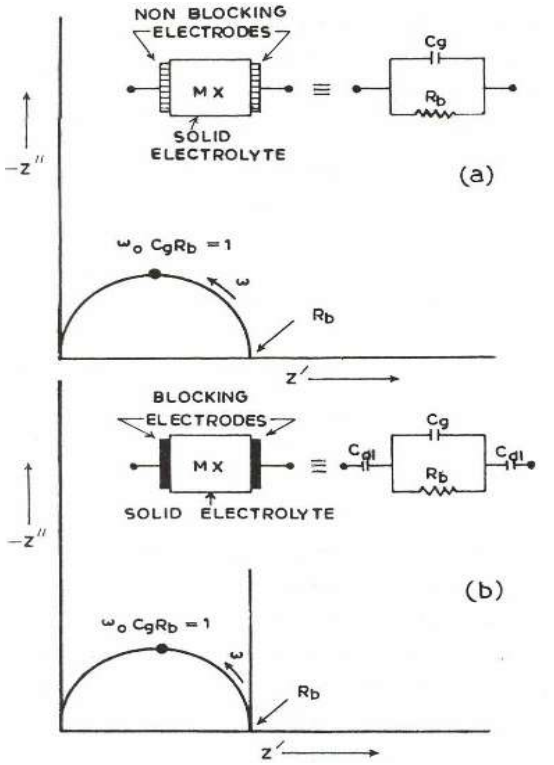

Figure 12. Complex impedance plots for typical electrochemical cells along with their equivalent circuits (a) with non-blocking electrodes and (b) with blocking electrodes

Sometimes it is challenging to resolve highly complex contributions of lines and semicircles in an impedance graphic. In such condition the admittance diagram is preferred because identification of deviation from straight line is easier than that from circular arc. In the present work, polymer composite polymer electrolytes have been sandwiched between two blocking platinum electrodes and kept in spring loaded holder as shown in figure-12 (b). The impedance measurements (Z,θ) have been performed on a Hioki make LCR meter (coupled to a computer) between a frequency range 40 Hz – 100 KHz.

Some Additional Features

Second Semicircle – Polymer electrolytes contain crystalline as well as amorphous regions along with uneven salt distribution throughout the matrix. Conductivity in such a system is a combination of inter grain and intra grain conduction. Because of the high defect density in the interface region, the grain boundaries may both provide high conductivity and impede ion movement. In such a case, a second semicircle is observed after the semicircle of ion conduction and polarization [89, 90]. The grain boundaries may be expressed as combinations of two parallel RC elements representing inter and intra granular regions (figure-13(b)).

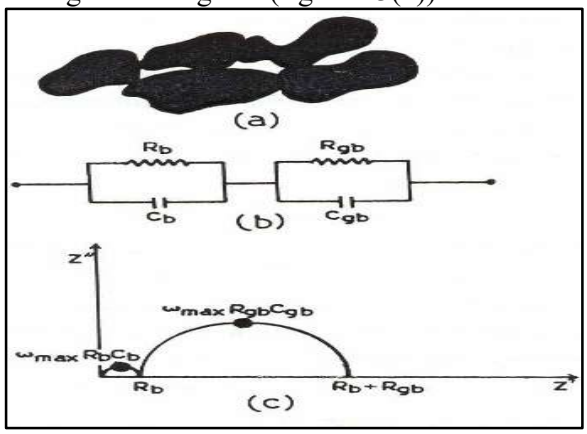

Figure – 13 (a) Approximate representation of in homogenous polymer electrolyte with individual grains in contact at grain boundary (b) equivalent circuit for (c) complex impedance plot for circuit

If conductivity increases at the grain boundary, it will give an apparent bulk resistance that is lower than real bulk effect.

Identification of Semicircle - The entire semicircles are rarely obtained within observation range. It may be then difficult to identify the semicircle arising from phenomenon. However, some tricks outlined below are used in proper identification

i. As a rule, the observation range shift from left to right of impedance diagram as the temperature increases. Bulk properties are

usually observed at low temperature and electrode characteristics appear at high temperatures.

ii. Since bulk resistance depends upon the length of sample and hence real intercept corresponds to bulk resistance in the impedance plot. Therefore, to separate bulk property, semicircle from electrode semicircle, measurements should be repeated for different length of sample.

iii. Replacement of electrode material can also be used to obtain electrode semicircle changes. Similarly, relaxation frequencies are dimension independent and thus measurement of relaxation frequency of concerned semicircle (i.e. top of semicircle) may also provide differentiation.

iv. Since bulk properties are found to be perfectly linear and relevant part of $Z^{'}$ $Z^{''}$ plot are independent of amplitude of applied signal whereas electrode response with amplitude variation is not linear especially for voltages greater than 100 mV. Therefore, variation in amplitude of applied signal may also be helpful in justification of processes.

v. Determination of capacitance and related dielectric constant may also provide identification criterion.

Overlapping of Semicircles – As discussed earlier, the plots of real and imaginary component will show one semicircle for each process taking place in the cell under study. If the relaxation time for each process differs by 100 times, separate semicircle would be observed. But in most cases considerable overlapping of semicircle may occur. To resolve this problem frequency distribution can be checked by Cole-Cole approach [91]. In this technique distances (u and v) are measured from origin and real axis intercept as shown in figure-14.

Logarithm of u/v is graphed as a function of frequency to decide the number of processes. Over the years, computers have been employed for analysis of overlapping semicircles.

Warburg Resistance – Nevertheless, difficulties occur when attempting to obtain the analogous circuit for the purpose of simulating the electrode phenomena in the cell.

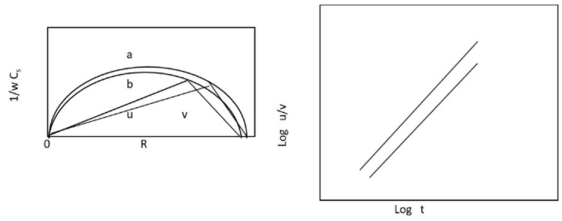

Figure-14 Cole- Cole method analyzing the overlapping semicircle [92]

The component that explains the impedance resulting from several electrode processes—namely, charge transfer, diffusion steps, and double layer capacitance (Cdl)—must be included. A transfer resistance Rt can be used to characterise the charge transfer resistance since the current is in phase with the applied voltage. It often corresponds with the electrode reaction rate. The concentration independent diffusion term is a function of frequency because at high frequencies the bulky ions move too slowly to react in phase with applied potential [93–94]. A straightforward formula for the interfacial impedance of the working electrode:

$$Z = \left[i\omega C_{dl} + \frac{1}{(Rt + W)} \right]^{-1} \dots\dots\dots\dots (18)$$

Where W, the Warburg impedance is given by

$$W = S\omega^{1/2} - js\omega^{1/2} \dots\dots\dots (19)$$

The Warburg coefficient S is a function of concentration and diffusion of oxidized and reduced species.

Constant Phase (angle) Element (CPE)-In many cases, especially in polymer composite gel electrolytes, depression of high frequency semicircle and bending of low frequency spike towards real axis are observed. The depression angle is usually small for bulk semicircle but can be very large for electrode semicircle. This feature cannot be manipulated with series and parallel combination of R & C component. A new type of circuit element is proposed and termed as constant phase angle element (CPE)

to account for displacement of centre of semicircle below real axis and spike tilting. The value of this impedance Z_{CPE} is given by

$$Z_{CPE} = k(j\omega)^{-p} \quad \text{where } 0 \leq p \leq 1 \quad \ldots\ldots\ldots (20)$$

When p = 0, Z = independent of frequency K = just a resistance R and p = 1, $Z = \frac{k}{j\omega} = \frac{-j}{\omega k^{-1}}$; the constant k^{-1} now corresponding to the capacitance C. The CPE functions as an intermediary between a resistor and a capacitor when p is between 0 and 1 (as is typically encountered). Thus, CPE connected in parallel with bulk resistance will result in depressed semicircle (figure-15).

Several interpretations have been proposed to explain this phenomenon. A general explanation can be offered in terms of inter and intra grain heterogeneity [88]. In case of polymer electrolytes, this may be due to distribution of crystalline non-conducting phase within conducting amorphous phase. Thus, heterogeneity in properties and their statistical distribution of corresponding relaxation may be the reason. Johnscher [96] have considered this semicircle depression as a specific property of ionic conductor and dielectric material. According to him, it is an essential attribute of the elementary jump of ion and due to local energy storage effect associated with slow relaxation of polarization, which is induced by mobile ions within its surroundings. Further, tilting of low frequency spike is related to the roughness of electrode-electrolyte interfaces. Series combination of CPE and bulk resistance represents this tilted low frequency spike. The bulk resistance is obtained from the intersection of flattened semicircle and tilted spike.

3.7. Dielectric Spectroscopy:

Dielectric spectroscopy establishes a connection between the features of the bulk properties of the material under study and the attributes of each individual constituent. The trend of frequency dependent dielectric studies, started during the days of Cole and Cole [97], have been spread over a wide variety of solid-state material characterization,

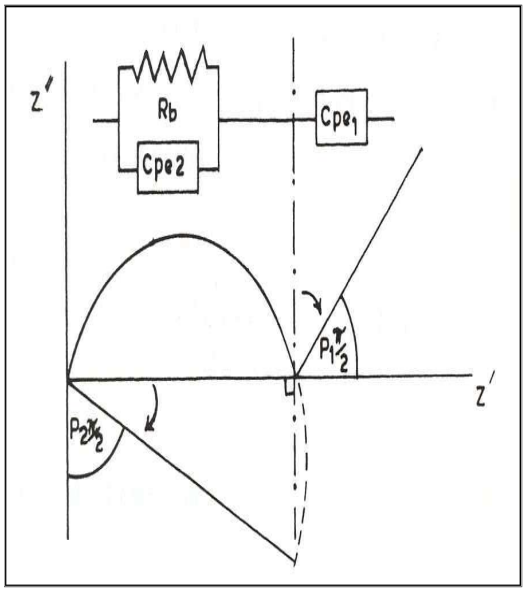

Figure-15 Constant phase element response of a typical polymer electrolyte cell illustrating depression of semicircle and tilting of spike. [95]

including, ion conducting materials. Several dipolar relaxations may be of interest in polymer-based electrolytes such as dipolar, segmental, and larger unit relaxation in the polymer itself and relaxation due to complexation with salt/acid (i.e. dipoles formed on complexation cation-anion pairs), relaxation due to clusters etc. The kind and type of ionic and molecular motions and their interactions, which are influenced by the chemical composition, molecular structure, and morphology of the sample under examination, are abundantly revealed by studying relaxation processes in such materials [98–99]. The relaxation frequency and the strength of relaxation are characteristic of the relaxing dipole. Therefore, the measurement of relaxation time can be used to differentiate conductivity relaxation processes from dipolar relaxation within the bulk materials. Despite being significant and helpful from a scientific perspective, dielectric investigations on ionically conducting solid nanocomposite polymer electrolyte have not been thoroughly investigated because of data analysis limitations and complexity. Fontenella et al. [100–101] have described the low frequency dielectric properties of a pure

polymer (PEO, PPO) and their complexes with different salts. The dielectric characteristics of ionically conducting solid polymeric films have also been reported recently [102-103] by Elisasson et al. [104]. While many research groups have done a good deal of work on the synthesis and characterisation of NCPEs [105, 106], relatively few studies have been published on the dielectric attributes of NCPEs to far. Impedance spectroscopy was used to analyse the electrical properties of NCPE films when a 200 mV small alternating current was applied across a symmetrical cell of the type Pt // NCPE // Pt (where Pt is for platinum blocking electrodes). A computer-controlled impedance analyzer (HIOKI LCR Hi-Tester, model: 3520, Japan) was used to get complex impedance parameters, or impedance, permittivity, and tangent loss parameters, as a function of frequency (40Hz to 100 KHz) at different temperatures (RT to 100°C). Relation 15 was utilised to compute the real and imaginary parts of impedance and permittivity.

$$\varepsilon * = \varepsilon' - j\varepsilon'' \ldots\ldots\ldots\ldots\ldots\ldots (21)$$

$$\varepsilon' = \frac{-Z''}{\omega C_o\left(Z'^2 + Z''^2\right)} \ldots\ldots\ldots\ldots\ldots (22)$$

$$\varepsilon'' = \frac{Z'}{\omega C_o\left(Z'^2 + Z''^2\right)} \ldots\ldots\ldots\ldots\ldots (23)$$

Where

ω= the angular frequency, C_o= the geometrical capacitance in vacuum of the same dimension as the

Sample [Co $= \frac{0.0885A}{d} PF$], A= the area of electrode and d = the thickness of the sample. The a. c. conductivity was evaluated from dielectric data in accordance with the relation

$$\sigma_{ac} = \omega \varepsilon_o \varepsilon_r \tan\delta \ldots\ldots\ldots\ldots\ldots\ldots (24)$$

Where $\varepsilon_r = \frac{C}{C_o}$ is the relative permittivity ω= 2πf, f= the frequency of the applied field, Following relation can be used to evaluate the tangent loss:

$$\tau \alpha \vartheta \delta \frac{\varepsilon''}{\varepsilon'} = \frac{Z''}{Z'} \ldots\ldots\ldots\ldots\ldots (25)$$

For different nanocomposite polymer electrolytes, the change of σ_{ac} with frequency displays dispersion at higher frequencies and a frequency independent tiny plateau in the low frequency zone. The universal power law governs this behaviour .

$$\sigma_{\alpha\gamma}(\omega) = \sigma_o + A\omega^{\vartheta} \ldots\ldots\ldots\ldots\ldots (26)$$

Where,

σ_o = d.c. conductivity (frequency independent plateau in the low frequency region)

A= the pre-exponential factor and,

n = the fractional exponent between 0 and 1.

The electrode polarisation effect is the cause of the conductivity spectrum's divergence from the plateau region (σ_{dc}) value in the low frequency zone. Through fitting of the observed to relation 26, the values of σ_o, A, and n were determined. Power law exponents (n) for ionic conductors typically vary from 1 to 0.5, denoting diffusion-limited hopping (tortuous paths) and optimal long-range pathways, respectively [107]. The universal dynamic response [108], which has been extensively noted in disorganised materials including Doped crystalline solids, ionically conducting glasses [109], and conducting polymers [110], as well as in general, follows the general behaviour of AC. It is generally accepted that this behaviour is demonstrated in the mechanism of charge transport nature of charge carriers.

In ac conductivity, it is observed that the frequency dependence of conductivity can be split into three zones:

(i) a plateau area of low frequency; (ii) an area of intermediate frequency dispersion. (iii) high frequency area that is not reliant on frequency Because of electrode polarisation effects at the interfaces between the electrode and the electrolyte, conductivity is nearly frequency independent in the low frequency range [111]. High frequency dispersion is indicated by the conductivity in the intermediate frequency band, which varies greatly with frequency. The conductivity increases with frequency in this zone, which is closer to relaxation times, due to the high mobility of charge carriers; in contrast, the

conductivity once more becomes frequency independent in the third high frequency region. The fact that the charge carriers are not sufficiently free to follow the fluctuating electric field in this location demonstrates that conductivity is practically frequency independent despite the high frequency.The Cole–Cole expression, or real part (ε') against imaginary part (ε") of complex permittivity, can be used to characterise the dielectric behaviour of polymeric materials [112]. The centre of the semicircular arc formed by the data points lies beneath the abscissa, fitting the data points nicely. The equation provides an empirical description of the complex permittivity (ε*).

$$\varepsilon^* = \varepsilon' - \varphi\varepsilon'' = \varepsilon_\infty + \frac{\Delta\varepsilon}{1+(\omega\tau)^\beta} \dots\dots\dots\dots\dots (27)$$

Where, $\Delta\varepsilon=\varepsilon_o-\varepsilon_\infty$,

ε_o is the static permittivity, ε_∞ the permittivity at very high frequencies, τ the angular frequency, τ the mean relaxation time and β the parameter using in the range $0<\beta<1$ to describe the distribution of relaxation time. When β=1, the equation gives semicircle in the plot of ε" vs.ε and is reduced to the non-co-operative single relaxation following the linear Arrhenius relation of the dielectric absorption maximum, f_{max} is expressed as

$$2\pi f_{max}\tau = 1 \dots\dots\dots\dots (28)$$

$$\tau = \frac{1}{2\pi f_{max}} \dots\dots\dots\dots\dots (29)$$

where the symmetry of the absorption and dispersion curves is centred at ^{74}=1. Therefore, fmax can be ascertained using the relaxation time τ that was measured experimentally [108].

3.8. Modulus Spectroscopy:

Many times, the complex modulus M* formalism is employed for dielectric relaxation research. From the impedance data presented by the relation, the real part M′ and the imaginary part MǴ of the complex modulus (M*) can be evaluated.

$$M^* = M' + jM'' = \frac{1}{\varepsilon^*} = j\omega\varepsilon_o Z'' \dots\dots\dots (30)$$

$$where,\quad M' = \frac{\varepsilon'}{\left(\varepsilon'^2+\varepsilon''^2\right)} \dots\dots\dots\dots (31)$$

$$M'' = \frac{\varepsilon''}{\left(\varepsilon'^2+\varepsilon''^2\right)} \dots\dots\dots\dots (32)$$

One benefit of presenting frequency-dependent dielectric or conductivity data using modulus formalism is that it removes any false effects caused by contacts or surfaces [113, 114]. This type of analysis of the electric data suggests that the electrode polarisation phenomenon adds very little to M* and can be ignored because the real part of the modulus M′ approaches zero at low frequencies. The values of the relaxation time and frequency correlate with the peak in the MǴ fluctuation.
When discussing the synthesis and characterization techniques of nanocomposite polymer electrolyte membranes, several key factors become crucial: scalability, economic feasibility, and repeatability of results. Let us break down each of these aspects in the context of these membranes:

- **Scalability**:

This refers to the ability of the synthesis method to be scaled up from laboratory-scale production to industrial-scale production without significant loss of efficiency or quality. For nanocomposite polymer electrolyte membranes, scalability is essential because these membranes are often intended for practical applications in devices like batteries, fuel cells, and sensors. Techniques that can be easily scaled up, such as solution casting, solvent evaporation, or electrospinning, are typically favored in industrial applications. It is important to ensure that as the production scales, the properties of the membranes remain consistent and desirable.

- **Economic Feasibility:**

The cost-effectiveness of the synthesis and characterization techniques is critical for widespread adoption and commercialization.

Factors influencing economic feasibility include the cost of raw materials, energy consumption during synthesis, labor costs, and equipment costs. Techniques that use readily available, inexpensive materials and involve straightforward processes tend to be more economically feasible. However, cost-effectiveness should be balanced with the performance and longevity of the membranes to ensure competitiveness in the market.

- **Repeatability of Results**:

Consistency in the properties and performance of nanocomposite polymer electrolyte membranes is essential for their reliability and reproducibility. Techniques that yield consistent results across different batches and under varying conditions are preferred. This requires robust characterization techniques that can accurately measure and validate the properties of the membranes, such as mechanical strength, ionic conductivity, thermal stability, and chemical resistance. Quality control measures and standardized protocols play a crucial role in ensuring repeatability.

4. **Potential Areas for Future Research:**
   - **Enhanced Performance through Nanoparticle Design**:

Investigating novel nanoparticle designs (e.g., core-shell structures, functionalized surfaces) can improve compatibility with polymer matrices, leading to enhanced mechanical, thermal, and electrochemical properties of membranes.

- **Advanced Characterization Techniques:**

Developing and refining characterization techniques (e.g., in situ imaging, multi-scale modeling) to provide deeper insights into the structure-property relationships of nanocomposite membranes. This can aid in understanding transport mechanisms and optimizing membrane performance.

- **Green and Sustainable Synthesis Methods:**

Exploring environmentally friendly synthesis routes (e.g., green solvents, sustainable nanomaterials) that reduce energy consumption, waste generation, and reliance on hazardous chemicals.

- **Integration with Emerging Technologies:**

Exploring the integration of nanocomposite polymer electrolyte membranes with emerging technologies such as artificial intelligence (AI) for predictive modeling, Internet of Things (IoT) for real-time monitoring, or additive manufacturing (3D printing) for customized membrane fabrication.

- **Application-specific Optimization**:

Tailoring synthesis and characterization techniques to meet the specific requirements of diverse applications (e.g., energy storage, water purification, biomedical devices) to enhance performance under varying conditions.

- **Long-term Stability and Durability:**

Investigating strategies to improve the long-term stability and durability of nanocomposite membranes, including resistance to degradation from chemical exposure, mechanical stress, and aging.

5. Conclusions: Experimental investigations using dielectric spectroscopy, electrical conductivity, XRD, OM, SEM, and IR reveal that nanofiller alters the morphological and physical attributes of the nano-composite electrolyte. The production of a nano-composite system with crystallite sizes ranging from 40 to 60 nm is confirmed by XRD and SEM measurements. When ferrite is dispersed, the electrical conductivity is increased by around 4 orders of magnitude, and it also regulates the gap between crystalline and amorphous conductivity. The amount of salt in the polymer electrolyte affects how well filler fits in. A broad electrochemical window for device applications is demonstrated by the C-V studies. The presence of the material electrode interface polarisation process is

shown by the fluctuation of the relative dielectric constant with frequency (on the lower frequency side) in nano composite electrolytes (NCPEs). It also suggests a strong coupling between segmental mobility of polymers and ions. The dielectric constant's frequency variation is more pronouncedly influenced by the addition of salt than by ferrite. The electrical modulus's scaling behaviour suggests that carrier concentration is also a factor in the relaxing process. As the concentration of salt rises, so does the ac conductivity.

References:

[1]. B. Scrosati., Applications of Electroactive Polymers, Chapman and Hall,London,1993.

[2]. F.M. Gray, Solid Polymer Electrolytes, Fundamentals and Technological Applications, VCH, New York, (1991).

[3]. D. E. Fenton, J.M. Parker, P.V. Wright, Polymer 14 ,1973, 589.

[4]. R. G. Linford, (Ed). Electrochemical Science and Technology of Polymers, 1 and 2, Elsevier Applied Science, London ,1987 and1990.

[5]. N.Srivastava, A. Chandra S.Chandra, Physica. Review, B52 ,1995, 225.

[6]. F. W. Stone, J. J Stratta., "Ethylene Oxide Polymers" In Encyclopedia of Polymer Science and Technology, Vol. 6, John Wiley &Sons, Inc New York, 1967, 103.

[7]. L. Yang, G. Venkatesh, R. Fassihi, "Characterization of compressibility and Compactibility of Poly (ethylene oxide) Polymers for Modified Release application by Compaction Simulator," J. Pharm. Sci. 85, 1996,1085.

[8]. P.G., Bruce, F. Grey, D. F Shriver, in Solid State Electrochemistry, Bruce. G. Ed. Cambridge University Press: Cambridge, U. K. ,1995.

[9]. W. Wieczorek, D. Raducha, A. Zaiewska, J. R. Stevens, J. Phys. Chem. 1998.

[10]. D. B. Braun., "Poly (ethylene oxide)" in Handbook of Water-Soluble Gums Resins, R. L. Davidson, Ed. (McGraw – Hill Book Company, New York, 1980 19

[11]. N. B. Graham, "Hydrogels for Useful Therapy," special publication, Royal Society of Chemistry, 87(High Value Polymers), 1991, 79.

[12]. N.B. Graham et al., "Caffeine Release from Fully Swollen Poly (ethyleneoxide) Hydrogels," J. Controlled Release 5, 1988, 243.

[13]. M.F. Daniel, B. Desbat, J.C. Lassegues, Solid State Ionics28, 1988 632.

[14]. A. Awadhia, S. L.Agrawal Solid State Ionics, 178, 2007, 951.

[15]. B. Brunetand, J. Cabane. Non-Cryst. Solids163, 1993, 211.

[16]. N. Chand, N. Rai, T. S. N. Natarajan S.L. Agrawal Fibres and Polymers, 12 2011, 438.

[17]. B.K. Choi, K.H. Shin, Solid State Ionics, 86, 1996, 303.

[18]. W. Wieczorek, J.R. Stevens, Z. Florzanczyc, Solid State Ionics, 85, 1996, 67.

[19]. D. Golodnisky, G.Ardel, E.Peled, Solid State Ionics, 85, 1996, 231.

[20]. Bhide, K. Hariharan, Polymer International, 57, 2008, 523.

[21]. S. S. Sekhon, G.S. Sandha, S.Chandra, Bull. Electrochem. 12, 1996, 415.

[22]. A. Chandra, P.K.Singh, S.Chandra, Solid State Ionics 15, 2002, 154.

[23]. D.K. Pradhan, R. N.P. Choudhary, B.K. Samantaray Express Polymer Letters 2,2008, 630.

[24]. F. Croce, L.Persi, F.Ronci, B.Scrosati, Solid State Ionics, 135, 2000, 47.

[25]. S. Chung, Y.Wang, L.Persi, F.Croce, S. G. Greenbaum, B. Scrosati, E. Plichta, J. Power Sources 97, 2001, 644.

[26]. M. Abdullah, W. Lenggoro, K. Okuyama, Encyclopedia of nanoscience and nanotechnology Edt. H.S. Nalwa, 8, 2004, 731.

[27]. M. Popovici, C. Savii, D. Niznanskya, J. Subrta, J. Bohaceka, D. Becherescub, C. Caizerc, C. Enache, C. Ionescu Journal of Optoelectronics and Advanced Materials, 5, 2003, 251.

[28]. K. Pandey, M.M. Dwivedi, M. Singh, S. L Agrawal., J. Polym. Res.17, 2010, 127.
[29]. B. Jirgensons, M.E. Straumanis, A Short Text Book of Colloid Chemistry, Pergamon Press, Oxford 1962,377.
[30]. S. Chandra, S. S. Sekhon, R. Shrivastava, N. Arora, Solid State Ionics,154, 2002, 609.
[31]. Tager, Physical Chemistry of Polymer, MIR Publisher, Moscow,1978.
[32]. M. S. Siekierski, Ph.D. Thesis, Warsaw Univ. of Tech., Warsaw, 1994.
[33]. S. Rabaste, Microcavitésoptiqueélaboréesparvoie sol-gel: applications aux ions terre rare d, Eu3+ et aux nanocristauxsemiconducteurs de CdSe, PhD thesis, Lyon, 1993.
[34]. B. Fabes et al 'Sol-Gel Derived Ceramic Coatings' in Ceramic Coatings and Films, ed. by J.B. Wachtman and R.A., Haber Noyes Publications, New Jersey, 1993.
[35]. M. Kakihana Journal of Sol-Gel Science and Technology, 6,1996, 7.
[36]. L.L. Hench, J. K. West, Chemical Review, 90, 1990, 33
[37]. Y. Narendar, G.L Messing, Catalysis Today, 35,1997, 247.
[38]. V. Driessche, B.Schoofs, G. Penneman, E. Bruneel, S.Hoste Measurent Science Rev., 5, 2005, 3.
[39]. C.J. Brinker, G.W. Scherer Sol-Gel Science, The Physics and Chemistry of Sol-Gel Processing, Academic Press, Boston, 1990.
[40]. B. Arkles, Kirk-Othmer Encyclopedia of Chemical Technology, John Wiley, New York,1997, 69.
[41]. A. C. Pierre, Introduction to sol-gel processing. Springer Nature, 2020
[42]. C. J. Brinker & G. W. Scherer, Sol-gel science: the physics and chemistry of sol-gel processing. Academic press. 2013
[43]. Y. Lu, H. Fan, N. Doke, D. A.Loy, , R. A. Assink, , D. A. LaVan, & C. J. Brinker, Evaporation-induced self-assembly of hybrid bridged silsesquioxane film and particulate mesophases with integral organic functionality. Journal of the American Chemical Society, 122(22), 2000 5258-5261.
[44]. K. Gopinath, S.Gnanasekar, , K. A. Al-Ghanim, M.Nicoletti, M.Govindarajan, A. Arumugam & S. Thanakkasaranee, Fabrication of neodymium (Nd), cadmium (Cd) and Nd: Cd doped hybrid copper oxide nanocomposites: evaluation of their antibacterial activity and cytotoxicity against human L132 cell line. Ceramics International, 49(18), 2023, 29933-29947.
[45]. M. S. Hassan, One pot synthesis of CoTiO3-TiO2 composite nanofibers and its application in dye degradation. International Journal of Chemoinformatics and Chemical Engineering (IJCCE), 8(2), 2019.47-56
[46]. Z.L. Lu, E. Lindner, H. A Mayer., Chem. Rev. 102, 2002, 3543.
[47]. A.C. Pierre, Introduction to Sol-Gel Processing. Kluwer, Boston, 1998.
[48]. B.D. Cullity, Elements of X-ray diffraction, Addison Wesley, Co.USA 1978.
[49]. J. Bonarski, "X-ray texture tomography of near-surface areas" Progr. Mat. Sc. 51, 2006, 61.
[50]. John Wiley & Sons Ltd. Elements of Modern X-Ray Physics, 2001, 40
[51]. B.E Warren, X-ray Diffraction, General Publishing Company, Classic X-Ray physics book ,1990.
[52]. Charles Hodgeman, Ed. CRC Handbook of Chemistry, and Physics, 44thEd. USA: Chemical Rubber Co. 1961.
[53]. W.L. Bragg, "The Diffraction of Short Electromagnetic Waves by a Crystal", Proceedings of the Cambridge Philosophical Society, 17, 1913, 43–57.
[54]. M. Taubin, V Platonov, A. Yaskolko X-Ray Tube Cathodes of Medical Purpose. Biomed Eng.;43(1) 2009, 48-50.
[55]. G. K. Williamson, W.H. Hall, X-ray line broadening from filed Aluminium and wolfram, Acta Metall. 1 ,1953, 22.
[56]. P. Habdas, E.R Weeks., Curr. Opinion in Coll. &Interf. Sci. 2002

[57]. D. Semwogerere, E.R. Weeks Confocal Microscopy, in Encyclopedia of Biomaterials & Biomedical Engineering, Taylor&Francis, 2005**.**

[58]. J.T. Rantala, P. Ayras, R. Levy, S. Honkanen, M.R. Descour N. Neogrammarian,"Binary phase zone-plate arrays based on hybrid sol-gel glass," Opt. Lett., 23, 1998, 1939.

[59]. Max. Knoll, "Aufladepotentiel and SekundäremissionElectronEnbestrahlter Korper", ZeitschriftfurtechnischePhysik, **16 ,1935,** 467.

[60]. J. Goldstein, Scanning electron microscopy and x-ray Microanalysis, Kluwer Academic/Plenum Publishers, 2003, 689.

[61]. L. Reimer, Scanning electron microscopy: physics of image formation and Microanalysis, Springer, 1998, 527.

[62]. R. F. Egerton, Physical principles of electron microscopy, an Introduction TEM, SEM, and AEM, Springer, 2005, 202.

[63]. R. Clarke, Microscopy techniques for materials science, CRC, 2002.

[64]. P. R. Griffiths and J.A. Haseth de, "Fourier Transform Infrared Spectroscopy," John Wildey& Sons, New York, 1986.

[65]. L. Smith, Applied Infrared Spectroscopy, New York: Wiley,1979.

[66]. R. M. Crooks et.al, "The Characterization of Organic Monolayers by FTIR External Reflectance Spectroscopy," Spectroscopy 7, 1993, 28.

[67]. C. Daniel Harris, and D. Bertolucci. Michael Symmetry and Spectroscopy: An Introduction to Vibrational and Electronic Spectroscopy. New York: Dover Publications, 1989. Print.

[68]. S. C. Lassegues, Desbat B., O. Tringquet, F. Cruege, Solid State Ionics, 35 ,1989, 17.

[69]. Sharma B. K., Instrumental Methods of Chemical Analysis, Goel Publishing House, Meerut (7^{th}edn), 1998.

[70]. K. Nakamoto, Infrared and Raman Spectra of Inorganic and Coordination Compounds(4^{th}edn), John Wiley & sons, New York, 1988.

[71]. M. I Pope, M.J. Judd, "Differential Thermal Analysis", London, Heyden, Academic Press 1977.

[72]. J. Sestak, V. Satava, W.W. Wendland Thermochimica Acta,7, 1973,333.

[73]. Konryushin & L.N. Larikov: J. Mat. Sci., 13, 1978,1.

[74]. L. Greer, ThermochimicaActa, 42,1980,193.

[75]. S. Etemad, A.J. Heeger, & A.G. Mac Diarmid, Annu. Rev. Phys. Chem.33, 1982,443.

[76]. P.K. Shukla, Study of Polymer Electrolytes for Electrochromic Display Devices, Ph. D. Thesis, A. P. S. University, Rewa, 1997.

[77]. P.T. Kissinger, W.R. Heineman, J. Chem. Educ.60, 1983, 702.

[78]. H. Karami, B. Kafi, S. N Mortazavi, Int. J. Electrochem. Sci.,4,2009,414.

[79]. W. W. Yao, H.M. Peng, R. D Webster, M. W Gill Peter, J. Phys.Chem. B, 112 2008, 6847.

[80]. J. S. Wagner, C. Wagner, J. Chem. Phys., 26, 1957, 1597.

[81]. A. R. Kulkarni, S. Selvasekarapandian, K. Hariharan, S. A. Suthanthiraraj, S. Selladurai, B. Nalini, Vijay Kumar, and M. (eds.) Proc. National Workshop on Solid State Ionics and Its Applications, Bharathiar University, Coimbatore 2002.

[82]. J. Przyluski, W. Wieczorek, Mat. Sci. and Engg. B13 ,1992,335.

[83]. A. A. Khamzin, I. I. Popov, And R. R. Nigmatullin, Correction of The Power Law of Ac Conductivity in Ion-Conducting Materials Due to The Electrode Polarization Effect Physical Review E 89, 2014, 032303

[84]. Rubintein (Ed.), Physical Electrochemistry: Principles, Methods and Applications, Marcell Dekker, New York ,1995.

[85]. D. W. Xia, J. Smid, Recent Advances in Fast Ion Conducting Materials and Devices, B. V. R. Chowdari, Q.Liu and

L. Chen (eds), World Scientific, Singapore,1990, 249.
[86]. J. E. Baurale, J. Phy. Chem. Solids, 30 1969, 2657.
[87]. S. Slane, M. Saloman, J. Power Sources, 55, 1995, 7.
[88]. B. E. Mallander, A. Luden, Materials for Solid State Batteries, (Eds.) B. V. R. Chowdari and S. Radhakrishna, World Scientific, Singapore, 1986, 161.
[89]. W. I. Archen R. D. Armstrong, in: Electrochemistry, vol. 7 (Ed.), H. R. Thirsk the Royal Soc. of Chem., London, 1980, 157.
[90]. K. S. Cole, R. H. Cole J. Phys., 9, 1941, 341.
[91]. S. P. S. Badwal, Solid State Batteries, B. V. R. Chowdari, S. Radhakrishna, World Scientific, Singapore, 1988, 965.
[92]. Wood J., Materials Today, 10, 2005, 16.
[93]. K. Johnscher, J. M. Reau, Mat. Sci. 13 1978, 563.
[94]. G. Williams, D. C. Watts and in Dielectric Properties of Polymer, (Ed.) F. E. Karazz, Plenum Press, New York 1972, 17.
[95]. S. L. Agrawal, P. K Shukla, Phy. Stat. Sol.163, 1997, 247.
[96]. P. Muistarelli, A. Magistris, P. Ferloni, Mol. Cryst. Liq. Crystal,229, 1993,187.
[97]. H. Shirkawa, E.J. Louis., A.G. Mac Diarmid , Chiang C.K. Heeger, A.J., J. Chem.Soc. Chem. Commun., 1977,578.
[98]. S. Etemad, A.J. Heeger, A.G., MacDiarmid, Annu. Rev. Phys. chem. 33,1982, 443
[99]. J. R. Macdonald (Ed.), Impedance Spectroscopy – Emphasizing Solid Materials and System, John Wiley & Sons, New York ,1987.
[100]. M.C. Wintersgill, Fontanalla, in Polymer Electrolyte Review-II, MacCallum J.R. and Vincent CA (eds.), Elsevier, London ,1987.
[101]. H. Eliasson, I. Albinsson B.E. Mellander, Electrochemica Acta 43 1998, 1498.
[102]. K.P. Singh, P. N. Gupta European Polymer Journal, 34, 1998, 1023.
[103]. B. Natesan, N.K. Karan et al J. Non Crystalline Solids352, 2006,5205.
[104]. D. K. Pradhan, R.P.N Choudhary, J. Power Sources139, 2005, 384.
[105]. T. J. Pinnavaia, G. W. Bell (eds.) Polymer-Clay Nanocomposite, JohnWiley and Sons Ltd. England 2000,1.
[106]. M.Wang, F Zhao, Z. Guo, and S. Dong, Electrochemica Acta, 49, 2004, 3595.
[107]. K. Jonscher, Dielectric relaxation in Solids, Chelsea Dielctric Press, London, 1983.
[108]. K. Jonscher, Nature, 267,1977, 673.
[109]. K. A. Mauritz Macromolecules, 22, 1989, 4483
[110]. S.R. Elliott Solid State Ionics, 27 ,1988, 131.
[111]. M.L. Lucia Leon, and J. Santamaria, Phys. Rev. B 55, 1997, 882
[112]. D.K. Pradhan, R.N.P Choudhary, B.K. Samantaray Int. J. Electrochem.Sci.3,2008, 597.
[113]. H. A. Hashen and S. Aboulhassan Chinese Journal of Physics 43, 2005, 955.

Polypyrrole-Magnetite-Nanocomposite Based Toroidal Transformers: An Economical Industrial Solution with Minimum Core Losses

Jyoti Shah*, R K Kotnala

CSIR-National Physical Laboratory, Dr K S Krishnan Marg, Delhi, India

Volume 1, Issue 4, July 2024
Received:20 June, 2024; Accepted: 12 July, 2024
DOI: https://doi.org/10.63015/5N-2433.1.4

**Corresponding Author Email: shah.jyoti1@gmail.com*

Abstract: Electricity transmission and power conversion devices are always associated with huge power losses and transformer is the primary element in electricity transmission system and power conversion devices. Moreover, it is the major constituent of the power losses because of retaining substantial core losses which are further disintegrated into hysteresis and eddy current losses. Consequently, there is an immediate need for innovating new materials for transformer core to minimize the losses. Besides low hysteresis losses, high power to weight ratio is also a key factor for fabricating efficient and light weight transformer core. In this direction, soft magnetic nanocomposites provide attainable solution by exhibiting low hysteresis losses. In present work it is first time reporting a light weight and highly efficient polypyrrole-magnetite nanocomposite based toroidal transformer core. Polypyrrole-magnetite based nanocomposites are synthesized by facile and cost-effective solution phase route and fabricated as toroidal cores to study the power losses at high frequencies for transformer applications. Vibrating sample magnetometer (VSM) study shows the decrement in hysteresis losses from 8576 erg/cm^3 for bare Fe_3O_4 NPs to 6467 erg/cm^3 for NC-90(90:10; Fe_3O_4:PPy).Core losses measurement of composites at open circuit (no-load test) reveals reduction in loss values from 43.20 mW/cm^{3}for bare Fe_3O_4 NPs to 30.72 mW/cm^3 for NC-90 and from 30.35 mW/cm^3 to 18.24 mW/cm^{3}at 5 V and 3.5 V excitation voltages, respectively. Moreover, similar trends are also observed in broad range of frequencies ranging from 50 Hz to 50 kHz. Minimum core loss30.72 mW/cm^{3}at 50 kHz has been reported by NC-90 nanocomposite. Low Core losses are the primary need of hour for miniaturization of future economical transformer devices.

Keywords: Nanomagnetic particles, Hysteresis, Nanocomposite, Polypyrrole, Transformer core.

1. Introduction: Power saving has become a primary challenge for today's world due to fast deprivation of natural resources and emerging of deleterious environmental problems [1,2]. Transformers have major role for retaining the power owing to its vast applications in power and electronics industries such as power distribution and transmission systems, power converters in switching mode power supplies and as wide band and pulse transformers [3-5]. Core geometry, core material and the windings are the critical elements of the transformers that specify its efficiency, weight and cost [6]. Being the key parameter, core material plays the central role in power conversion in the transformer devices at global level**.** Electrical steel (Fe-Si alloy) and soft ferrites such as Mn-Zn, Ni-Zn and Mg-Zn ferrites are the traditional base materials of transformer cores due to their high saturation magnetic induction and low power losses for low and high frequency applications, respectively [7,8]. Electrical steel has low corrosion resistance with high processing cost [9-11] and micro-magnetic soft ferrites have large volume of magnetic components and high hysteresis losses [12-15].

However, lack of significant and desirable power losses in case of these materials, limit their commercial viability and technological feasibility [1]. Consequently, there is continuous strong urge across the world for novel materials to achieve the adequate power losses. The strategic goal is to carry out the research for the development of light weight and easily processed soft magnetic nanocomposite materials for the fabrication of transformer core for advance technologies at minimal cost. Owing to their negligible coercivity, superparamagnetic nanoparticles of single domain are extremely advantageous for producing low hysteresis losses [16,17]. Soft ferrite nanoparticles dispersed in conducting polymer matrix offer high saturation magnetic induction, low power losses with tunable properties, ease of manufacturing and high corrosion resistance [18,19]. As per literature, bulk soft ferrites exhibit 288 mW/cm^3 power losses at high frequency of 50 kHz [20]. Recently, Zhou et al reported 450 mW/cm^3 power losses at 50 kHz frequency for composite core in which Fe-6.5wt% Si powder insulated with Mn-Zn ferrite nanoparticles [15]. Mori et al designed Ni-Zn-Fe ferrite coated with Fe-3.5 Si-4.5 Cr powder composite core showed 224 mW/cm^3 power losses at 50 kHz [21]. In present work toroidal cores have been fabricated using nanocomposite material, synthesized through a universally recognized simple solution method taking magnetite nanoparticles (Fe_3O_4 NPs) and polypyrrole as starting precursors. Transformer cores have been constructed into toroidal geometry to allow the maximum magnetic flux enclosure and to provide supports on its edges which subsequently minimizes core stress [6,22]**.** Being less toxic with good magnetic properties, facile synthesis and chemical stability of Fe_3O_4 NPs in conjunction with polypyrrole provided a unique platform of nanocomposites for the designing of highly efficient, light weight, cost effective core material with tunable functionalities and environmental benign synthesis protocols [23-28]. Synthesized nanocomposites exhibited good saturation magnetization with negligible coercivity. As a consequence, hysteresis losses were decreased due to reduction in surface anisotropy with the incorporation of polypyrrole as well as alternating current (AC) power losses were comparatively lower than pure Fe_3O_4 NPs at high frequencies [29]. Low power losses as well as high saturation magnetic induction properties were obtained in nanocomposite cores with light weight, ease of processing and low cost also. To the best of our knowledge, no work has been published on the synthesis of nanocomposite (Fe_3O_4 NPs and polypyrrole) involving DMSO as a solvent by solution synthesis method. In fact, it is first report on the fabrication of transformer toroidal cores of magnetite–polypyrrole nanocomposite.

2. Experimental Details

2.1. Materials

Ferrous chloride tetrahydrate ($FeCl_3.4H_2O$), ferric chloride hexahydrate ($FeCl_3.6H_2O$) and ammonia solution (25 %) of Merck were used in the experiments. Pyrrole and methanol were of analytical grade. Distilled water (DI water) was used for the experiments.

2.2. Preparation of Fe_3O_4 NPs by co-precipitation method

Fe_3O_4 NPs were prepared by co-precipitation method. Firstly, $FeCl_3.4H_2O$ and $FeCl_3.6H_2O$ with molar ratio (2:1) were dissolved in DI water. Ammonia solution (30 mL) was added drop wise under stirring into the reaction solution at maintained temperature of 70 °C and pH value of solution was adjusted at 12. Reaction solution was stirred for next 10 minutes. Prepared Fe_3O_4 NPs from reaction solution were washed with DI water and dried in vacuum oven at 60 °C for 8 hours.

2.3. Polymerization of Pyrrole by chemical oxidative polymerization method

Chemical oxidative polymerization method was adopted for polymerization of pyrrole. Pyrrole was distilled under reduced pressure and stored in dark at 5 °C. $FeCl_3.6H_2O$ oxidant (0.016 molar) was dissolved in DI water and oxidant solution was degassed before use. Distilled pyrrole (0.50 mL) was added into oxidant solution under vigorous stirring in argon atmosphere and was continued for next 8 hours. Prepared PPy was washed with methanol and dried in vacuum oven at 50 °C for 24 hours.

2.4. Formation of nanocomposites

Solution method was used for the formation of nanocomposites. As-prepared Fe_3O_4 NPs and PPy were dispersed in di-methyl sulfoxide (DMSO) solvent separately with the aid of probe sonicator for 45 minutes and 15 minutes, respectively. Fe_3O_4 NPs and PPy solutions were intermixed with the aid of probe sonicator for 20 minutes. Prepared nanocomposites solutions were mixed with water and then reaction mixture was separated from the DMSO and water solvent through magnetic decantation. Obtained reaction mixture was washed with DI water and dried in vacuum oven at 50 °C for 24 hours. As a result, five samples of nanocomposites were prepared with loading of Fe_3O_4 NPs in different concentration (8.6 g, 3.86 g, 2.24 g, 1.45 g and 0.967 g in DMSO solvent, respectively) in polypyrrole (0.967 g in DMSO solvent) matrix and samples were denoted NC-90 (90 % loading of Fe_3O_4 NPs in polypyrrole matrix), NC-80 (80% loading of Fe_3O_4 NPs in polypyrrole matrix), NC-70 (70% loading of Fe_3O_4 NPs in polypyrrole matrix), NC-60 (60% loading of Fe_3O_4 NPs in polypyrrole matrix) and NC-50 (50% loading of Fe_3O_4 NPs in polypyrrole matrix), respectively. Schematic representation of Fe_3O_4 NPs, PPy and nanocomposites synthesis are shown in Figure 1.

2.5. Characterization Techniques

X-ray diffraction analysis of the samples was examined on Rigaku make X-ray diffractometer with CuK_α (λ=1.54 Å) radiation source. CuK_α radiation was produced at room temperature with power setting of 40 kV and 30 mA. Infrared spectra of the prepared samples using the KBr pellet were recorded on Fourier Transform Infrared spectrometer (IR infinity-I Shimadzu). Particle size and morphology of the Fe_3O_4 NPs and nanocomposite samples were determined from high resolution transmission electron microscopy (HRTEM, Technai G20-stwin) at an accelerating voltage of 200 kV. Point and line resolution of HRTEM were 1.44 and 2.32 Å, respectively. A small drop of diluted Fe_3O_4 NPs and nanocomposite samples (NC-50 and NC-90) in ethanol were dripped on TEM grids for performing the TEM analysis. Magnetic measurements of nanocomposite samples were performed at room temperature using vibrating sample magnetometer (VSM, Lakeshore 7404**)** at an applied maximum external magnetic field of 5 kOe. The electrical conductivity of polypyrrole and nanocomposite samples was measured using four-point probe method. Conductivity measurement was performed on circular pellets of samples having diameter of 10 mm and thickness of 1 mm, prepared by hydraulic press. An open circuit test (no-load test) was executed using power meter on nanocomposite based toroidal cores. Nanocomposite samples were compacted into toroidal shaped specimens using hydraulic press having following dimensions (outer diameter = 14 mm, inner diameter = 7 mm and height = 4 mm) with the aid of polyvinyl alcohol (PVA).

3. Results and Discussion:

Crystallographic structures of prepared samples are presented in Figure 2. Crystalline peaks of Fe_3O_4 NPs at 2θ = 30.1°, 35.6°, 43.1°, 53.6°, 57.1° and 62.9° indexed to the (220), (311), (400), (422), (511) and (440) lattice planes, respectively which confirm the pure crystalline phase formation of Fe_3O_4 NPs (JCPDS-790417). Using Scherrer's equation, the average particle size of Fe_3O_4 NPs is calculated

9.27 nm. Polypyrrole XRD pattern shows broad scattering peak at 25.8° diffraction angle determined its amorphous phase which is the characteristics of doped polypyrrole [30]. The peaks at 2θ = 30.1°, 35.6°, 43.1°, 53.6°, 57.1°, 62.9° and 25.8° reveal the presence of Fe_3O_4 NPs and polypyrrole in the nanocomposite samples [31]. Figure 3 depicts the FTIR spectra of polypyrrole, Fe_3O_4 NPs and nanocomposite samples. The absorption band at 576 cm^{-1} is attributed to Fe-O bond stretching in the Fe_3O_4 nanoparticles [32]. The characteristics peaks obtained at 3410 cm^{-1} and 1533 cm^{-1} are assigned to the N-H stretching and C-C stretching vibrations in the polypyrrole sample [33,34]. The absorption centered in the range (1250-1100) cm^{-1} is ascribed to the pyrrole ring vibration [26]. Peaks observed at 1294 cm^{-1} and 1031 cm^{-1} denote the C-H in plane and out of plane deformation mode. C=C stretching vibration in polypyrrole is occurred at 894 cm^{-1} [35]. The main absorption bands of polypyrrole and Fe_3O_4 NPs are appeared in the nanocomposite samples which confirm the existence of polypyrrole and Fe_3O_4 NPs. However, noticeable peak shifting is observed in the nanocomposite compared to bare magnetite nanoparticles and polypyrrole peaks. It may be attributed to non-covalent interactions such as columbic and Vanderwaal's interactions between the magnetite and polypyrrole [29,36,37]. Surface dangling bonds of magnetite interact with ring electron density of the polypyrrole. Moreover, such interactions induce a synergy effect in the final nanocomposite and resulted into the reduced resistivity and power losses. Such surface interactions promote the uniform dispersion of magnetic nanoparticles in polymer matrix observed in HRTEM images. HRTEM images of Fe_3O_4 NPs are shown in Figure 4 (a) and 4 (a′). Fe_3O_4 NPs are of spherical shape with average diameter of 9 nm similar to XRD crystallite size [31]. Figure 4 (b) and 4(b′) show the HRTEM micrographs of the NC-50 sample and Figure 4(c) and 4(c′) represent the HRTEM images of the NC-90 sample. A uniform dispersion of Fe_3O_4 NPs is observed in polypyrrole matrix [38]. Magnetization and flux density curves at room temperature are plotted as a function of magnetic field to study the magnetic properties of the prepared samples shown in Figure5(a) and 5 (b). Images of the flux density curves at low magnetic field are also incorporated in Figure 5 (b). Magnetic properties of the Fe_3O_4 NPs and nanocomposite samples are listed in Table 1. Magnetic properties such as saturation magnetization (M_s), coercivity (H_c), hysteresis area and magnetocrystalline anisotropy constant (K) of the nanocomposite samples were reduced because of the inclusion of non-magnetic polypyrrole polymer content. Magnetic properties of the magnetic nanoparticles are greatly affected by the surface chemistry [39]**.** Reduced magnetization in superparamagnetic nanoparticles is described based on the presence of disordered spins at the surface and by the spin canting [40]. Additionally, saturation magnetization is reduced in the nanocomposite samples with the incorporation of polypyrrole molecules due to predominant diamagnetic nature of polypyrrole[41].Furthermore, magnetic properties of magnetic NPs also depend on many anisotropy aspects. Dispersion of Fe_3O_4 NPs in polypyrrole matrix may influence surface anisotropy and interface anisotropy due to interfacial electrostatic and Vander-waals interactions [29]. The decrement in coercivity of the nanocomposite may be due to reduced surface anisotropy of Fe_3O_4 NPs by interfacial bonding of PPy ring electrons with its surface spins (dangling bonds). Using stoner-wohlfarth theory, the H_c of nanoparticles is calculated by the equation (1):

$$H_c = \frac{2K}{\mu_o M_s} \quad \text{..... (1)}$$

Herein, K is magneto crystalline anisotropy, μ_o is the permeability in free space and its value is $4\pi \times 10^{-7}$ H/m and M_s is the saturation magnetization. The value of K is determined by the product of H_c and M_s. It can be inferred that

K value is monotonically decreasing function with loading of polypyrrole resulting into reduction of H_c and M_s. Thus, coercivity value varies with change in surface anisotropy. Consequently, hysteresis losses reduced. Figure 6 represents the conductivity values of the nanocomposite samples and polypyrrole. Conductivity decreases with increasing concentration of Fe_3O_4 NPs in the nanocomposite samples. Conduction mechanism in the conducting polymer arises due to transport mechanism of anions, bipolarons and hopping of electrons in its conjugated system. Charge carrier scattering and blockage of conduction path, both are enhanced with the inclusion of the Fe_3O_4 NPs in the polypyrrole matrix as well as free surface charge is decreased due to physical interaction between polypyrrole and Fe_3O_4 magnetic NPs. Consequently, conductivity is reduced [42-45]. Figures 7 and 8 demonstrate the power losses density curves of the samples as a function of frequency from 50 Hz to 50 kHz at two sinusoidal exciting voltages 5 V and 3.5 V, respectively. Power losses are segregated into three components: hysteresis losses (P_h), eddy current losses (P_e) and residual losses (P_r). Residual losses predominate only at very high frequencies and at low magnetic flux density levels [46]. It is approximated to zero in the power applications of the soft magnetic materials [47,48]. Hysteresis losses are appeared due to high coercivity of the magnetic materials and surface anisotropy determines the coercivity factor as above discussed [22,39,49]. With the incorporation of polymer content in the Fe_3O_4 magnetic NPs, coercivity was reduced and hysteresis losses were decreased. It can be validated by the calculated values of the coercivity and hysteresis area as displayed in Table 1. On the other side, eddy current losses are increased due to decrement in resistivity with the addition of polymer content [22]. Resistivity of the nanocomposite samples is decreased with the inclusion of higher concentration of polypyrrole and it is shown in Figure 6. Eddy current losses are comparable to the hysteresis losses at normal line frequency (50 Hz/60 Hz) [22]. P_e is directly proportional to the square of frequency while P_h is directly proportional to the frequency. Accordingly, eddy current losses are abruptly enhanced than hysteresis losses with the increased excitation frequency [50]. Consequently, power losses are almost constant till 1 kHz frequency and increased beyond 1 kHz frequency as shown in Figures 7 and 8. Power loss density values at 50 Hz frequency were decreased from 37.80 mW/cm^3 for Fe_3O_4 magnetic NPs to 24.58 mW/cm^3 for NC-90 sample at 5 V and also reduced from21.41 $mW/cm^3$to 14.71 mW/cm^3 at 3.5 V. Power loss density values at 50 kHz decreased from 43.20 mW/cm^3 (Fe_3O_4 magnetic NPs) to 30.72 mW/cm^3 (NC-90 sample) at 5 V and it is reduced from 30.35 mW/cm^3 to 18.34 mW/cm^3 at 3.5 V excitation voltages. Power loss density values were further increased from 24.58 mW/cm^3 and 14.71 mW/cm^3 (NC-90) to 34.45 mW/cm^3 and 18.99 mW/cm^3 (NC-50 sample) at 5 V and 3.5V excitation voltages, respectively at 50 Hz frequency. Power losses density values were also further increased from 30.72 mW/cm^3 and 18.34 mW/cm^3 (NC-90 sample) to 40.40 mW/cm^3 and 29.93 mW/cm^3 (NC-50 sample) at 5 V and 3.5V excitation voltages, respectively at 50 kHz frequency, but still less than the Fe_3O_4 magnetic NPs. It might be increased due to enhancement of eddy current losses with the decrement in resistivity. Resistivity is reduced with the loading of polypyrrole in nanocomposite due to induced synergy effect via non covalent interaction between ring electron density of the polypyrrole and surface dangling bonds of magnetite. Additionally, conduction takes place with the inclusion of conducting polypyrrole phase in nanocomposite. Consequently, eddy current gets conduction path easily and eddy current losses are enhanced rapidly.

4. Conclusions

This work reports an eloquent approach for reducing core losses at high frequencies by nanocomposite of Fe_3O_4 NPs and PPy. At high frequency of 50 kHz, power loss density values decreased from 43.20 mW/cm^3 (Fe_3O_4 magnetic NPs) to 30.72 mW/cm^3 (NC-90 sample) at 5 Vand it reduced from 30.35 mW/cm^3 to 18.34 mW/cm^{3}at 3.5 V excitation voltages. Reduction in core losses in nanocomposite is the result of decrease in coercivity of nanocomposite. Core losses monotonically increased with polypyrrole concentration. Therefore, the core losses were increased in NC-50 sample comparatively to NC-90 sample. Enhancement in eddy current losses may be the reason for increased core losses because the conductivity is increased with the addition of polypyrrole phase in nanocomposite. Trivial hysteresis losses obtained in nanocomposite due to reduced surface anisotropy by interfacial surface interaction of PPy and Fe_3O_4 NPs. Nanocomposite sample (NC-90) with less inclusion of PPy matrix exhibited minimum core loss at high frequency, which is most suited for switching mode power supplies.

References

[1] D. van Niekerk, B. Schoombie and P. Bokoro, Design of an Experimental Approach for Characterization and Performance Analysis of High-Frequency Transformer Core Materials, *Energies* **16(9)**, 2023, 3950.

[2] K. Zhu, H. Chen, S. Li, C. Sun, F. Liu, An RF On-Chip Transformer With Fe_3O_4/GO Nanocomposite Film, *IEEE Transactions on Magnetics,* **57**, 2, 2021.

[3] A. Najafi, and I. Iskender, Comparison of core loss and magnetic flux distribution in amorphous and silicon steel core transformers. *Electr. Eng.***100**, 2018, 1125–1131.

[4] R. Williams, D. A. Grant, and J. Gowar, Multielement transformers for switched-mode power supplies: toroidal designs. *IEE Proc. B Electr. Power Appl.***140**, 1993, 152.

[5] A. C. Razzitte, S. E. Jacobo, and W. G. Fano, Magnetic properties of MnZn ferrites prepared by soft chemical routes. *J. Appl. Phys.***87**, 2000, 6232–6234.

[6] L. M. Bollig, P. J. Hilpisch, G. S. Mowry, and B. B. Nelson-Cheeseman, 3D printed magnetic polymer composite transformers. *J. Magn. Magn. Mater.***442**, 2017, 97–101.

[7] Z. H.Khan, M. Rahman, S. S. Sikder, M. A. Hakim, and D. K. Saha, Complex permeability of Fe-deficient Ni–Cu–Zn ferrites. *J. Alloys Compd.* **548**, 2013, 208–215.

[8] Y. Lu, G. Zu, L. Liu, Y. Wang, L. Gao, L.Yuan, X. Ran, X. Zhang, Investigation of microstructure and properties of strip-cast 4.5 wt% Si non-oriented electrical steel by different rolling processes. *J. Magn. Magn. Mater.* **497**, 2020, 165975.

[9] J. E. Contreras, E. A. Rodriguez, and J. Taha-Tijerina, Nanotechnology applications for electrical transformers—A review. *Electr. Power Syst. Res.* **143**, 2017, 573–584.

[10] G. Ouyang, X. Chen, Y. Liang, C. Macziewski, and J. Cui, Review of Fe-6.5 wt%Si high silicon steel—A promising soft magnetic material for sub-kHz application. *J. Magn. Magn. Mater.***481**, 2019, 234–250.

[11] H. Wayne Beaty, Donald Fink. *Standard Handbook for Electrical Engineers (2012)*.

[12] K. Praveena, K. Sadhana, S. Bharadwaj, and S. R. Murthy, Development of nanocrystalline Mn–Zn ferrites for forward type DC–DC converter for switching mode power supplies. *Mater. Res. Innov.***14**, 2010 56–61.

[13] J. Gass, Functional Magnetic Nanoparticles. (University of South Florida, 2012).

[14] G. Khan, Design and synthesis of soft magnetic materials for high frequency power applications. (Dartmouth College, 2014).

[15] M. M. Zhou, *et al.* Magnetic properties and loss mechanism of Fe-6.5wt%Si powder core insulated with magnetic Mn-Zn ferrite nanoparticles. *J. Magn. Magn. Mater.***482**, 2019, 148–154.

[16] Z. Mosleh, P. Kameli, M. Ranjbar, and H. Salamati, Effect of annealing temperature on structural and magnetic properties of $BaFe_{12}O_{19}$ hexaferrite nanoparticles. *Ceram. Int.***40**, 2014, 7279–7284.

[17] M. Houshiar, F. Zebhi, Z. J. Razi, A. Alidoust, and Z. Askari, Synthesis of cobalt ferrite ($CoFe_2O_4$) nanoparticles using combustion, coprecipitation, and precipitation methods: A comparison study of size, structural, and magnetic properties. *J. Magn. Magn. Mater.***371**, 2014, 43–48.

[18] Yun, H. *et al.* Size and composition dependent radio frequency magnetic permeability of iron oxide nanocrystals. *ACS Nano* **2014**, 12323–12337.

[19] S. C. Mills, E. A. Patterson, J. S. Andrew, 0-3 magnetic nanocomposites via EPD: Current

status for power component fabrication and future directions, *Am Ceram Soc.* **107(3)**, 2024, 1859–1870.

[20] J. P. F. Araújo, High power density DC-DC converter. 2015.

[21] S. Mori, T. Mitsuoka, M. Sonehara, T. Sato, & N. Matsushita, High permeability and low loss of Ni-Zn-Fe ferrite/metal composite cores in high frequency region. *AIP Adv.***7**, 2017, 056657.

[22] H. W. Ng, R. Hasegawa, A. C. Lee, & L. A. Lowdermilk, Amorphous alloy core distribution transformers. *Proc. IEEE* **79**, 1991, 1608–1623.

[23] V. F. Cardoso, A. Francesko, C. Ribeiro, M. Bañobre-López, P. Martins, S. Lanceros-Mendez, Advances in Magnetic Nanoparticles for Biomedical Applications, *Advanced Healthcare Materials,* **7(5),** 2018, 17000845.

[24] N. A. Frey, S. Peng, K. Cheng, and S. Sun, Magnetic nanoparticles: synthesis, functionalization, and applications in bioimaging and magnetic energy storage. *Chem. Soc. Rev.***38**, 2009, 2532.

[25] S.-J. Yen, E.-C.Chen, R.-K. Chiang, & T.-M. Wu, Preparation and characterization of polypyrrole/magnetite nanocomposites synthesized byin situ chemical oxidative polymerization. *J. Polym. Sci. Part B Polym. Phys.***46**, 2008, 1291–1300.

[26] M. Wysocka-Żołopa, A. Brzózka, E. Zambrzycka-Szelewa, U. Klekotka,·B. Kalska-Szostko, K. Winkler, Structure and electrochemical properties of magnetite and polypyrrole nanocomposites formed by pyrrole oxidation with magnetite nanoparticles, *Journal of Solid State Electrochemistry,* **27**, 2023, 1919–1934.

[27] Y.He, Dai, X. Zhang, Y. Sun, W. Shi, D. Ge The Bioactive Polypyrrole/Polydopamine Nanowire Coating with Enhanced Osteogenic Differentiation Ability with Electrical Stimulation, *Coatings* **10(12)**, 2020, 1189.

[28] Md. K. Hossain, Md. M. Hasan, Md. S. Islam, O. T. Mefford, H. Ahmad, and Md. M. Rahman, Polypyrrole Coating via Lemieux-von Rudloff Oxidation on Magnetite Nanoparticles for Highly Efficient Removal of Chromium(VI) from Wastewater, *ACS Omega* **9,** 2024, 17, 19077–19088.

[29] Y.-L. Luo, Li-H. Fan, F. Xu, Y.-S. Chen, C.-Hu Zhang, Q.-Bo Wei, Synthesis and characterization of Fe_3O_4/PPy/P(MAA-co-AAm) trilayered composite microspheres with electric, magnetic and pH response characteristics. *Mater. Chem. Phys.***120**, 2010, 590–597.

[30] K. Cheah, M. Forsyth, V.-T. Truong, Ordering and stability in conducting polypyrrole. *Synth. Met .***94**, 1998, 215–219.

[31] H. Zhang, X. Zhong, J.-J. Xu, and H.-Y. Chen, Fe_3O_4 /Polypyrrole/Au Nanocomposites with Core/Shell/Shell Structure: Synthesis, Characterization, and Their Electrochemical Properties. *Langmuir* **24**, 2008, 13748–13752.

[32] M. T. Ramesan, Preparation and Properties of Fe_3O_4 /Polypyrrole/Poly(Pyrrole-Co-Acrylamide) Nanocomposites. *Int. J. Polym. Mater.***62**,2013, 277–283.

[33] V. V. Karambelkar, J. D. Ekhe, and S. N. Paul, High yield polypyrrole: A novel approach to synthesis and characterization. *J. Mater. Sci.***46**, 2011, 5324–5331.

[34] N. Arsalani, and K. E. Geckeler, Novel electrically conducting polymer hybrids with polypyrrole. *React. Funct. Polym.***33**, 1977, 167–172.

[35] L. G. Wade, *Organic chemistry*. Pearson Education India, 2008.

[36] J. Guo, H. Gu, H. Wei, Q. Zhang, N. Haldolaarachchige, Y. Li, D. P. Young, S. Wei and Z. Guo Magnetite–Polypyrrole Metacomposites: Dielectric Properties and Magnetoresistance Behavior. *J. Phys. Chem. C***117**, 2013, 10191–10202.

[37] F. F. Fang, Y. D. Liu, & H. J. Choi, Electrorheological and magnetorheological response of polypyrrole/magnetite nanocomposite particles. *Colloid Polym. Sci.***291**, 2013, 1781–1786.

[38] S. Varshney, A. Ohlan, V. K. Jain, V. P. Dutta, and S. K. Dhawan, Synthesis of ferrofluid based nanoarchitectured polypyrrole composites and its application for electromagnetic shielding. *Mater. Chem. Phys.***143**, 2014, 806–813.

[39] C. R. Vestal, and Z. J. Zhang, Effects of Surface Coordination Chemistry on the Magnetic Properties of $MnFe_2O_4$ Spinel Ferrite Nanoparticles. *J. Am. Chem. Soc.***125**, 2003, 9828–9833.

[40] E. Karaoğlu, Baykal, H. Deligöz, M. S¸enel, H. Sözeri, M.S. Toprak, Synthesis and characteristics of poly (3-pyrrol-1-ylpropanoic acid) (PPyAA)–Fe_3O_4 nanocomposite. *J. Alloys Compd.* **509**, 2011, 8460–8468.

[41] P. Xu, X. Han, C. Wang, H. Zhao, J. Wang, X. Wang and B. Zhang, Synthesis of Electromagnetic Functionalized Barium Ferrite

Nanoparticles Embedded in Polypyrrole. *J. Phys. Chem. B* **112**, 2008, 2775–2781.

[42] K. R. Reddy, K. P. Lee, and A. I. Gopalan, Self-assembly approach for the synthesis of electro-magnetic functionalized Fe3O4/polyaniline nanocomposites: Effect of dopant on the properties. *Colloids Surf. Physicochem. Eng. Asp.***320**, 2008, 49–56.

[43] J. Deng, X. Ding. W. Zhang, Y. Peng, J. Wang, X. Long, P. Li, A. S. C. Chan, Magnetic and conducting Fe_3O_4 –cross-linked polyaniline nanoparticles with core–shell structure. *Polymer* **43**, 2002, 2179–2184.

[44] K. Singh, A. Ohlan, R. K. Kotnala, A. K. Bakhshi, and S. K. Dhawan, Dielectric and magnetic properties of conducting ferromagnetic composite of polyaniline with γ-Fe_2O_3 nanoparticles. *Mater. Chem. Phys.***112**, 2008, 651–658.

[45] R. Turcu, O. Pana, A Nan, I Craciunescu, O Chauvet and C Payen Polypyrrole coated magnetite nanoparticles from water based nanofluids. *J. Phys. Appl. Phys.***41**, 2008, 245002.

[46] L. Chang, L. Xie, M. Liu, Q. Li, Y. Dong, C. Chang, X.-M. Wang and A. Inoue, Novel Fe-based nanocrystalline powder cores with excellent magnetic properties produced using gas-atomized powder. *J. Magn. Magn. Mater.***452**, 2018, 442–446.

[47] J. R. Brauer, Z. J. Cendes, B. C. Beihoff, and K. P. Phillips, Laminated steel eddy current loss versus frequency computed using finite elements. *IEEE Trans. Ind. Appl.***36**, 2000, 1132–1137.

[48] X. Li, J. Zhou, L. Shen, B. Sun, H. Bai, W. Wang, Exceptionally High Saturation Magnetic Flux Density and Ultralow Coercivity via an Amorphous–Nanocrystalline Transitional Microstructure in an FeCo-Based Alloy, *Advanced Materials* **35**, 2023, 2205863.

[49] T., Suetsuna, S. Suenaga, & Harada, K. Bulk nanogranular composite of magnetic metal and insulating oxide matrix. *Scr. Mater.***113**, 201), 89–92.

[50] S. Mori, T. Mitsuoka, K. Sugimura, R. Hirayama, M. Sonehara, T. Sato, N. Matsushita, Core-shell structured Mn-Zn-Fe ferrite/Fe-Si-Cr particles for magnetic composite cores with low loss. *Adv. Powder Technol.* **29**, 2018, 1481–1486.

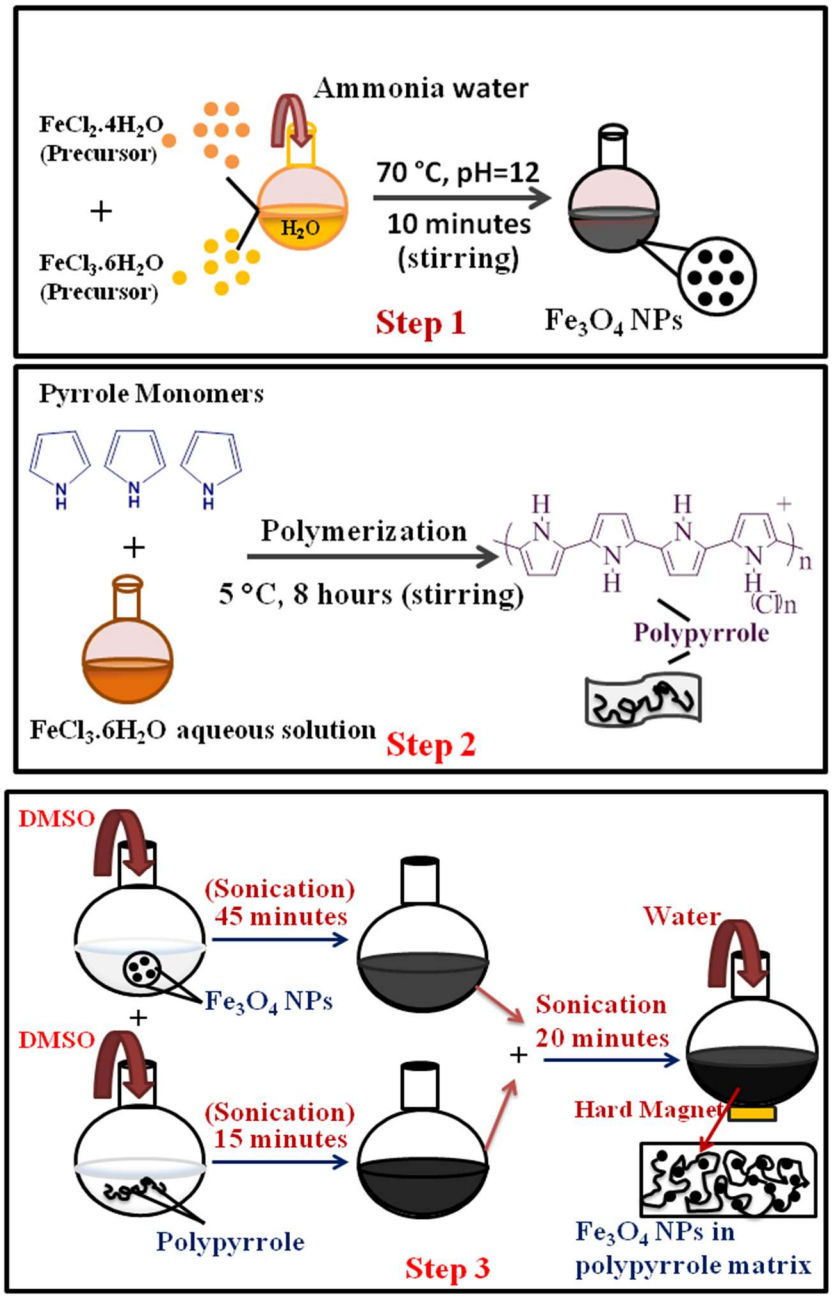
Ammonia water
FeCl2.4H2O
(Precursor)
+
FeCl3.6H2O
(Precursor)
H2O
70 °C, pH=12
10 minutes
(stirring)
Step 1
Fe3O4 NPs
Pyrrole Monomers
+
Polymerization
5 °C, 8 hours (stirring)
Polypyrrole
FeCl3.6H2O aqueous solution
Step 2
DMSO
(Sonication)
45 minutes
Fe3O4 NPs
+
DMSO
(Sonication)
15 minutes
Polypyrrole
Water
Sonication
20 minutes
Hard Magnet
Fe3O4 NPs in
polypyrrole matrix
Step 3

Figure 1

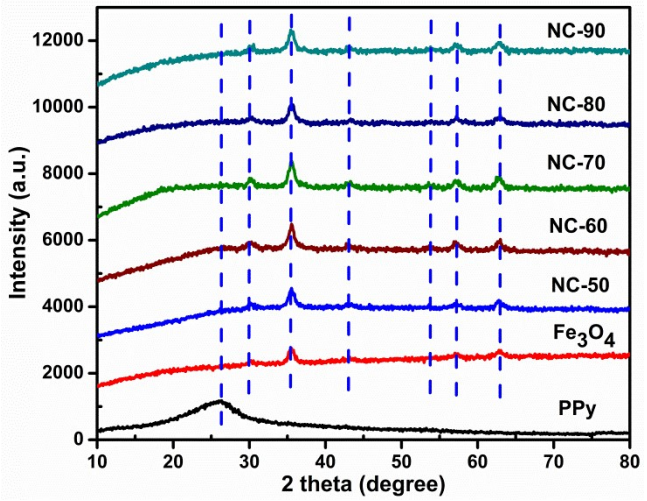

Figure 2

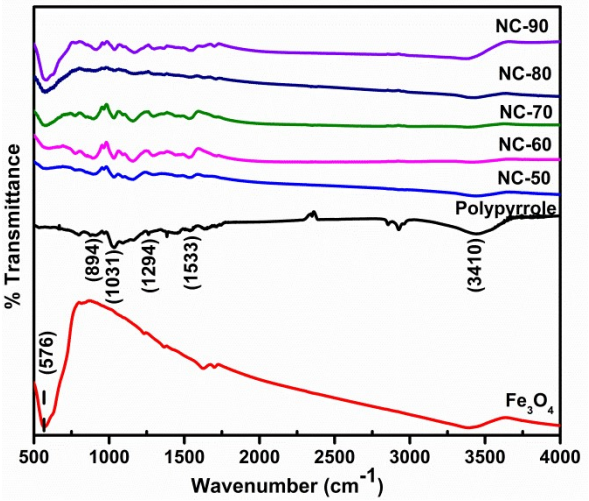

Figure 3

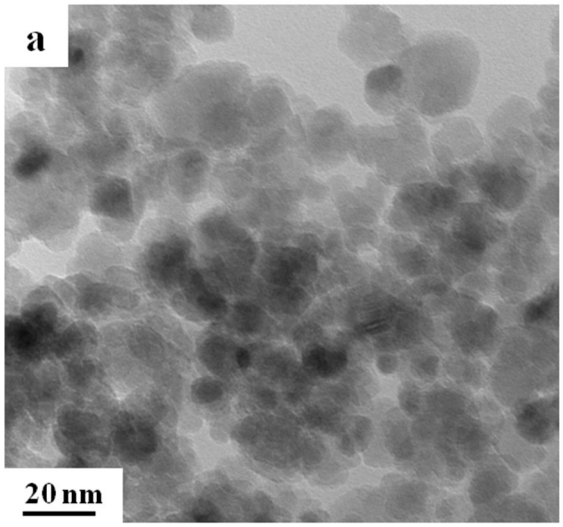

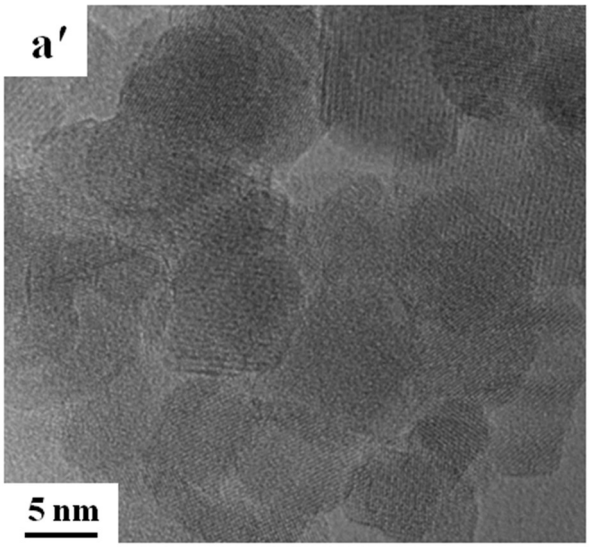

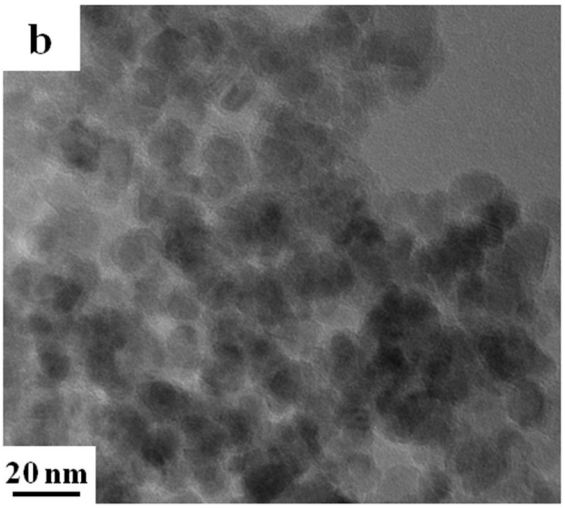

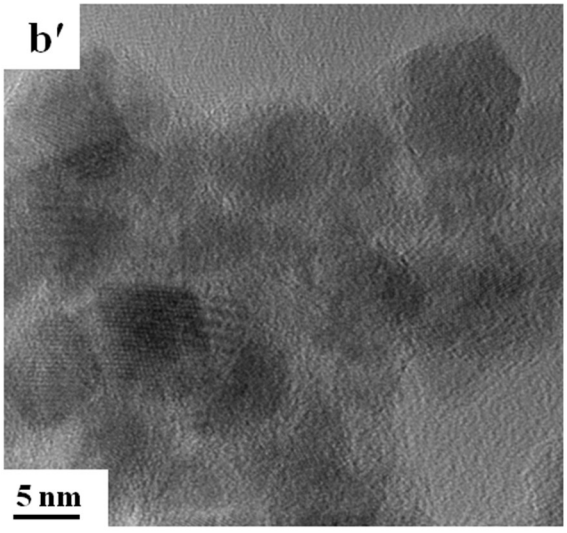

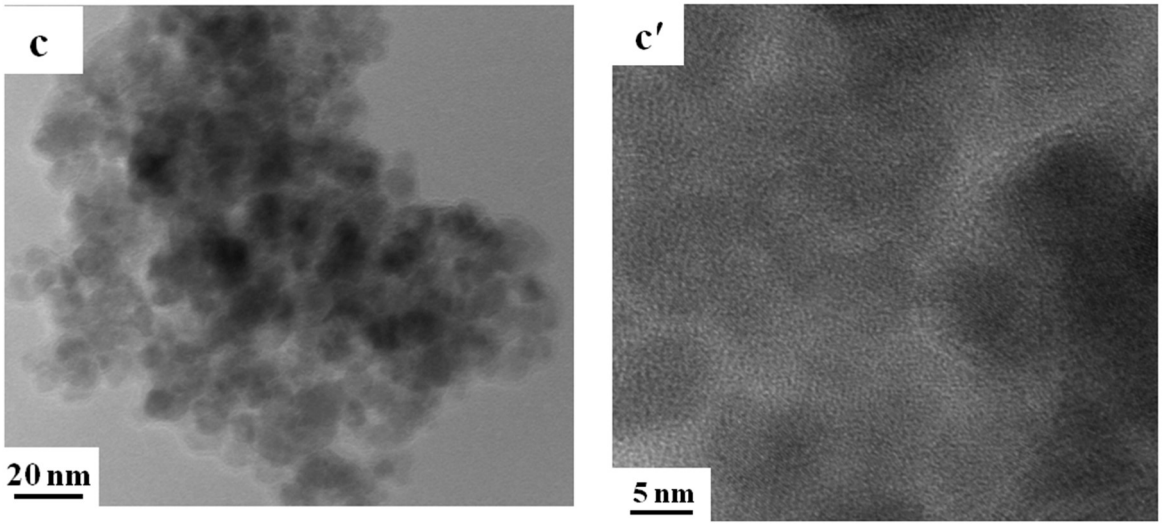

Figure 4

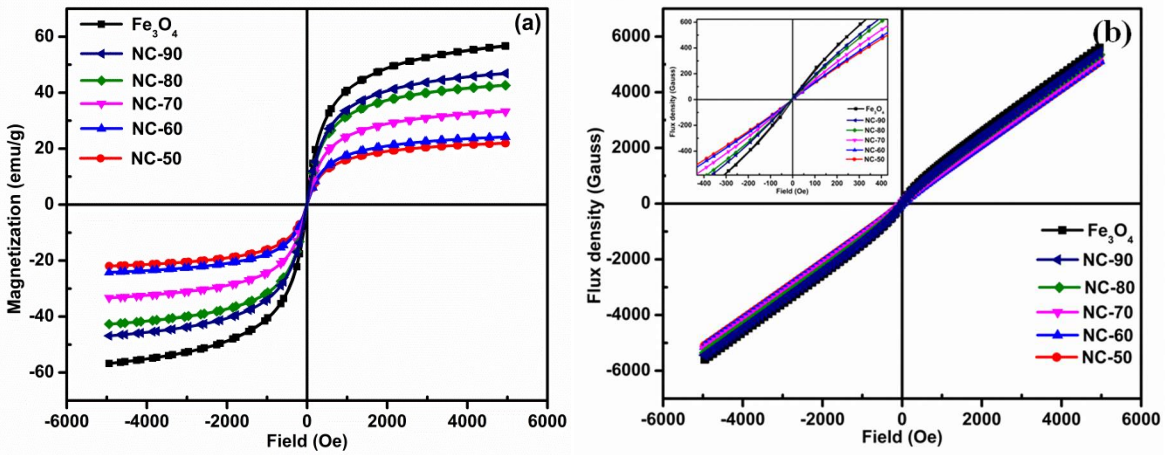

Figure 5

Table 1

	Saturation magnetization (M_s) (emu/g)	Saturation flux density (B_s)(Gauss)	Coercivity (H_c) (Oe)	Hysteresis losses (erg/cm^3)	K×μ_o
Fe_3O_4NPs	56.6	5,600	6.87	8576	388
NC-90	46.7	5,500	5	6467	233.5
NC-80	42.7	5,400	4	5367	170.8
NC-70	33.2	5,300	3.74	4558	124.16
NC-60	24.1	5,200	2.93	3751	70.613
NC-50	21.9	5,100	2.28	2455	49.932

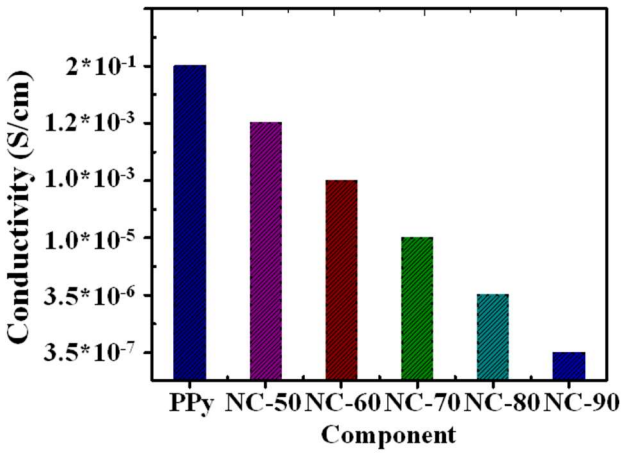

Figure 6

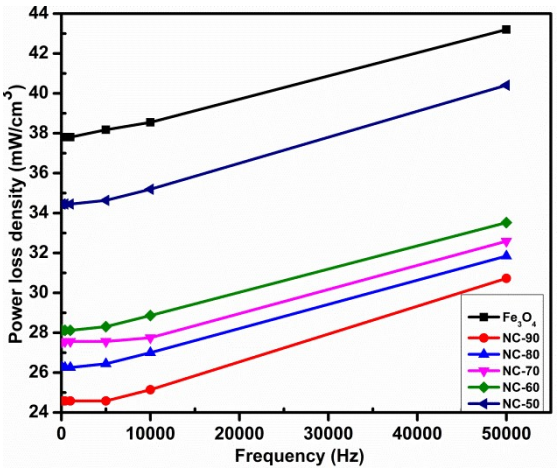

Figure 7

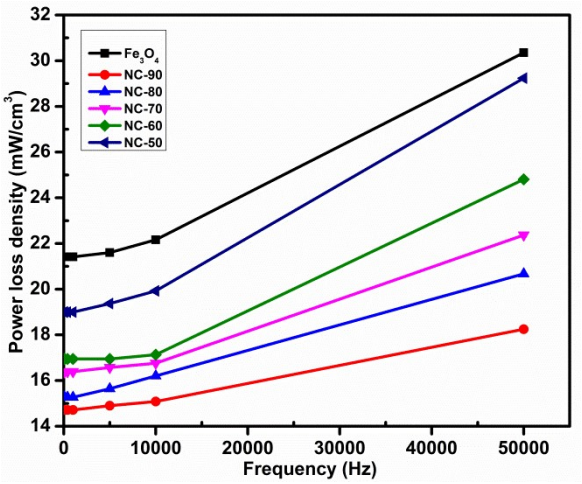

Figure 8

Introduction to Polymer Composites in Aerospace

Sayyed Samir[1]*, Jeeban Pd Gewali[1], Taranjit Singh[1], Karnilian Debbarma[1], Subhrojeet Mazumdar[1], Faizul Lone[1], Uwera Ed Daniella[1]

[1]*School of Mechanical Engineering, Lovely Professional University, Phagwara, Punjab144401, India*

Volume 1, Issue 4, July 2024
Received:29 May, 2024; Accepted: 27 June, 2024
DOI: https://doi.org/10.63015/4E-2431.1.4

**Corresponding Author Email: sameerrsayyed1@gmail.com.*

Abstract: The strategic use of polymer composites in aerospace engineering has influenced aircraft and spacecraft design and manufacturing. This abstract summarizes the fundamental principles, key components, and significance of polymer composites in aerospace applications. Polymer composites are formed of a matrix material (generally a polymer resin) reinforced with high-strength fibres like carbon, glass, or aramid. This combination gives the composite superior mechanical properties, such as high strength-to-weight ratio, stiffness, and resistance to fatigue and corrosion. Such properties make polymer composites ideal for aerospace structures where lightweight construction and exceptional performance are critical. Polymer composites are widely used in aerospace to reduce weight, improve fuel efficiency, and strengthen structural integrity in structural components such as wings, empennages, and fuselages. They are also essential to propulsion systems, interior structures, and thermal protection systems, which emphasizes their adaptability and versatility to a wide range of aerospace applications. The use of polymer composites in aerospace has driven improvements in manufacturing processes, including automated resin transfer molding and fibre placement, making it possible to produce intricate composite structures with extreme efficiency and precision. Furthermore, engineers can maximize component performance while adhering to strict aerospace regulations and safety standards thanks to the design flexibility provided by polymer composites. Further study attempts to boost the capabilities and characteristics of polymer composites, such as better resistance to damage, durability to impacts, and durability in extreme conditions. The invention of the next-generation aerospace vehicles that can meet the changing needs of space exploration and transportation looks promising as a result of this ongoing innovation.

Keywords: Aerospace, Composites, Polymer, Strength, Efficiency, Manufacturing, Innovation

1. Overview of Aerospace Materials:

Usually, traditional materials with fundamental strength and endurance, such steel, titanium and aluminium, have dominated the area of aircraft engineering for a long time. But because of their high weight, they present serious problems that raise fuel consumption and operating expenses for planes and spacecraft. Moreover, these materials have a tendency to corrosion and get fatigued over time, requiring costly and time-consuming routine maintenance and repairs. Presently, composite polymers provide a strong substitute for the drawbacks of conventional aircraft materials. Composite polymers surpass their traditional equivalents in strength-to-weight ratios by creatively fusing a polymer matrix with reinforcing fibres, such carbon or glass. This leads to much lighter aircraft and spacecraft, which increases fuel economy and lowers total operating costs. Additionally, composite polymers have outstanding resistance to fatigue and corrosion, prolonging the life of aeronautical components and reducing maintenance needs. Because composite polymers are lightweight, they improve fuel economy and reduce carbon emissions, which promotes environmental sustainability. This is in line with the aircraft industry's growing emphasis on environmentally friendly policies and procedures. Furthermore, composite polymers'

strength, resistance to fatigue, and corrosion translate into longer service lives for aerospace components, which minimizes the need for regular replacements and repairs. This reduces operating expenses and improves overall safety by ensuring the structural integrity of spacecraft and airplanes over long-term operations [1, 2].

The use of composite polymers in aircraft engineering is a paradigm shift that provides answers to the persistent problems with traditional materials. This transition is visible in many aerospace applications, such as propulsion systems and internal structures, as well as structural elements like wings, fuselages, and empennages. Because composite polymers are so versatile, engineers can design and produce aerospace components more precisely and efficiently, achieving strict performance requirements and complying with safety rules as shown in figure 1. Ultimately, composite polymers represent a significant breakthrough in aircraft materials, providing a comprehensive response to the persistent problems associated with conventional materials such as titanium, steel, and aluminium. In contemporary aerospace engineering, their remarkable strength and durability, along with their lightweight nature, make them essential. As the aviation sector advances, composite polymers could have a big impact on how aircraft technology advances.

2. Literature Survey: Polymer composites are increasingly utilized in the automobile and aerospace industries for weight reduction, improved performance, and environmental sustainability [1, 2, 3]. Fiber-reinforced plastics (FRP) play a crucial role in the automobile industry, offering weight reduction potential, high specific strength, and stiffness (Alberto, 2013). Polymer composites provide advantages over steel in terms of weight reduction, styling flexibility, tooling cost reduction, rust resistance, noise reduction, and higher damping properties [4, 5].

The aerospace industry has seen a rise in the use of polymer composites for various components like tail fins, elevators, fuselage fairings, spoilers, and ailerons, leading to weight reduction and cost savings [8]. Research in advanced polymer composites is expanding, with a focus on recyclability, mechanical properties, reduced weight, and extended shelf life for future automotive applications [10].

Aerospace materials must meet specific requirements such as being lightweight, high strength, having good fracture resistance, and high damage tolerance [3, 12]. The aerospace industry's focus on lightweight materials is driven by the need to reduce operational costs, particularly fuel consumption, which accounts for a significant portion of aviation expenses.

Materials and structures are fundamental to the development of modern aerospace systems, impacting various stages of an aircraft's life cycle from design to disposal [3, 5 7]. This highlights the continuous evolution and importance of materials in the aerospace industry. Fiber-reinforced polymer composite materials are increasingly favored for aerospace applications, particularly as primary structural materials [11].

Challenges in composite materials include impact damage, damage tolerance, environmental degradation, and long-term durability [9, 10]. The aerospace industry faces issues in setting inspection intervals and defining repair levels for aircraft in service due to impact damage concerns [2, 5, 8].

The use of composites in aerospace structures demands high reliability and safety, leading to extensive testing at all stages of design, development, certification, and in-service inspection [1, 2].

Future developments in aerospace composites focus on cost reduction techniques, such as new process technologies like resin transfer moulding (RTM) and resin infusion moulding (RIM), stitched hybrids, and smart materials for improved performance and affordability [1, 4, 13].

3. Composite Polymers: Polymer matrix composites (PMCs), often called composite

polymers, are a class of innovative materials that are gaining popularity across several industries due to their exceptional mechanical properties and versatility. Reinforcing fibres, usually comprised of glass or carbon, and a polymer matrix make up the two major components of composite polymers. The reinforcing fibres function as load-bearing components to increase strength and stiffness, while the polymer matrix acts as a binding agent to give the composite cohesion and structural integrity.

A variety of polymers can be utilized to form the polymer matrix of composite polymers, including thermoplastic polymers like polyethylene, polypropylene, and polyamide, and thermosetting resins like epoxy, polyester, and phenolic. The required mechanical qualities, processing constraints, and environmental concerns are just a few of the variables that influence the choice of polymer matrix. A stiff and long-lasting matrix is produced by the irreversible chemical crosslinking reactions that thermosetting resins experience during curing, whereas thermoplastic polymers allow for repeated melting and reshaping, providing more manufacturing process flexibility. The mechanical performance of composite polymers is largely dependent on the reinforcing fibres. Carbon fibres are incredibly strong, rigid, and light-weight, which makes them perfect for high-performance applications where weight reduction is crucial. Carbon fibres are made from carbon precursor materials like pitch or polyacrylonitrile (PAN). In contrast to carbon fibres, glass fibres are less expensive and have superior strength and stiffness. They are mostly made of silica and various oxides. Other types of reinforcing fibres are natural fibres like flax and bamboo and aramid fibres like Kevlar, each having special qualities appropriate for particular uses [3, 4, 15].

3.1. Why polymer composites are widely used in aerospace:

- Because polymer composites are lightweight and can reduce an aircraft's overall weight by up to 40%, they are preferred in the aerospace industry.
- These materials are effective for aeronautical applications because they have particular strength qualities, which make them robust for their weight.
- Due to their superior resilience to fatigue and fractures, polymer composites are essential for withstanding the harsh conditions seen in aerospace applications.
- The materials address the demanding specifications of aircraft components by offering dimensional stability, low thermal expansion characteristics, and speed of manufacturing.
- High performance materials are frequently needed for aerospace applications, and because of their many benefits, polymer composites are the material of choice for many aircraft components [2, 8,16].

3.2. Scope of polymer composites in aerospace:

- In aerospace applications, polymer composites are essential, especially for parts like crew gear, solar array substrates, and cockpit interiors.
- Polymer composites have allowed modern military fighter aircraft to reduce weight by thirty percent, demonstrating their value in the construction of strong, lightweight aerospace structures.
- These composites comprise up to 80% of contemporary satellite launch vehicles and are widely employed in satellite components such equipment panels, antennae, and honeycomb structures.
- Polymer composites are perfect for a variety of aircraft applications, such as high-precision detectors and space structural equipment, because of their strength, resilience, and design flexibility.

- Polymer composites are becoming the material of choice in aircraft, replacing traditional materials because of their superior performance and ability to be tailored to specific requirements. [6, 16].

Polymer composites are categorized according to a number of factors, such as the kind of polymer matrix, the kind of reinforcing fibres, and the method of manufacture. Polymer matrix composites (PMCs), ceramic matrix composites (CMCs), and metal matrix composites (MMCs) are the three primary categories into which polymer composites are divided under one common classification approach. Depending on the kind of polymer matrix and reinforcing fibres, polymer composites can be divided into multiple subtypes:

4. Types of Fibre-reinforced polymer (FRP): Certainly! Let's delve into each type of fibre-reinforced polymer (FRP) in detail:

4.1. Carbon Fibre Reinforced Polymers (CFRPs): Composition: Carbon fibres are contained in a polymer matrix, usually epoxy resin, to form CFRPs. Carbon fibres are renowned for having remarkable rigidity and strength.

Properties: CFRPs exhibit outstanding strength-to-weight ratios, stiffness, and corrosion resistance. Because of their remarkable strength and low weight, they are perfect for industries including sporting goods, automotive, and aerospace where reducing weight is essential.

Applications: The high strength-to-weight ratio of CFRPs in aerospace helps with fuel efficiency and performance in structural components such as wings, fuselages, and empennages. In the automotive industry, CFRPs are employed in body panels and chassis components to reduce weight and improve fuel economy. Additionally, CFRPs are used in sporting goods such as bicycles, tennis rackets, and golf clubs due to their lightweight and high-performance characteristics [3, 4].

4.2. Glass Fibre Reinforced Polymers (GFRPs): Composition: GFRPs utilize glass fibres as the reinforcing phase, combined with a polymer matrix such as polyester or vinyl ester resin.

Properties: GFRPs offer good strength and stiffness properties at a lower cost compared to CFRPs. While not as lightweight or as strong as carbon fibres, glass fibres provide decent mechanical performance and corrosion resistance.

Applications: GFRPs find applications in various industries where moderate mechanical performance and cost-effectiveness are desired. In aerospace, GFRPs may be used in non-structural components like fairings and interior panels. They are also utilized in marine applications for boat hulls and components exposed to water environments. Moreover, GFRPs are common in automotive components, construction materials, and consumer goods due to their versatility and affordability [15].

4.3. Aramid Fibre Reinforced Polymers (AFRPs): Composition: AFRPs employ aramid fibres, such as Kevlar, as the reinforcing phase in a polymer matrix, typically epoxy or phenolic resin.

Properties: AFRPs exhibit high strength, excellent impact resistance, and good fatigue properties. Aramid fibres are renowned for their toughness and resistance to ballistic impact, making AFRPs suitable for applications requiring protection against projectiles and impacts.

Applications: In aerospace, AFRPs are used in ballistic protection systems, helicopter rotor blades, and components subjected to high-velocity impacts. They are also utilized in marine applications for boat hulls and protective structures. Additionally, AFRPs find applications in sporting goods, such as helmets and body Armor, where impact resistance is crucial [3, 4].

4.4. Natural Fibre Reinforced Polymers (NFRPs): Composition: NFRPs incorporate natural fibres, such as bamboo, flax, or hemp,

as the reinforcing phase in a polymer matrix, often bio-based resins like soy-based epoxy or polylactic acid (PLA).

Properties: NFRPs offer environmental benefits, including biodegradability and renewable sourcing. While natural fibres may not match the mechanical properties of synthetic fibres like carbon or glass, they still provide adequate strength and stiffness for certain applications.

Applications: NFRPs are utilized in industries seeking sustainable alternatives to traditional materials. In automotive applications, NFRPs are used in interior components, door panels, and trunk liners. In construction, NFRPs find use in building materials like insulation, panels, and roofing. Additionally, NFRPs are employed in packaging materials and consumer goods, where eco-friendly materials are favoured [3, 4].

Numerous industries, including construction, automotive, marine, aerospace, and sporting goods, use composite polymers. Because of their light-weight and high strength, composite polymers are widely utilized in aerospace for structural components such as aircraft wings, fuselages, empennages, and interior structures. Body panels, chassis parts, and interior trim are among the automotive applications of composite polymers designed to lighten vehicles and increase fuel economy. Due to their durability and corrosion resistance, composite polymers are used in the construction sector for infrastructure applications like decks, bridges, and reinforcement materials [1-4, 15]. Composite polymers are an innovative and adaptable class of materials that are driving breakthroughs across several sectors. Composite polymers are expected to have a big impact on the direction of materials science and engineering because of continuous research and development activities aimed at improving their characteristics and processing methods.

5. Advantages of Composite Polymers in Aerospace: Due to their many advantages over conventional materials like metal, composite polymers have completely changed the aerospace sector. These cutting-edge materials have revolutionized the design and production of airplanes and spacecraft. They are made of a polymer matrix reinforced with fibres like carbon or glass. The principal benefits of composite polymers in aeronautical applications are given below [1-3].

5.1. Light-weight: Composite polymers are significantly lighter than metals, resulting in reduced overall aircraft weight. This reduction in weight translates to improved fuel efficiency and increased range for aircraft, allowing for longer flights and reduced operating costs. Lighter aircraft also require less energy to propel, contributing to environmental sustainability by reducing carbon emissions.

5.2. High strength-to-weight ratio: Composite polymers exhibit exceptional strength-to-weight ratios, providing structural integrity comparable to metals but with lower weight. This allows engineers to design aerospace components that can withstand high loads and stresses while minimizing weight, enhancing overall performance and safety [1-3].

5.3. Corrosion resistance: Unlike metals, composite polymers are immune to corrosion, eliminating the risk of rust and degradation over time. This corrosion resistance extends the lifespan of aerospace components, reducing maintenance needs and associated costs.

5.4. Fatigue resistance: Composite polymers demonstrate excellent fatigue resistance, capable of withstanding repeated stress cycles without compromising structural integrity. This durability is particularly advantageous in aerospace applications, where components are subjected to fluctuating loads during flight.

5.5. Design flexibility: Composite polymers offer unparalleled design flexibility, allowing for the creation of complex shapes and aerodynamic designs that optimize performance. Engineers can tailor the properties of composite materials to meet specific aerodynamic requirements, resulting

in more efficient and streamlined aircraft designs [2, 3].

5.6. Improved thermal and electrical insulation: Composite polymers provide enhanced thermal and electrical insulation properties compared to metals. This insulation capability improves safety and efficiency in extreme conditions, such as high temperatures encountered during atmospheric re-entry or electrical insulation requirements in electronic components.

5.7. Reduced part count: The use of composite polymers often results in a reduction in part count compared to traditional metal structures. Simplified assembly processes and fewer components streamline manufacturing and maintenance operations, leading to lower operational costs and faster turnaround times.

5.8. Enhanced durability: Composite polymers offer superior durability, capable of withstanding harsh environmental conditions, including temperature extremes, humidity, and exposure to chemicals. This durability ensures the longevity of aerospace components, reducing the need for frequent replacements and repairs and improving overall mission reliability [1-3]. In conclusion, the advantages of composite polymers in aerospace applications are numerous and far-reaching, encompassing improvements in weight, strength, durability, design flexibility, and operational efficiency. These advanced materials have revolutionized aircraft and spacecraft design, enabling the development of safer, more efficient, and environmentally sustainable aerospace vehicles.

6. Applications in Aircraft Structures: Modern aerospace engineering provides extensive uses for composite polymers because of their unique combination of strength, durability, and light weight in aircraft components [1-4]. The primary uses of composite polymers in airplane structures are described in detail below:

6.1. Fuselage: Composite polymers are widely used in fuselage construction, where their lightweight nature offers significant advantages. By replacing traditional metal structures with composite materials, overall aircraft weight is reduced, leading to enhanced fuel efficiency and increased range. Additionally, composite polymers provide superior strength, contributing to the structural integrity of the fuselage and ensuring passenger safety during flight [2-4].

6.2. Wings: Composite materials play a crucial role in wing design, offering benefits such as improved aerodynamics and reduced drag. The use of composites in wings leads to enhanced fuel efficiency by minimizing air resistance and increasing lift-to-drag ratios. Furthermore, composite wings are lighter than their metal counterparts, resulting in overall weight savings for the aircraft and improved performance.

6.3. Empennage: The tail section of aircraft, including the horizontal and vertical stabilizers, benefits from the use of composite materials. Composite polymers exhibit a high strength-to-weight ratio, ensuring stability and control during flight while minimizing additional weight. The lightweight nature of composite empennage components contributes to overall aircraft efficiency and manoeuvrability.

6.4. Landing Gear: Components of the landing gear system, such as struts and fairings, often incorporate composite polymers. By utilizing composites in landing gear construction, the weight of the landing gear system is reduced, contributing to overall weight savings for the aircraft. The use of composite materials in landing gear components improves performance during take-off and landing, enhancing aircraft safety and efficiency [2, 4].

In conclusion, composite polymers are essential to aircraft structures because they provide a host of benefits like increased performance, greater strength, and lightweight design. Composite materials have revolutionized aerospace engineering, enabling the production of safer, more efficient, and environmentally sustainable

aircraft, from fuselages to wings and landing gear [1-4].

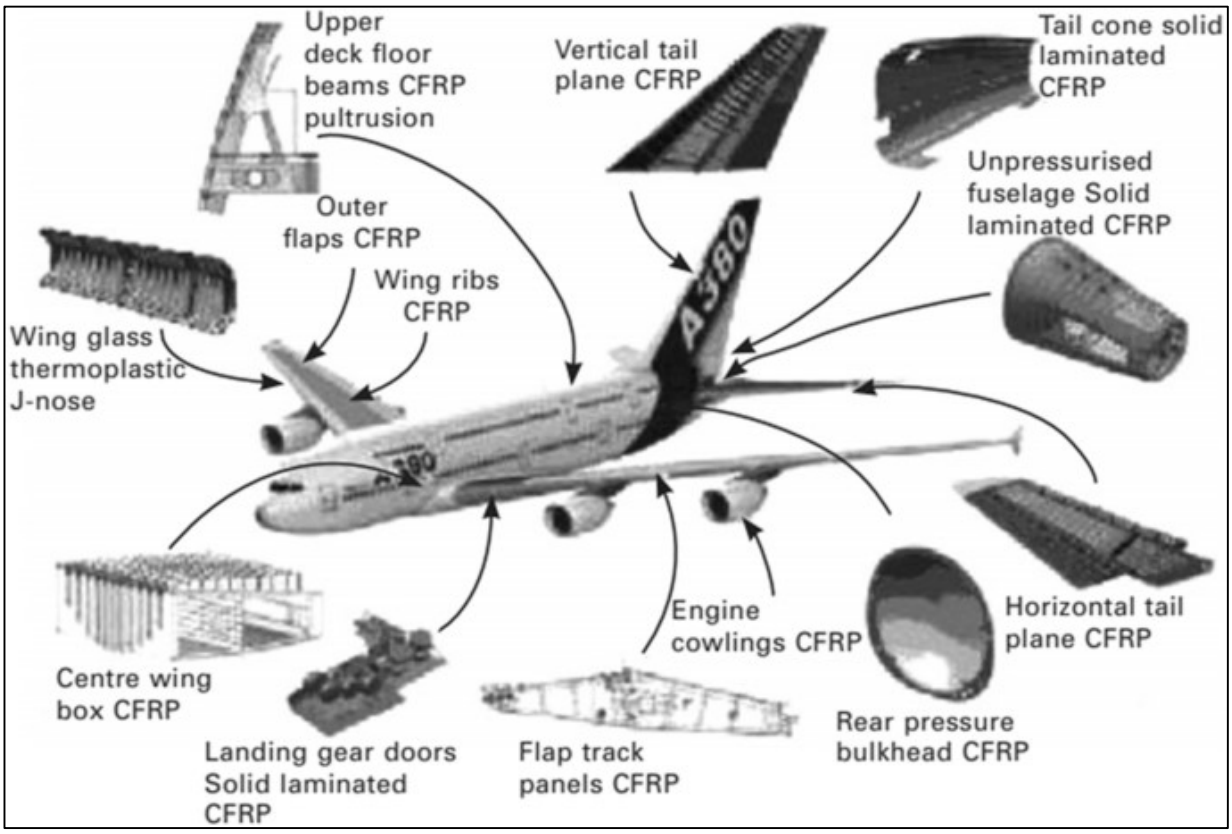

Figure 1. Advanced Polymer Composite for Aerospace Engineering Applications (N. Ramli, et al 2022) [17]

7. Manufacturing Processes Manufacturing Processes for Composite Polymers in Aerospace:

7.1. Hand layup: Process: Hand layup involves manually laying fibre reinforcements, such as carbon or glass fibres, into a mold. The fibres are then impregnated with resin, typically epoxy, polyester, or vinyl ester, to create the composite part.

Advantages: Hand layup offers flexibility for small-scale production and allows for the creation of complex shapes and structures. It works effectively for customizing and prototyping.

Challenges: However, hand layup can be labour-intensive and time-consuming. The manual process is also prone to variations in quality due to human error, leading to potential inconsistencies in the final product [5].

7.2. Automated Tape Laying (ATL): Process: ATL utilizes a computer-controlled machine to lay down pre-impregnated fibre tape onto a mold in precise patterns. The tape is typically pre-impregnated with resin, ensuring uniform distribution and controlled impregnation.

Advantages: ATL offers high precision and consistency, making it suitable for large and flat components like aircraft skins or panels. The automated process minimizes human error and increases production efficiency.

Challenges: However, ATL may not be suitable for components with complex geometries or curved surfaces, as the tape laying process is primarily linear and may struggle with intricate shapes [6].

7.3. Resin Transfer Molding (RTM): Process: RTM involves injecting liquid resin into a closed mold containing dry fibre reinforcements. The resin infiltrates the fibres,

saturating them completely, before curing to form the final composite part.

Advantages: RTM offers high production rates and excellent surface finish. It is suitable for high-volume production of aerospace components such as fairings or interior panels. The closed mold system minimizes waste and allows for precise control over resin flow.

Challenges: However, RTM requires specialized equipment and tooling, making it more suitable for mass production rather than small-scale or custom projects. The initial setup costs can be significant, and the process may be less adaptable to design changes compared to other methods [6].

7.4. Automated Fibre Placement (AFP): Process: Similar to ATL, AFP utilizes robotic arms to lay down continuous fibre reinforcements onto a mold. However, AFP offers increased flexibility in laying patterns, allowing for complex geometries and tailored fibre orientations.

Advantages: AFP is ideal for components with curved or contoured shapes, as the robotic arms can adjust fibre placement according to the design requirements. This flexibility allows for optimized fibre orientations and enhanced structural performance.

Challenges: AFP systems are complex and require skilled operators to program and operate effectively. Additionally, the equipment and tooling costs for AFP may be higher compared to other manufacturing processes [6].

In summary, every aircraft composite polymer manufacturing process has its own advantages and difficulties. Various criteria, including production volume, part complexity, design requirements, and budgetary restraints, must be taken into consideration while choosing the most suitable approach. Aerospace manufacturers can create high-quality composite components that satisfy the industry's strict performance requirements by efficiently utilizing these manufacturing techniques [7- 9].

8. Challenges and Limitations: Challenges and Limitations of Composite Polymers in Aerospace:

8.1. Cost: Initial Investment: One of the primary challenges with composite polymers in aerospace is the higher initial investment required for manufacturing facilities, equipment, and specialized tooling. Compared to traditional materials like metals, composite fabrication processes may involve costly machinery and infrastructure.

Material Expenses: Additionally, the raw materials used in composite polymers, such as carbon fibres and epoxy resin, can be more expensive than metals like aluminium or steel. This can significantly impact overall production costs, especially for large-scale manufacturing projects [2,3, 9, 15].

8.2. Complex manufacturing: Specialized Skills and Equipment: Composite fabrication requires specialized skills and equipment, including CNC machines, autoclaves, and robotic systems for automated layup processes. Aerospace manufacturers must invest in training programs to ensure their workforce possesses the necessary expertise to handle composite materials effectively [2].

Higher Production Complexities: The manufacturing processes for composite polymers, such as resin infusion or automated fibre placement, are more complex than traditional metal fabrication methods. This complexity can lead to longer production lead times, increased setup costs, and a higher likelihood of errors during manufacturing [3, 10, 14].

8.3. Inspection and maintenance: Detecting Defects: Detecting defects and ensuring structural integrity in composite materials can be challenging due to their heterogeneous nature and anisotropic properties. Traditional inspection methods, such as visual inspection or ultrasonic testing, may not always be effective in identifying internal flaws or delamination [2].

Advanced Inspection Techniques: Aerospace manufacturers must invest in advanced

inspection techniques, such as computed tomography (CT) scanning or thermography, to accurately assess the quality of composite components. These techniques require specialized equipment and expertise, adding to the overall complexity and cost of quality control processes [2, 3, 14].

Maintenance Challenges: While composite materials offer excellent durability and resistance to corrosion, they are not immune to damage from impact, fatigue, or environmental factors. Repairing composite structures may require specialized techniques and materials, adding to maintenance costs and downtime for aircraft or spacecraft [3, 11, 14].

8.4. Environmental concerns: Disposal and Recycling: The disposal of composite materials at the end of their service life raises sustainability concerns, as traditional recycling methods may not be suitable for composite waste. Composite polymers are typically non-biodegradable and can pose challenges for landfill disposal.

Eco-friendly Solutions: Aerospace manufacturers are increasingly exploring eco-friendly recycling solutions for composite waste management, such as pyrolysis or mechanical recycling processes. However, developing cost-effective and efficient recycling technologies for composite materials remains a significant challenge [2, 3, 12].

In conclusion, while composite polymers offer numerous advantages for aerospace applications, including lightweight construction and superior performance, they also present challenges and limitations that must be addressed. Aerospace manufacturers must navigate these challenges through investment in research and development, advanced manufacturing techniques, and sustainable practices to maximize the benefits of composite materials while mitigating their drawbacks [9-12].

9. Research and Development: To encourage innovation and get over current obstacles, research and development (R&D) in composite polymers for aeronautical applications is essential. One area of interest is the development of fibres, including glass and carbon, to improve their stiffness, strength, and light weight. In order to produce stronger and lighter composite materials, researchers are working to create fibres with improved performance properties. In order to meet the demanding requirements of aircraft settings, R&D efforts also focus on developing resins with enhanced toughness, durability, and temperature resistance [3, 9, 13, 14]. Another significant aspect of composite polymer R&D is sustainability, with scientists looking at recycling techniques and environmentally benign substitutes to allay worries about the environmental impact of composite disposal. This involves minimizing waste and the environmental impact of composite materials by researching bio-based polymers and creating effective recycling techniques [2, 3, 13].

Composite technology advances are mostly driven by collaborative innovation, where collaborations between academics and industry facilitate information exchange and accelerate growth. Through these collaborations, researchers are able to pool resources and experience from several disciplines to address complex challenges related to composite materials and production processes. Ultimately, this leads to the development of aerospace technologies that are safer, more effective, and sustainable [3, 6, 13].

10. Future Trends: The development of innovative materials with superior qualities, such as higher strength and reduced weight, as well as the integration of smart technologies for improved functionality, is the direction of future trends in composite polymers for aerospace applications. Future developments are expected to push the limits of existing composite technology, opening the door to lighter and stronger aircraft constructions [3, 9].

Composite polymers have the potential to transform a number of aerospace industries by expanding their applications beyond

conventional airplanes to include satellites and drones. With these increased uses, composite materials will be able to significantly influence how aircraft engineering develops in the future, spurring creativity and changing the face of air travel. Composite polymers will surely continue to lead the way as the sector develops, generating innovations and stretching the limits of what is feasible in aircraft technology [3, 13].

11. Conclusion: In conclusion, composite polymers represent a revolutionary advancement in aerospace materials, offering transformative benefits such as weight reduction, increased durability, and enhanced design flexibility. These advancements are reshaping the landscape of air travel by improving efficiency, performance, and safety standards across various aerospace sectors. To fully utilize composite polymers in aerospace, however, is still a trip away. In order to guarantee composite materials' broad acceptance and continuous progress in the aerospace sector, research and development endeavours must be carried out with an ongoing innovative mindset. Furthermore, advancing innovation and expanding the frontiers of composite technology requires cooperative efforts between business, academia, and research centres. In concert, stakeholders may overcome obstacles, quicken progress, and open up opportunities for the development of aerospace engineering by pooling their expertise and financial resources.

References:

[1] S. Kesarwani, "Polymer Composites in Aviation Sector," Int. J. Eng. Res. Technol. (IJERT), vol. 06, no. 06, June 2017,http://dx.doi.org/10.17577/IJERTV6IS060291.

[2] P. D. Mangalgiri, "Composite materials for aerospace applications," Bull. Mater. Sci., vol. 22, no. 3, pp. 657-664, May 1999, https://doi.org/10.1007/BF02749982.

[3] B. Parveez et al., "Scientific Advancements in Composite Materials for Aircraft Applications: A Review," Polymers (Basel), vol. 14, no. 22, Nov. 2022, Art. no. 5007, https://doi.org/10.3390%2Fpolym14225007.

[4] S. Devaraju and M. Alagar, "Polymer Matrix Composite Materials for Aerospace Applications," 2021, http://dx.doi.org/10.1016/B978-0-12-819724-0.00052-5.

[5] D. R. Askeland and P. P. Fulay, Essentials of Materials Science and Engineering, Cengage Learning, 2016.

[6] K. Balasubramanian, M. T. H. Sultan, and N. Rajeswari, "Manufacturing techniques of composites for aerospace applications," in Sustainable Composites for Aerospace Applications, M. Jawaid and M. Thariq, Eds., Woodhead Publishing, 2018, pp. 55-67,https://doi.org/10.1016/B978-0-08-102131-6.00004-9.

[7] P. K. Mallick, Fibre-Reinforced Composites: Materials, Manufacturing, and Design, CRC Press, 2007.

[8] A. Mcilhagger, E. Archer, and R. Mcilhagger, "Manufacturing processes for composite materials and components for aerospace applications," in Polymer Composites in the Aerospace Industry (Second Edition), P. Irving and C. Soutis, Eds., Woodhead Publishing, 2020, pp. 59-81,https://doi.org/10.1016/B978-0-08-102679-3.00003-4.

[9] A. Matzenmiller and S. W. Tsai, "Composite Materials in Aerospace Engineering," in Encyclopedia of Aerospace Engineering, Wiley, 2010, pp. 1-10.

[10] R. F. Gibson et al., "Composite Materials," in Materials Science and Engineering: An Introduction, 10th ed., John Wiley & Sons, Inc., 2017.

[11] K. K. Chawla, Composite Materials: Science and Engineering, Springer, 2012.

[12] Ince, J.C., Peerzada, M., Mathews, L.D. et al. Overview of emerging hybrid and composite materials for space applications. Adv Compos Hybrid Mater 6, 130 (2023). https://doi.org/10.1007/s42114-023-00678-5.

[13] A. Kelly and C. Zweben, "Introduction and Historical Perspective," in Comprehensive Composite Materials, A. Kelly and C. Zweben, Eds., vol. 1, Elsevier, 2000, pp. 1-10.

[14] N. Ramli, M. Norkhairunnisa, Y. Ando, K. Abdan, and Z. Leman, "Advanced Polymer Composite for Aerospace Engineering Applications," in *Advanced Composites in Aerospace Engineering Applications*, N. Mazlan, S. Sapuan, and R. Ilyas, Eds. Cham: Springer, 2022, pp. 1–15. https://doi.org/10.1007/978-3-030-88192-4_1.

[15] Aamir, M., Tolouei-Rad, M., Giasin, K., et al. "Recent advances in drilling of carbon fiber–reinforced polymers for aerospace applications: a review." International Journal of Advanced Manufacturing Technology, vol. 105, pp. 2289–2308, 2019. https://doi.org/10.1007/s00170-019-04348-z.

[16] S. W. Ghori, R. Siakeng, M. Rasheed, N. Saba, and M. Jawaid, "The role of advanced polymer materials in aerospace," in *Sustainable Composites for Aerospace Applications*, M. Jawaid and M. Thariq, Eds. Woodhead Publishing, 2018, pp. 19-34. https://doi.org/10.1016/B978-0-08-102131-6.00002-5.

[17] N. Ramli, M. Norkhairunnisa, Y. Ando, K. Abdan, and Z. Leman, "Advanced Polymer Composite for Aerospace Engineering Applications," in *Advanced Composites in Aerospace Engineering Applications*, N. Mazlan, S. Sapuan, and R. Ilyas, Eds. Cham, Switzerland: Springer, 2022 https://doi.org/10.1007/978-3-030-88192-4_1.

Structural, Optical & Dielectric Behavioural Analysis of Nb_2O_5-V_2O_5 Modified Barium-Boro-Bismuthate Glasses: Opto-Electronic Applications

Vikas Attri[1], M.S. Dahiya[1,2], Ashima Hooda[1], A. Agarwal[3] and Satish Khasa[1]*

[1] *Department of Physics, Deenbandhu Chhotu Ram University of Science and Technology, Murthal, Haryana, India*
[2] *Directorate of Education, Govt. of NCT, Delhi*
[3] *Department of Physics, Guru Gambheswer University of Science and Technology, Hisar, Haryana, India*

Volume 1, Issue 4, July 2024
Received:28 April, 2024; Accepted: 12 July, 2024
DOI: https://doi.org/10.63015/5C-2428.1.4

* *Corresponding Author Email: skhasa.phy@dcrustm.org*

Abstract: Barium-Boro-Bismuthate glasses modified with Nb_2O_5 and V_2O_5 having composition $x$$Nb_2O_5$-(10-$x$)$V_2O_5$-25BaO-30$B_2O_3-35Bi_2O_3$ (where x = 0, 1, 3, 5, 8, 9 and 10 mol%) were prepared via melt-quench technique and investigated for structural, optical, electrical and thermal properties. The produced glasses were subjected to thermal exposure for five hours at 450 °C in order to examine structural modifications inside the glass matrix. Densities of as-prepared glass samples were measured and values were found to lie in order of 5.5 g/cc. XRD profile containing broad humps for as-prepared glass samples reflected their amorphous nature, and ordered peak pattern for annealed glass samples reflected development of $Bi_{45}BO_{69}$ crystalline phase (with crystallite size < 50 nm) inside annealed glass matrix. FTIR spectroscopy helps in identification of different structural units (such as BO_4, BO_3, BiO_6 & BiO_3) inside base glass matrix. Dielectric analysis reflects usability of glass samples for high frequency signal transmission, high-temperature semi-conducting and energy storage devices. Lower value for ac conductivity (~10^{-5} S/m) reflects usability of glass samples towards high-voltage bearing materials (due to high resistance for electrical breakdown). Optical band-gaps (E_g) for as-prepared and annealed glass samples lie between 1.13 and 2.39 eV, suggesting their usability towards various optical and opto-electronic devices (such as absorber material in solar cells, optical fibre, lenses, filters, etc.). A non-significant change in refractive index values for as-prepared glass samples after annealing reflected enlisted these into transparent glass ceramic category. A single sharp exothermic peak in each differential thermal analysis (DTA) curve reflects nucleating ability of as-prepared glass samples.

Keywords: Nano-crystallites, optical band-gap, refractive indices, ac conductivity, differential thermal analysis, transparent glass ceramics, mixed transition metal effect

1. Introduction: The demand for low-cost, sustainable, chemically robust, and dependable materials for optoelectronic devices is rising quickly. Consequently, enormous research efforts have been made by scientists all over the world to create novel materials that fulfil these specifications. Researchers have focused especially on oxide glasses (including borate, vanadate, bismuthate, and tellurite) imparting transition metals due to their usability in optoelectronic devices. These glasses can be prepared in order to target a particular application or behaviour, such as insulation, conduction, optical transparency, low melting point, waveguide, water resistance, etc. [1–5]. Boro-bismuthate glass network mainly contains three and four coordinated borate units (i.e. BO_3 and BO_4) along with three and six coordinated bismuthate units (i.e. BiO_3 and BiO_6). Modification of glass matrix with alkali oxides or alkali earth oxides (like BaO, Li_2O, etc.) in boro-bismuthate glass network endows their physical, optical, thermal and electrical properties by defining the glass matrix [6–8].

The presence of transition metal ions (TMIs) in glass matrix causes enhancements in thermal and spectroscopic properties due to polaronic conductions, local order or disorder in glass matrix and hoping of charge carriers [9]. TMI's such as Nb, Fe, V, Co, etc. were coordinated with non-bridging oxygen (i.e. compensating the extra charge and found to form some extrinsic dipoles to form a trap type entity where the charge carriers (electrons and holes) will be trapped and dipole polarization will occur inside the glass matrix [9–11]. The existence of TMIs in multiple oxidation states makes these materials (glass or glass-ceramics) useful for applications like UV irradiation shielding windows and glass lasers. These ions can mainly act as network modifiers or formers helping to tailor electrical, optical, and thermal properties of glasses [12–14].

Glasses containing Nb_2O_5 can be treated as usable materials for piezoelectric, semi-conducting and radiation shielding materials with high stimulated emission parameters [13]. The addition of V_2O_5 and Nb_2O_5 causes enhancements in optical and thermal behaviour of boro-bismuthate glass matrix [15–19]. With all these enhancements, these oxides (or ions) also intensify the crystallization abilities of glass matrix [1,20]. Alongside the investigation of the borate network, the spectroscopic futures of Nb_2O_5 placed into the network were also being examined. It was found that borate glasses containing Nb_2O_5 exhibit substantial UV absorption, better transparency in the visible-IR range, enhanced nonlinear optical properties and possess high refractive indices [21]. Moreover, Nb_2O_5 exists in Nb^{4+} and Nb^{5+} oxidation states, which helps to increase electrical conductivity (through polaronic conduction contribution) of glass samples. Boro-bismuthate glasses having niobium metal oxide possess large chemical resistance, high refractive index, high vickers hardness, fair transparency in Vis-IR region [13,16]. A number of researchers tried to investigate structural contribution of Nb_2O_5 in various silicate, germanate and borate glass matrices, as per IR and Raman spectroscopic outcomes [17,22,23]. Majority of these investigations suggest existence of Nb^{5+} ions (i.e. Nb_2O_5 acts as glass formers), which have a significant effect on thermal and opto-electrical properties of glass systems. The addition of Nb_2O_5 increases the crystal field strength, helps for phase separation and helps increase the nucleation ability of glass system [1,13,14,16,25–30,31–34,]. An enhancement in physical, electrical, optical properties, with addition of TMI's has been observed in literature [5,27,34–36]. The dynamics of multi TMIs in barium-boro-bismuthate glass systems may therefore be interesting to investigate. Keeping in mind these facts, the study aims to investigate how the inclusion of Nb_2O_5 at the cost of V_2O_5 affects the optical, electrical and thermal abilities of barium boro-bismuthate glass system.

2 Sample Synthesis and Experimental Techniques

2.1 Glass synthesis

Nb_2O_5-V_2O_5 substituted barium boro-bismuthate glass samples with chemical composition $x$$Nb_2O_5$-(10-$x$)$V_2O_5$-25BaO-30$B_2O_3-35Bi_2O_3$ (where x can take values from 0.0, 1.0, 3.0, 5.0, 8.0, 9.0 and 10.0) were prepared using melt-quench methodology and shortened as NVBBBx (where x = 0, 1, 3, 5, 8, 9 and 10). For synthesis, the AR/GR grade starting raw chemicals (i.e. Bi_2O_3 (HIMEDIA, 99.5%), B_2O_3 (HIMEDIA (ACS grade, 99.8% pure)), BaO (HIMEDIA (ACS grade, 99%)), V_2O_5 and Nb_2O_3 (HIMEDIA (AR grade, 99.5%))) were weighed (as per composition) and mixed (homogenously) through agate pestle mortar. The prepared homogenous mixture was transferred to high alumina crucible and placed in electrical muffle furnace (operating at 1150°C) for an hour with regular shaking in every 15 minutes (in order to keep the melt homogenous). The obtained melt (mixture) was quenched or sandwiched between two preheated SS plates (in order to reduce thermal stress), resulting in glass samples with thickness ranging from 0.5 - 1 mm. Samples were polished and cut into rectangular shapes for dielectric studies. A portion of prepared glass samples was finely powdered for analyzing their optical, structural

and thermal behaviour. As-prepared glass samples were exposed thermally (annealed) at 450 °C for five hours in order to investigate any structural change or crystallite growth inside glass matrix.

2.2 Experimental Techniques

2.2.1 Density measurements

Density measurements (performed at room temperature via Archimedes principle) help to analyze the physical behaviour of sample. Xylene (density of 0.863 g/cc) was used as buoyant liquid (because of its inert nature with glasses). A digital single pen weighing balance (Model- CAS CAUY 220) with a minimum count of 0.1 mg, was used for weight recording. Density measurements and molar volume estimations for each prepared sample were performed as per relation (see equations (i & ii)) [18,37].

$$\rho = \frac{W_a}{W_a - W_x} \times \rho_x \qquad \text{(i)}$$

Here ρ, ρ_x are densities of glass sample and xylene, W_a, W_x are weights of glass sample in air and in xylene respectively. The molar volume (V_m) of prepared samples can be analyzed using molecular mass (M) and density (ρ) via relation given below.

$$V_m = \frac{M}{\rho} \qquad \text{(ii)}$$

2.2.2 X-ray diffraction (XRD) profile

Rigaku Ultima-IV, (X-ray diffractometer) working with Cu-Kα radiations (along with Kβ filter) at voltage and current of 40kV and 40mA respectively was used as XRD instrument for recording XRD profiles. Each profile was recorded within the 2θ range from 20° to 80° with scanning rate of 2°/min. Structural arrangement (amorphous/crystalline) of samples (as-prepared and annealed) were analyzed through obtained XRD profiles.

2.2.3 FTIR

FTIR spectroscopy helps to identify presence of functional groups, different structural units and provide their quantitative description. FTIR spectra of as-prepared glass samples were recorded through Perkin Elmer Frontier FTIR Spectrometer using KBr pellet technique. In KBr pellet technique, both sample powder and KBr were mixed homogenously in ~1:100. This mixture was put in 13mm radius die-set (dia. ~ 13mm) and then hydraulically pressed in order to get an almost transparent pellet. Spectral modifications such as baseline and noise corrections were performed using Spectrum 10 analysis software (available with instrument).

2.2.4 Dielectric analysis

A thin layer of colloidal silver paint was pasted at both ends (which helps to improve connectivity and act as electrodes) of rectangular shaped polished sample. The dielectric analysis was performed using impedance analyzer (model: HIOKI IM 3570) operating within frequency range from 1 kHz to 10^6 Hz and temperature range from ambient temperature to 450 °C with heating rate of 1 °C/min. Series capacitance (Cs), parallel capacitance (Cp), impedance (Z) and series resistance (Rs) were fetched from analyzer through external triggering at each temperature with a gap of 5 °C throughout the mentioned frequency range. The formulas used for calculation of dielectric parameters are listed below:

$$\varepsilon' = C_p t/(\varepsilon_\circ A) \qquad \text{(iii)}$$

$$tan\delta = \frac{\varepsilon''}{\varepsilon'} \qquad \text{(iv)}$$

$$\sigma_{ac} = 2\Pi f \varepsilon_\circ \varepsilon' tan\delta \qquad \text{(v)}$$

Where ε' is real and ε'' is imaginary component of dielectric constant (ε), ε_o is absolute dielectric permittivity, A, t, f, $tan\delta$ and σ_{ac} are area of cross-section, thickness of sample, frequency applied, loss tangent and ac conductivity respectively.

2.2.5 UV-Visible absorption

Optical behaviour of as-prepared glass samples was analyzed through UV-Vis NIR spectroscopy. UV-Vis absorption spectra (or optical absorption spectra) were performed at room temperature (for both as-prepared and annealed glasses) using Perkin Elmer LAMDA 750 UV-Vis NIR spectrophotometer, with wavelength range of operation from 300 nm to 900 nm at room temperature.

2.2.6 Differential Thermal Analysis (DTA)

The thermal behavioural analysis for as-prepared glass samples were analyzed using DTA thermograms. These thermograms were recorded using DTA simultaneous measuring instrument (model: DTG 60 H) in temperature ranging from 300°C to 600°C at a heating rate of 10°C/min.

3. Result and Discussion

3.1 Density measurements

Density measurement is a crucial intensive property of glasses as it helps to identify any structural change inside the glass matrix because of compositional alterations. Density of glass systems is generally controlled by various factors like ionic radii, size, mass of modifier and concentration of non-bridging oxygen inside glass matrix [15,38–40]. Table 1 contains measured density values and calculated molar volume values for as-prepared glass samples. Density values for present glass samples were found to lies around 5.5 g/cc to 6 g/cc. In general, addition of Nb_2O_5 with replacement of V_2O_5 is expected to provide an increase in density (due to increasing molar mass of composition) and thereby enhance the compactness of glass network. As expected, we have observed an increasing trend in density with enhanced Nb_2O_5 substitution.

Oxygen packing density (*OPD*) helps to analyze structural compactness of glass matrix (i.e. how tightly oxygen atoms are assigned). *OPD* for all as-prepared glass samples was calculated as per literature [40,41] and obtained values are reported in Table 1. During all compositions total number of oxygen atoms per formula unit remains invariant, which leads to almost similar values of *OPD* for as-prepared glass samples. Along with this, *OPD* can also be related to N_4 (concentration of four coordinated boron atoms) directly (i.e. the increase in N_4 leads decreases in V_m and increase in OPD) [42]. On behalf of increasing density, OPD values and decreasing molar volume, one can suggest that replacement of Nb_2O_5 in place of V_2O_5 causes strengthening of bonds present inside the glass matrix.

3.2 X-ray Diffraction (XRD)

XRD profile helps to analyze the structural arrangement of constituents in glass/glass ceramic network. Figures 1(a & b) shows X-ray Diffraction profiles of NVBBB (as-prepared and annealed) glass system. In Figure 1(a), appearance of a broad hump in diffraction pattern of each glass shows amorphous nature of all as-prepared glass samples (although, some nano-crystalline nucleating agents may be present with short range ordered structure) [33].

As-prepared glass samples were exposed thermally (annealed at ***450℃ for 5 hours),*** in order to identify any sort of crystalline phase growth inside the glass matrix on account of thermal induction (due to nucleation and growth processes) [43–45]. The availability of crystalline seeds with short range ordered structure led to the formation of crystalline phase in glass matrix which is evident through sharp peaks in obtained diffraction patterns (Figure 1(b)). These XRD profiles were analyzed by matching with JCPDS data and it was found that this diffraction data matches with crystallite phase of $Bi_{45}BO_{69}$ (JCPDS card number 42-0294). The size of crystallites developed inside the annealed glass matrix corresponding to the most intense peak (201) was calculated using Debye-Scherrer equation [18,46]. The XRD profile of annealed glass samples matches the diffraction profile of crystallite phase with chemical formula **$Bi_{45}BO_{69}$** (having JCPDS card number 42-0294). Other structural parameters such as lattice parameters (a,b,c), inter-planer spacing (*d*), calculated volume (V_{cal}), given volume (V_{given}) and lattice strain were also estimated and obtained values are reported in Table 2. A close analysis of data available in Table 2

concludes that nano-crystallites developed inside the glass matrix on annealing at 450 °C for 5 hours fulfil the conditions and criteria for use of these compositions as transparent glass ceramics (TGC).

3.3 Fourier Transform Infrared (FTIR) Spectroscopy

FTIR spectroscopy helps in identification of different structural units that constitute the glass matrix and functional groups in chemical composition of as-prepared glass samples. In order to identify existence of different structural units inside glass matrix, fingerprint region of FTIR spectra was analyzed. The fingerprint region of boro-bismuthate glasses consists of three wide absorption bands (i.e. bands from 1500 to 1100 cm^{-1}, from 1100 to 800 cm^{-1} and 800 to 600 cm^{-1}) corresponding to various bending and stretching vibrations in different structural units. The IR band from 1500 to 1100 cm^{-1} is due to B-O stretching vibrations in BO_3 structural units. With moving towards higher energy, band in 1100 to 800 cm^{-1} and from 800 to 600 cm^{-1} range arise due to stretching vibrations in BO_4 structural units and B-O-B bending vibrations in borate network respectively [27,47–51]. Addition of heavy metal oxides (like BaO and Bi_2O_3) reduces the phonon energy of glass matrix. Figure 2 (a) shows FTIR spectra of as-prepared glass samples recorded using KBr pellet technique at room temperature.

The band lying between 650 to 400 cm^{-1} arises due to various M-O (metal-oxygen) vibrations (such as Ba-O, Bi-O, V-O, etc.) in glass structure [47,49]. Deconvolution on FTIR spectra was used to get a better idea of different bonds or structural units present inside the sample matrix. It helps to identify different peak positions and their corresponding relative peak areas along with NBO concentration constituting the complete spectrum. Deconvolution of recorded FTIR spectrum was performed using '**Gaussian distribution function**' through '**Origin 9.0**' software. Figure 2(b) shows a deconvoluted FTIR spectra of typical NVBBB(x=5) glass sample (here green line shows constituting peaks and red is fitted one). The observed peak centre and their corresponding bands of origin are given in Table 3. On basis of deconvolution one can suggest that glass structure consists of non-bridging oxygen's alongside different structural units listed in Table 3.

Parameter N_4 helps to identify content of non-bridging oxygen inside the sample matrix via relation discussed below.

$$N_4 = \frac{Area\ under\ peaks\ corresponding\ to\ BO_4\ structural\ units}{Sum\ of\ area\ under\ peaks\ corresponding\ to\ BO_4\ \&\ BO_3\ structural\ units} \quad \text{(vi)}$$

Higher content of the BO_4 structural unit lowers the concentration of non-bridging oxygen and molar volume [27,52]. All the structural modification within glass matrix results variation in non-bridging oxygen's (i.e. NBO's) concentration, which can be analyzed by using change in relative area under BO_4 structural units (i.e. N_4). The inset of Figure 2(a) shows compositional variation of N_4 for prepared glass system. N_4 shows increasing trend (with increase in Nb_2O_5 content) for as-prepared glass samples, resulting in compactness of glass matrix as described by compositional trends in density as well.

3.4 Dielectric Analysis

a) Dielectric constant

Dielectric analysis was performed on the basis of dielectric parameters like real component and imaginary component of dielectric constant, a.c. conductivity, loss tangent, etc. Isothermal curves (at temperature = 350 °C) of ε′ (real component) and ε″ (imaginary component) vs frequency for as-prepared glass samples are exposed in Figures 3(a & b), respectively. There are several factors (such as hoping, ionic rotation around negative sites, etc.) that affect the dielectric permittivity of any material. As per figures, the values of ε′ and ε″ decrease with rise in frequency values (for lower frequency values) and attain saturation at higher frequency region. In lower frequency region, both ε′ and ε″ have higher values, which might be due to domination of polarization and space charge accumulation of charge carriers around glass electrode interface, which restrict the further flow of charge carriers.

With rise in frequency, i.e. a faster periodic reversal in direction of applied electric field, space charge accumulation decreases, resulting in a decrease in values of both ε′ and ε″ [5,19,30,34]. Sample with maximum vanadium content (i.e. NVBBB(x=0)) have highest value of dielectric constant, which decreases on imparting Nb_2O_5 in place of V_2O_5 (which might be due to mixed transition metal effect (MTE)) [53]. Dielectric properties of glass systems are also affected by the concentration of NBO's present inside their glass matrix. Higher is the concentration of NBO's, more easily will the sample be polarized and greater will be its dielectric behaviour [15,16,54]. Samples having lower value of dielectric constant can be used as appropriate materials for high frequency signal transmission devices. For analyzing effect of heat on dielectric constant, we use typical curves (at different temperatures) of ε′ and ε″ vs frequency for NVBBB(x=5) glass sample, as shown in Figures 4 (a & b), respectively. In dispersive region (i.e. region of lower frequency), temperature has a significant effect (due to thermal agitation), which increases space charge polarization, while for higher frequency region, both curves become temperature-independent.

b) Loss tangent (tanδ)

Loss tangent (or dissipation factor) reflects phase difference between applied electric fields and developed electric fields. One can analyze tanδ as ratio of imaginary (ε″) to real (ε′) component of dielectric constant [19,30]. Figure 5(a) shows tanδ vs frequency curves for all as-prepared glass samples at 350 °C. Loss tangent helps to understand energy losses occurring due to various factors such as conduction, relaxation, resonance, etc. In lower frequency region, tanδ has higher value (due to dominance of relaxation phenomena) and its value decreases with increment in frequency [55,56]. Figure 5(b) reflects temperature dependence of tanδ vs frequency curve for typical NVBBB(x=5) glass sample. It can clearly be seen that tanδ follows a similar kind of variation as followed by dielectric loss (ε″). With increase in temperature the thermally accelerated charge carriers cause increase in tanδ values in lower frequency region [30]. The similar kind of behavioural variation is followed by all glass samples.

3.5 ac conductivity (σ_{ac})

The ac conductivity helps to understand how well a material can conduct the alternating current. It depends on various factors, such as frequency of applied field, temperature of material, and impurities inside the material. Figures 6(a & b) are used to understand frequency, compositional and temperature effects on ac conductivity. Figure 6(a) reflects ac conductivity (σ_{ac}) vs frequency curve for all as-prepared glass samples at 350 °C. For lower frequency region, σ_{ac} is almost constant due to charge carriers accumulation at glass-electrode interface, which restricts the flow of charge carriers through interface. With increase in frequency (i.e. periodic reversal of electric field), the space charge accumulation reduces, leads to flow of charge carriers and increase in ac conductivity (σ_{ac}). Glass sample with highest content of vanadium possess highest conductivity in comparison with all prepared glasses. Similar kind of pattern were observed among various researchers (i.e. modification of glass matrix with V_2O_5 results increase in ac conductivity due to hopping of charges between V^{4+} /V^{5+} sites) [34]. As shown in the figure, addition of Nb_2O_5 results decrease in σ_{ac} which may be due to heavier mass of niobium ions (in comparison with vanadium ions) and mixed transition metal effect. Glasses possessing lower ac conductivity can be used for high-voltage operating devices. Figure 6(b) shows σ_{ac} vs frequency curves for typical NVBBB(x=5) glass sample at different temperatures. All as-prepared glass samples show similar temperature and frequency variations. The increase in temperature cause increase in thermal agitation, which reduces the activation energy of charge carriers and increases ac conductivity.

3.6 UV-Vis Spectroscopy

The optical behaviour of as-prepared and annealed glass samples was analyzed through their UV-Vis absorption spectrum. These absorption spectra help in identification of various optical parameters such as cut-off wavelength ($\lambda_{cut\text{-}off}$), optical band-gap (E_g), Urbach energy (ΔE) and refractive index (n). A typical optical absorption spectra of NVBBB(x=5) glass samples (as-prepared and annealed) are shown in Figure 7(a), which helps in determining cut-off wavelength (i.e. $\lambda_{cut\text{-}off}$).

$\lambda_{cut\text{-}off}$ giving idea about the compactness of glass structure as a decrease in $\lambda_{cut\text{-}off}$ value reflects strengthening of bonds in glass matrix [18,20,57]. Observed values of $\lambda_{cut\text{-}off}$ for all as-prepared and annealed glass samples are reported in Table 4. One can observe from this table that addition of Nb_2O_5 in place of V_2O_5 results in a decrease in $\lambda_{cut\text{-}off}$, reflecting strengthening of bonds and compactness in glass network.

Earlier, was noticed that, the indirect optical band-gap plays significant role in optical behaviour of amorphous solids (like glass) [58]. The value of indirect optical band-gap (E_g) (at r=2 and 3) was recorded at energy intercept of extended part of linearly fitted portion (dash line) of $(\alpha h\upsilon)^{1/2}$ & $(\alpha h\upsilon)^{1/3}$ vs $h\upsilon$ (energy) curve. The graphical representation of these curves for typical NVBBB(x=5) sample are shown in Figure 7 (b) and Figure 8(a) respectively. It was observed that all compositions exhibit similar kind of optical behaviour. The obtained values of E_g (at r=2 and 3) for all as-prepared and annealed glass samples are listed in Table 4**.** As can be seen from this Table 4, substitution of Nb_2O_5 with V_2O_5 enhances the optical band-gap value, which might be due to the strengthening of bonds constituting glass matrix [16,37]. The compositional variation of indirect optical band-gap is found to support the predictions made through compositional trends in density and FTIR absorption spectra [18,49,59]. The increase in values of E_g reflects decreasing concentration of localized states within forbidden energy band-gap [20].

Urbach energy *(ΔE)* helps in identification of extent of defects and localized states inside the glass matrix [57,60]. Increase in network defects leads to an increase in localized states, which provides a relatively shorter energy path to ground state electrons for jumping in conduction band [57,60,61]. Urbach energy for all the prepared glass samples is calculated as per Urbach rule [57,60,61] and calculated values are reported in Table 4. The value of Urbach energy for an glass sample was calculated from inverse of slope of linearly fitted portion in $\ln(\alpha)$ vs $h\upsilon$ curve. A typical graphical representation of $\ln(\alpha)$ vs $h\upsilon$ curve for NVBBB(x=5) sample is shown in Figure 8(b). A decrease in ΔE value after annealing reflects the reduced content of defects present in glass matrix or localized states within forbidden energy band-gap.

a) Refractive Index

Refractive index helps to identify the transparency of annealed glass samples (i.e. annealed glass (glass ceramics) will be called as transparent glass ceramics if they have similar value of refractive index with glass). Refractive indices for any glass sample may effect by various factors such as coordination number of oxide ions, concentration of NBOs, optical basicity, etc. [39,62]. Refractive indices for all the prepared samples (as-prepared and annealed once) were calculated through optical band-gap value (E_g) (for r=2) via relation 'vii' and reported in Table 4.

$$\frac{n^2-1}{n^2+2} = 1 - \sqrt{\frac{E_g}{20}} \qquad \text{(vii)}$$

Addition of Nb_2O_5 to the glass matrix decreases refractive indices for as-prepared glass samples, reflecting a decrease in polarization and NBO's for prepared glass system. The similar values of refractive index for annealed glass samples reflect their transparent nature. On the basis of recorded values of crystallite size and refractive index, we can say that sample NVBBB(x=3) can be treated as useful material for transparent glass ceramics (TGC).

3.7 Differential Thermal Analysis (DTA)

DTA curves help to analyze thermal properties and characteristic temperatures (such as glass transition (T_g), peak (T_c) and onset (T_x) crystallization temperatures) for as-prepared glass samples [20]. Figure 9 contains, graphical representation of DTA curve for typical NVBBB(x=5) as-prepared glass sample. It was observed that all as-prepared glass samples follow similar kind of DTA curves along with their different characteristic temperatures as reported in Table 5. The existence of an endothermic shift in DTA curves for all glass samples reflects the glassy nature of each glass samples. From this table, we can generalize that the addition of Nb_2O_5 to the glass matrix, increases glass transition (T_g), peak crystallization (T_c) temperature and thermal stability. This increase in glass transition temperature reflects enhanced bond strength and compactness of glass network which was also favored by UV-Vis spectroscopy. The existence of exothermic peak reflects nucleation ability of glasses. The decrease in T_c on addition of TMI's suggests their increasing availability as nucleating agents.

4. Conclusion

Barium-boro-bismuthate glasses modified with Nb_2O_5 and V_2O_5 having composition $x$$Nb_2O_5$-(10-$x$)$V_2O_5$-25BaO-30$B_2O_3-35Bi_2O_3$ (where x = 0, 1, 3, 5, 8, 9 & 10 mol%) were prepared via melt-quench technique and abbreviated as NVBBBx (where x = 0, 1, 3, 5, 7, 9 and 10). XRD profiles of as-prepared and annealed glass samples, confirms their amorphous and crystalline nature (along with development of nano-crystallites in annealed glass matrix) respectively. FTIR spectroscopy indicates existence of BO_3, BO_4, BiO_3 and BiO_6, structural units along with non-bridging oxygen's. The optical, electrical and thermal analysis of as-prepared glass samples were analyzed via Uv-Vis, Impedance spectroscopy and Differential Thermal analysis respectively. The lower values of dielectric constant reflect their usability as appropriate materials for high frequency signal transmission devices. The lower value of ac conductivity ($\sigma_{ac} \sim 10^{-5}$ S/m), suggests their availability for high temperature semiconducting devices. $\lambda_{cut\text{-}off}$ of as-prepared glass samples decreases on replacement of V_2O_5 with Nb_2O_5, reflecting strengthening of bonds present inside the glass samples. The optical band-gap of as-prepared glass samples (ranging from 1.13 to 1.92 eV) increases on substitution of Nb_2O_5 in place of V_2O_5. These values reflect, their applicability in various fields such as infrared photo-detectors, thermo-, opto-electronics. The small increase in optical band-gap after annealing reflects a strengthening of bonds within the glass matrix and non-significant change in glass structure after annealing (i.e. crystallites developed are in very small portion). Refractive index values of as-prepared and annealed glass samples reflect that annealed glasses can be treated as transparent glass ceramics, whereas samples NVBBB(x=3) are good transparent ceramic materials among all prepared samples. The sharp exothermic curve in DTA thermogram reflects the nucleating and crystallization abilities of as-prepared glass samples. The decrease in T_c values reflects that transition metal ions present inside the glass matrix act as nucleating agents.

Acknowledgements

The authors express their gratitude to DST Delhi for furnishing experimental support under the FIST Research Grant (Sanction Order No. & Date: SR/FST/PS-1/2018/32). The Central Instrumentation Laboratory (CIL) of Deenbandhu Chhotu Ram University of Science and Technology, Murthal, is acknowledged by the authors for providing FTIR facilities. Author, Vikas Attri, expresses gratitude to UGC, New Delhi, for the financial support granted under JRF Fellowship F. No.-16-9(June 2018)/2019(NET/CSIR).

References:

[1] C.R. Gautam, D. Kumar, O. Parkash, P. Singh, Synthesis, IR, crystallization and dielectric study of (Pb, Sr)TiO 3 borosilicate glass-ceramics, Bull. Mater. Sci. 36 (2013) 461–469. https://doi.org/10.1007/s12034-013-0489-5.

[2] O.I. Sallam, A.M. Madbouly, N.A. Elalaily, F.M. Ezz-Eldin, Physical properties and radiation shielding parameters of bismuth borate glasses doped transition metals, J. Alloys Compd. 843 (2020) 156056. https://doi.org/10.1016/j.jallcom.2020.156056.

[3] H.H. Hegazy, M.S. Al-Buriahi, F. Alresheedi, S. Alraddadi, H. Arslan, H. Algarni, The Effects of TeO2 on Polarizability, Optical Transmission, and Photon/Neutron Attenuation Properties of Boro-Zinc-Tellurite Glasses, J. Inorg. Organomet. Polym. Mater. 31 (2021) 2331–2338. https://doi.org/10.1007/s10904-021-01933-2.

[4] M.S. Al-Buriahi, E.M. Bakhsh, B. Tonguc, S.B. Khan, Mechanical and radiation shielding properties of tellurite glasses doped with ZnO and NiO, Ceram. Int. 46 (2020) 19078–19083. https://doi.org/10.1016/j.ceramint.2020.04.240.

[5] A. Yadav, M.S. Dahiya, P. Narwal, A. Hooda, A. Agarwal, S. Khasa, Electrical characterization of lithium bismuth borate glasses containing cobalt/vanadium ions, Solid State Ionics. 312 (2017) 21–31. https://doi.org/10.1016/j.ssi.2017.10.006.

[6] H. Doweidar, Y.B. Saddeek, FTIR and Ultrasonic Investigations on Modified Bismuth Borate Glasses, J. Non. Cryst. Solids. 355 (2009) 348–354. https://doi.org/10.1016/j.jnoncrysol.2008.12.008.

[7] S. Bhattacharya, H.D. Shashikala, Effect of BaO on thermal and mechanical properties of alkaline earth borosilicate glasses with and without Al2O3, Phys. B Condens. Matter. 571 (2019) 76–86. https://doi.org/10.1016/j.physb.2019.06.065.

[8] Y.-H. Kao, Y. Hu, H. Zheng, J.D. Mackenzie, K. Perry, G. Bourhill, J.W. Perry, Second harmonic generation in transparent barium borate glass-ceramics, J. Non. Cryst. Solids. 167 (1994) 247–254.

[9] P. Bergo, W.M. Pontuschka, J.M. Prison, C.C. Motta, Investigation of some dielectric properties of phosphate glasses doped with iron oxides , by a microwave technique, Measurement. 43 (2010) 210–215. https://doi.org/10.1016/j.measurement.2009.09.007.

[10] V. Bhatia, D. Kumar, H. Singh, N. Kaur, S.M. Rao, A. Kumar, V. Mehta, S.P. Singh, Structural, optical and thermoluminescence properties of newly developed MnKB: Er3+ glass system, J. Non. Cryst. Solids. 543 (2020) 120113. https://doi.org/10.1016/j.jnoncrysol.2020.120113.

[11] M.S. Dahiya, S. Khasa, A. Yadav, A. Agarwal, Appearance of small polaron hopping conduction in iron modified cobalt lithium bismuth borate glasses, AIP Conf. Proc. 1731 (2016) 3–6. https://doi.org/10.1063/1.4947850.

[12] P. Syam Prasad, V. Himamaheswara Rao, M. Mohan Babu, P. Venkateswara Rao, G. Naga Raju, C. Laxmikanth, Spectroscopic investigations of the PbO-MoO3-P2O5:V2O5 glass system, Phys. Chem. Glas. Eur. J. Glas. Sci. Technol. Part B. 56 (2015) 169–174. https://doi.org/10.13036/17533562.56.4.169.

[13] S. Sanghi, A. Sheoran, A. Agarwal, S. Khasa, Conductivity and dielectric relaxation in niobium alkali borate glasses, Phys. B Condens. Matter. 405 (2010) 4919–4924. https://doi.org/10.1016/j.physb.2010.09.032.

[14] A. El-Denglawey, M. Ahmad, K. Aly, Y.B. Saddeek, A. Dahshan, A study of thermal parameters of some alkali boro-bismuthate glasses, J. Mater. Sci. Mater. Electron. 32 (2021) 23614–23623. https://doi.org/10.1007/s10854-021-06850-1.

[15] S. Rani, S. Sanghi, A. Agarwal, S. Khasa, Influence of Nb2O5 on the optical band gap and electrical conductivity of Nb2O5·BaO·B 2O3, IOP Conf. Ser. Mater. Sci. Eng. 2 (2009) 2–6. https://doi.org/10.1088/1757-899X/2/1/012041.

[16] S. Sanghi, S. Rani, A. Agarwal, V. Bhatnagar, Influence of Nb2O5 on the structure, optical and electrical properties of alkaline borate glasses, Mater. Chem. Phys. 120 (2010) 381–386. https://doi.org/10.1016/j.matchemphys.2009.11.016.

[17] N. Gupta, A. Khanna, Glass and anti-glass phase co-existence and structural transitions in bismuth tellurite and bismuth niobium tellurite systems, J. Non. Cryst. Solids. 481 (2018) 594–603. https://doi.org/10.1016/j.jnoncrysol.2017.12.002.

[18] Vikas, M.S. Dahiya, A. Hooda, S. Khasa, Structural analysis of mixed transition metal ion doped barium-boro-bismuthate glass system, J. Mol. Struct. 1264 (2022) 133291. https://doi.org/10.1016/j.molstruc.2022.133291.

[19] V. Attri, S. Khasa, Structural, Electrical and Optical Analysis of Barium Boro-Bismuthate Glass System: Opto-Electronic Devices, ECS Trans. 107 (2022) 10957–10967. https://doi.org/10.1149/10701.10957ecst.

[20] V. Attri, M.S. Dahiya, R. Kumar, A. Hooda, A. Agarwal, S. Khasa, Electrical, optical and high energy radiation shielding study of TMI-doped multi-component glasses, J. Mater. Sci. Mater. Electron. 34 (2023) 1–16. https://doi.org/10.1007/s10854-023-10625-1.

[21] K.S. Shaaban, N. Tamam, H.A. Alghasham, Z.A. Alrowaili, M.S. Al-buriahi, T.E. Ellakwa, Thermal , optical , and radiation shielding capacity of B 2 O 3 -MoO 3 -Li 2 O-Nb 2 O 5 glasses, 37 (2023). https://doi.org/10.1016/j.mtcomm.2023.107325.

[22] G. Upender, M. Prasad, Optik Vibrational , Optical and EPR studies of TeO 2 -Nb 2 O 5 -Al 2 O 3 -V 2 O 5 glass system doped with vanadium, 127 (2016) 10716–10726.

[23] G.S. Murugan, T. Suzuki, Y. Ohishi, Raman spectroscopic studies of quaternary tellurite glasses containing Nb2O5 and Ta2O5, Phys. Chem. Glas. 46 (2005) 359–364.

[24] Anshu, S. Sanghi, A. Agarwal, M. Lather, V. Bhatnagar, S. Khasa, Structural investigations of vanadyl doped Nb2O5·K2O·B2O3 glasses, IOP Conf. Ser. Mater. Sci. Eng. 2 (2009). https://doi.org/10.1088/1757-899X/2/1/012054.

[25] N. Elkhoshkhany, E. Syala, Detailed study about the thermal behavior and kinetics characterization of an oxyfluoride tellurite glass, J. Non. Cryst. Solids. 486 (2018) 19–26. https://doi.org/10.1016/j.jnoncrysol.2018.02.008.

[26] W. Holand, G.H. Beall, Glass-ceramic technology, Wiley, United Kingdom, 2019.

[27] A. Yadav, M.S. Dahiya, A. Hooda, P. Chand, S. Khasa, Structural influence of mixed transition metal ions on lithium bismuth borate glasses, Solid State Sci. 70 (2017) 54–65. https://doi.org/10.1016/j.solidstatesciences.2017.06.011.

[28] M. Rezvani, B. Eftekhari-Yekta, M. Solati-Hashjin, V.K. Marghussian, Effect of Cr2O3, Fe2O3 and TiO2 nucleants on the crystallization behaviour of SiO 2-Al2O3-CaO-MgO(R2O) glass-ceramics, Ceram. Int. 31 (2005) 75–80. https://doi.org/10.1016/j.ceramint.2004.03.037.

[29] A. Chakrabarti, A.R. Molla, Synthesis of Eu2O3 doped BaO-TiO2-GeO2 based glass-ceramics: Crystallization kinetics, optical and electrical properties, J. Non. Cryst. Solids. 505 (2019) 354–366. https://doi.org/10.1016/j.jnoncrysol.2018.11.002.

[30] M. Malik, S. Dagar, A. Hooda, A. Agarwal, S. Khasa, Effect of magnetic ion, Fe3+ on the structural and dielectric properties of Oxychloro Bismuth Borate Glasses, Solid State Sci. 110 (2020) 106491. https://doi.org/10.1016/j.solidstatesciences.20

20.106491.

[31] D. Holland, A. Mekki, I.A. Gee, C.F. McConville, J.A. Johnson, C.E. Johnson, P. Appleyard, M. Thomas, Structure of sodium iron silicate glass - a multi-technique approach, J. Non. Cryst. Solids. 253 (1999) 192–202. https://doi.org/10.1016/S0022-3093(99)00353-1.

[32] L.S. Rao, M.S. Reddy, M.R. Reddy, N. Veeraiah, Dielectric dispersion in Li2O-MoO3-B2O3 glass system doped with V2O5, J. Alloys Compd. 464 (2008) 472–482. https://doi.org/10.1016/j.jallcom.2007.10.016.

[33] M.S. Dahiya, S. Khasa, A. Agarwal, Structural, Optical and Thermal Properties of Transition Metal Ions Doped Bismuth Borate Glasses, Phys. Chem. Glas. Eur. J. Glas. Sci. Technol. Part B. 57 (2016) 45–52. https://doi.org/10.13036/17533562.57.2.023.

[34] A. Yadav, S. Khasa, A. Hooda, M.S. Dahiya, A. Agarwal, P. Chand, EPR and impedance spectroscopic investigations on lithium bismuth borate glasses containing nickel and vanadium ions, Spectrochim. Acta - Part A Mol. Biomol. Spectrosc. 157 (2016) 129–137. https://doi.org/10.1016/j.saa.2015.12.027.

[35] A. Yadav, S. Khasa, M.S. Dahiya, A. Agarwal, Nano crystalline Bi2(VO5) phases in lithium bismuth borate glasses containing mixed vanadium-nickel oxides, AIP Conf. Proc. 1731 (2016) 5–8. https://doi.org/10.1063/1.4947851.

[36] A. Yadav, S. Khasa, A. Hooda, M.S. Dahiya, A. Agarwal, P. Chand, EPR and impedance spectroscopic investigations on lithium bismuth borate glasses containing nickel and vanadium ions, Spectrochim. Acta Part A Mol. Biomol. Spectrosc. 157 (2016) 129–137. https://doi.org/10.1016/j.saa.2015.12.027.

[37] S. Khasa, M. Dahiya, A. agarwal, Structural Investigations of Lithium Vanadoxide Bismo-Borate Glasses, J. Integr. Sci. Technol. 1 (2013) 44–47. http://www.pubs.iscience.in/journal/index.php/jist/article/view/48.

[38] A. Bajaj, A. Khanna, B. Chen, J.G. Longstaffe, U. Zwanziger, J.W. Zwanziger, Y. Gomez, F. Gonzalez, Structural investigation of bismuth borate glasses and crystalline phases, J. Non. Cryst. Solids. 355 (2009) 45–53. https://doi.org/10.1016/j.jnoncrysol.2008.09.033.

[39] M. Abdel-baki, F.A. Abdel-wahab, A. Radi, F. El-diasty, Factors affecting optical dispersion in borate glass systems, J. Phys. Chem. Solids. 68 (2007) 1457–1470. https://doi.org/10.1016/j.jpcs.2007.03.026.

[40] S. Rada, P. Pascuta, M. Bosca, M. Culea, L. Pop, E. Culea, Structural properties of the boro-bismuthate glasses containing gadolinium ions, Vib. Spectrosc. 48 (2008) 255–258. https://doi.org/10.1016/j.vibspec.2007.12.005.

[41] M.S. Dahiya, Meenakshi, A. Shankar, A. Agarwal, S. Khasa, On the role of ZnO on properties of vitreous bismuth silicates, J. Alloys Compd. 696 (2017) 688–696. https://doi.org/10.1016/j.jallcom.2016.11.285.

[42] M.S. Dahiya, S. Khasa, A. Agarwal, Thermal characterization of novel magnesium oxyhalide bismo-borate glass doped with VO2+ ions, J. Therm. Anal. Calorim. 123 (2016) 457–465. https://doi.org/10.1007/s10973-015-4913-5.

[43] G.A. Sycheva, Crystal Growth and Nucleation in Glasses in the Lithium Silicate System, J. Cryst. Process Technol. 6 (2016) 29–55. https://doi.org/10.4236/jcpt.2016.64004.

[44] R. Casasola, J.M. Rincón, M. Romero, Glass-ceramic glazes for ceramic tiles: A review, J. Mater. Sci. 47 (2012) 553–582. https://doi.org/10.1007/s10853-011-5981-y.

[45] M. Romero, M. Kovacova, J.M. Rincón, Effect of particle size on kinetics crystallization of an iron-rich glass, J. Mater.

Sci. 43 (2008) 4135–4142. https://doi.org/10.1007/s10853-007-2318-y.

[46] S. Dagar, P. Sharma, S. Khasa, Structural refinement and DC conductivity of cobalt doped copper ferrite Structural Refinement and DC Conductivity of Cobalt Doped Copper Ferrite, 030132 (2020) 0–4.

[47] S. Khasa, M.S. Dahiya, A. Agarwal, FTIR studies of some vanadyl ion doped calcium oxychloride borate glasses, AIP Conf. Proc. 1536 (2013) 671–672. https://doi.org/10.1063/1.4810405.

[48] M.S. Dahiya, S. Khasa, A. Agarwal, Physical, thermal, structural and optical absorption studies of vanadyl doped magnesium oxy-chloride bismo-borate glasses, J. Asian Ceram. Soc. 3 (2015) 206–211. https://doi.org/10.1016/j.jascer.2015.02.006.

[49] A. Yadav, S. Khasa, M.S. Dahiya, S. Dalal, A. Hooda, A. Agarwal, Synthesis, thermal and spectroscopic characterization of lithium bismuth borate glasses containing mixed transition metal ions, Phys. Chem. Glas. Eur. J. Glas. Sci. Technol. Part B. 57 (2016) 146–152. https://doi.org/10.13036/17533562.57.3.018.

[50] P. Narwal, M.S. Dahiya, A. Yadav, A. Hooda, A. Agarwal, S. Khasa, Dy3+ doped LiCl–CaO–Bi2O3–B2O3 glasses for WLED applications, Ceram. Int. 43 (2017) 11132–11141. https://doi.org/10.1016/j.ceramint.2017.05.160.

[51] S. Khasa, M.S. Dahiya, A. Agarwal, P. Chand, EPR , FTIR , Thermal and Electrical Properties of VO 2 + doped BaCl2.BaO.B2O3 Glasses, J. Mol. Struct. 1079 (2015) 15–20. https://doi.org/10.1016/j.molstruc.2014.09.012.

[52] P. Narwal, M.S. Dahiya, A. Yadav, A. Hooda, A. Agarwal, S. Khasa, Improved white light emission in Dy3+ doped LiF–CaO–Bi2O3–B2O3 glasses, J. Non. Cryst. Solids. 498 (2018) 470–479. https://doi.org/10.1016/j.jnoncrysol.2018.01.042.

[53] B. Dutta, N.A. Fahmy, I.L. Pegg, Effect of mixed transition-metal ions in glasses . Part III : The P 2 O 5 – V 2 O 5 – MnO system, 352 (2006) 2100–2108. https://doi.org/10.1016/j.jnoncrysol.2006.02.043.

[54] F.A. Abdel-Wahab, A.M. Fayad, M.Abdel-Baki, H. Abdel-Maksoud, Role of non-bridging oxygen defect in the ionic conductivity and associated oxygen trap centers in lead-borate oxide glass: Effect of structural substitution of PbO for Ag2O and Li2O modifier, J. Non. Cryst. Solids. 500 (2018) 84–91. https://doi.org/10.1016/j.jnoncrysol.2018.06.033.

[55] A.S. Hassanien, I. Sharma, Dielectric properties, Optoelectrical parameters and electronic polarizability of thermally evaporated a-Pb-Se-Ge thin films, Phys. B Condens. Matter. 622 (2021) 413330. https://doi.org/10.1016/j.physb.2021.413330.

[56] A.S. Hassanien, Studies on dielectric properties, opto-electrical parameters and electronic polarizability of thermally evaporated amorphous Cd50S50-xSex thin films, J. Alloys Compd. 671 (2016) 566–578. https://doi.org/10.1016/j.jallcom.2016.02.126.

[57] M.S. Dahiya, A. Yadav, N. Manyani, S. Chahal, A. Hooda, A. Agarwal, S. Khasa, Fe-substituted Co-Li bismuth borate glasses: Crystallization kinetics and optical absorption, J. Therm. Anal. Calorim. 126 (2016) 1191–1199. https://doi.org/10.1007/s10973-016-5622-4.

[58] M.S. Dahiya, A. Agarwal, S. Khasa, Compositional Dependence of Optical Absorption in Barium Oxychloride Borate Glasses, J. Adv. Phys. 6 (2016) 116–120. https://doi.org/10.1166/jap.2017.1302.

[59] S. Thakur, V. Thakur, A. Kaur, L. Singh, Structural, Optical and Thermal Properties of Nickel Doped Bismuth Borate

Glasses, J. Non. Cryst. Solids. 512 (2019) 60–71. https://doi.org/10.1016/j.jnoncrysol.2019.02.012.

[60] J.I. Pankove, Optical Processes in Semiconductors, Dover Publications, New York, 1975.

[61] M. Elahi, D. Souri, Study of optical absorption and optical band gap determination of thin amorphous TeO2-V2O5-MoO3 blown films, Indian J. Pure Appl. Phys. 44 (2006) 468–472.

[62] E.S. Yousef, B. Al-Qaisi, UV Spectroscopy, Refractive Indices and Elastic Properties of the (76-x)TeO2.9P2O5.15ZnO.xLiNbO3 Glass, Solid State Sci. 19 (2013) 6–11. https://doi.org/10.1016/j.solidstatesciences.2013.01.014.

[63] P. Pascuta, M. Bosca, S. Rada, M. Culea, I. Bratu, E. Culea, FTIR spectroscopic study of Gd2O3-Bi 2O3-B2O3 glasses, J. Optoelectron. Adv. Mater. 10 (2008) 2416–2419.

[64] Y.B. Saddeek, K.A. Aly, K.S. Shaaban, A.M. Ali, M.M. Alqhtani, A.M. Alshehri, M.A. Sayed, E.A. Abdel Wahab, Physical properties of B2O3–TeO2–Bi2O3 glass system, J. Non. Cryst. Solids. 498 (2018) 82–88. https://doi.org/10.1016/j.jnoncrysol.2018.06.002.

[65] V. Dimitrov, Y. Dimitriev, A. Montenero, IR spectra and structure of VzO5-GeOe-Bi203 glasses, J. Non. Cryst. Solids. 180 (1994) 51–57. https://doi.org/10.1016/0022-3093(94)90396-4.

[66] I. Ardelean, S. Cora, D. Rusu, EPR and FT-IR spectroscopic studies of Bi2O3- B 2O3-CuO glasses, Phys. B Condens. Matter. 403 (2008) 3682–3685. https://doi.org/10.1016/j.physb.2008.06.016.

Figures

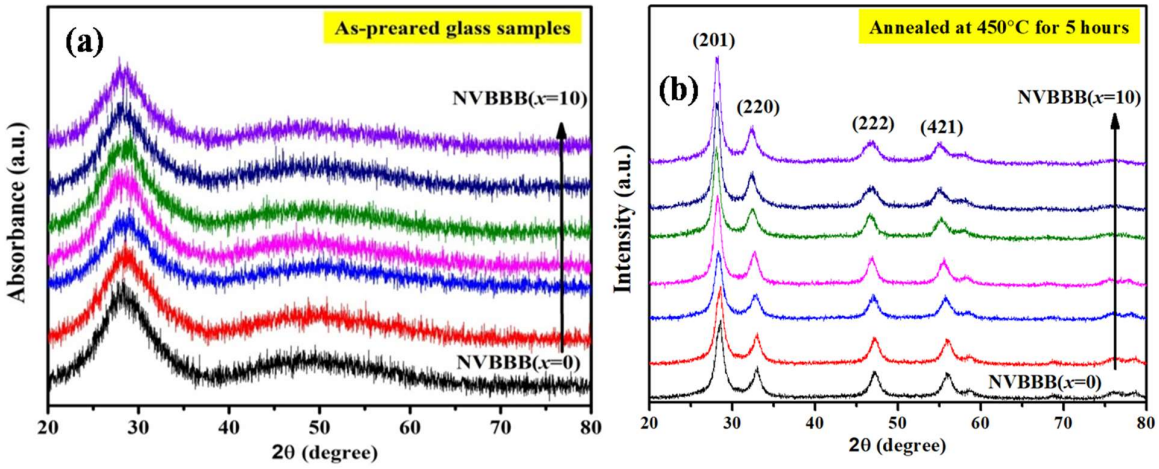

Figure 1. XRD profiles of NVBBB glass system (a) for as-prepared; (b) annealed ones

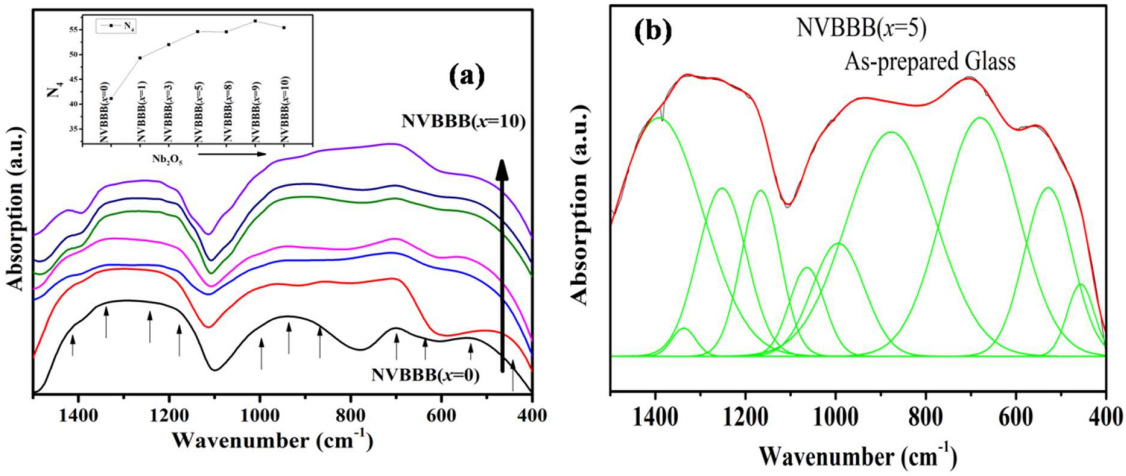

Figure 2. (a) FTIR spectra for all NVBBB glass systems (inset shows N_4 variation for all glasses),

(b) A deconvoluted FTIR spectrum of typical NVBBB(x=5) as-prepared glass sample.

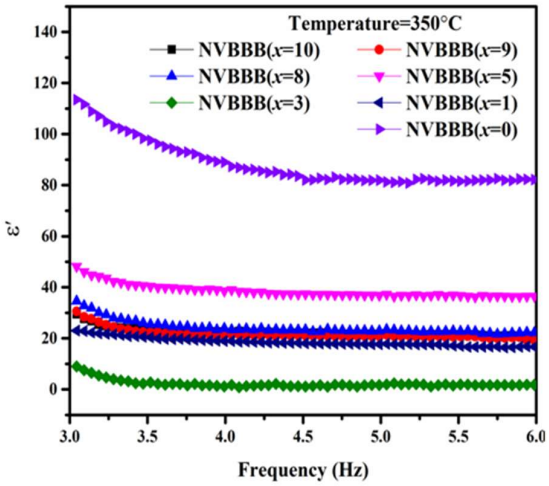

Figure 3. (a) ε′ vs frequency curve for as-prepared NVBBB glass samples at 350°C.

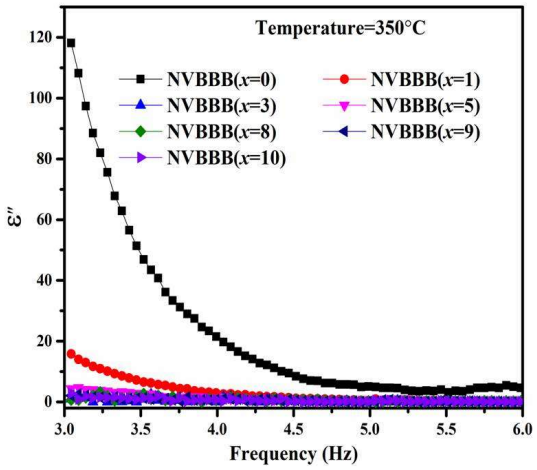

Figure 3 (b) ε″ vs frequency curve for NVBBB glass samples at 350 °C.

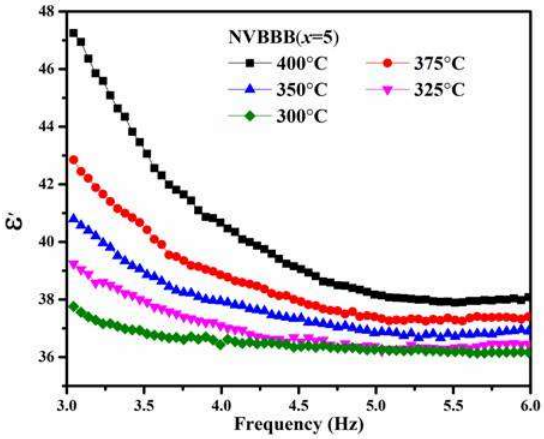

Figure 4. (a) ε′ vs frequency for NVBBB(*x*=5) glass sample at different temperatures

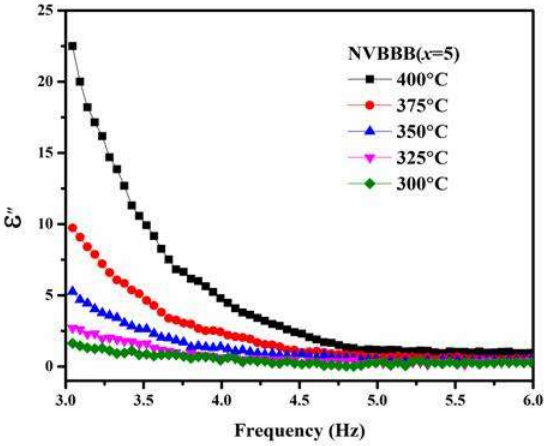

Figure 4. (b) ε″ vs frequency curve for NVBBB(*x*=5) glass sample at different temperatures.

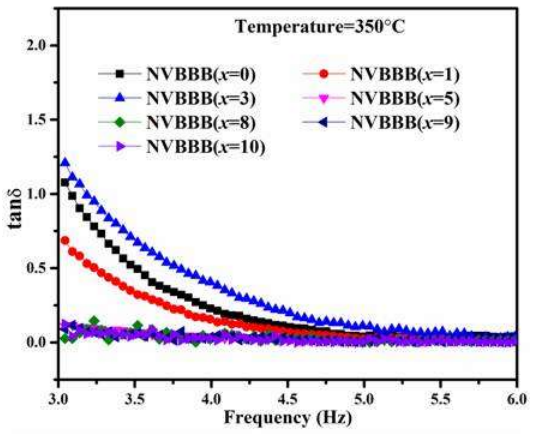

Figure 5. (a) tanδ vs frequency curves for NVBBB glass samples at 350°C

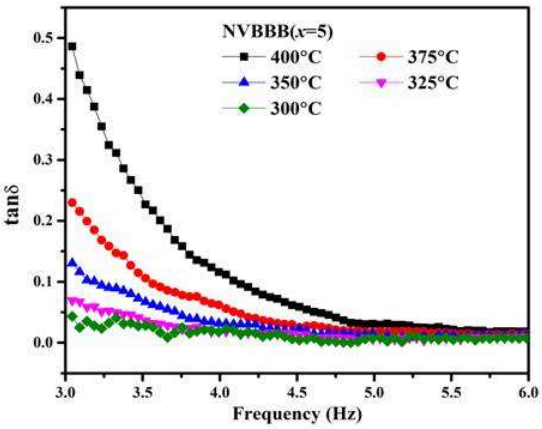

Figure 5. (b) Temperature dependence of tanδ vs frequency curve for NVBBB(*x*=5) glass sample

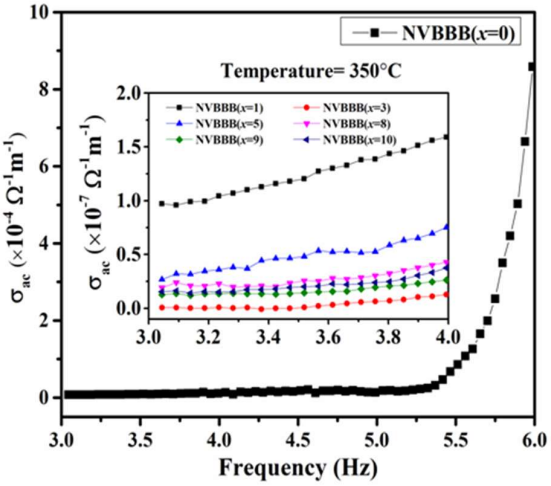

Figure 6. (a) σ_{ac} vs frequency curves for NVBBB glass system at 350°C

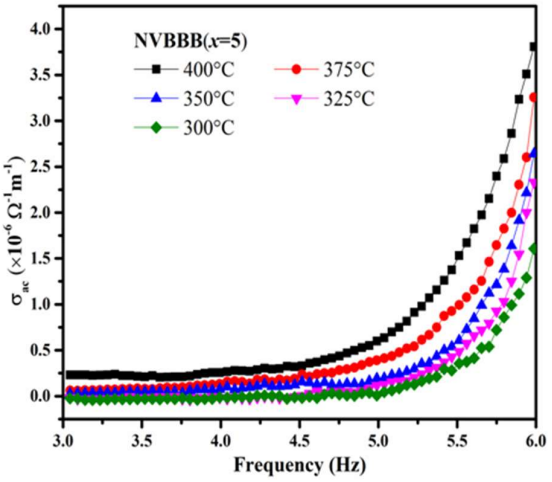

Figure 6. (b) Temperature dependence of σ_{ac} vs frequency curve for NVBBB(*x*=5) glass sample

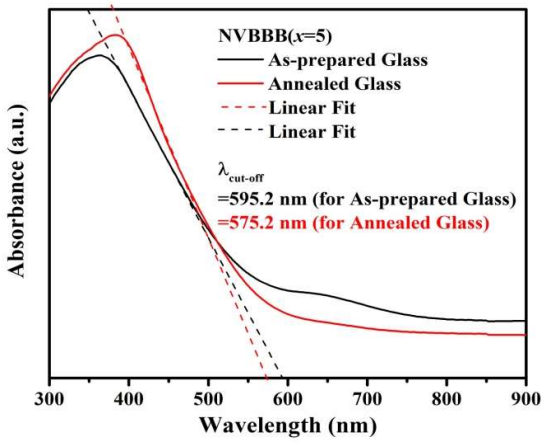

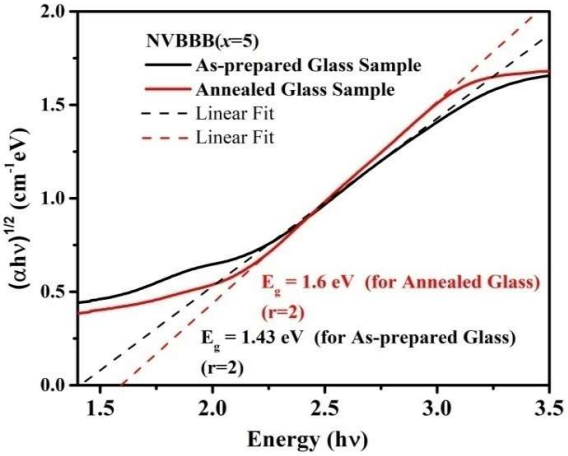

Figure 7. (a) A typical absorption spectra for NVBBB(*x*=5) as-prepared and annealed glass sample

Figure 7. (b) A typical $(\alpha h\nu)^{1/2}$ vs energy curves for NVBBB(*x*=5) as-prepared and annealed glass samples at room temperature

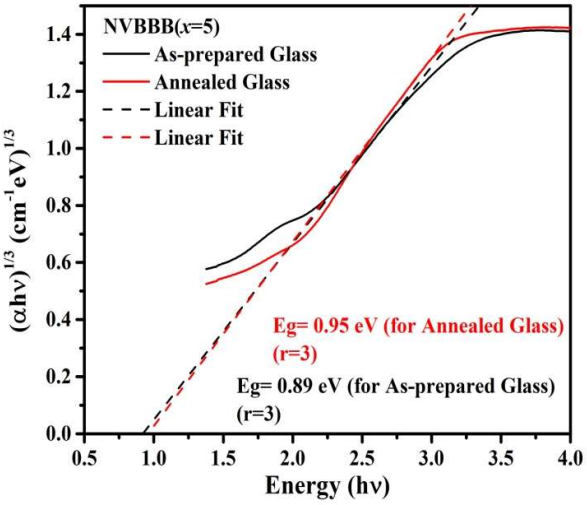

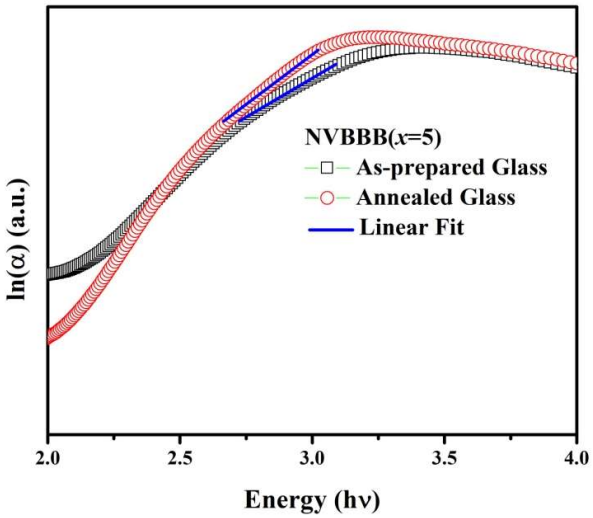

Figure 8. (a) A typical $(\alpha h\upsilon)^{1/3}$ vs Energy (hυ) curve for NVBBB(*x*=5) as-prepared and annealed glass sample

Figure 8. (b) A typical ln(α) vs Energy (hυ) curve for NVBBB(*x*=5) as-prepared glass sample

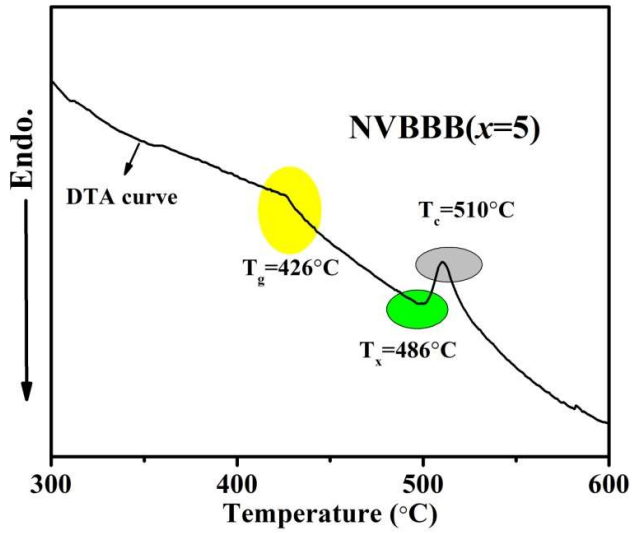

Figure 9. DTA curve for NVBBB(*x*=5) as-prepared glass samples

Tables

Table 1: Density (ρ), Molar Volume (V_m), Oxygen Packing Density (OPD) for NVBBB as-prepared glass systems

Sample	ρ (g/cc)	V_m (cm^3)	OPD (cm^{-3})
NVBBB(x=0)	5.50	45.30	59.59
NVBBB(x=1)	5.52	45.29	59.61
NVBBB(x=3)	5.54	45.43	59.43
NVBBB(x=5)	5.64	44.92	60.10
NVBBB(x=8)	5.63	45.44	59.47
NVBBB(x=9)	5.71	44.96	60.10
NVBBB(x=10)	5.69	45.26	59.64

Table 2: Structural parameters like Crystallite size (D), inter planer spacing (d), lattice parameters (a,b,c), Volume calculated ($V_{cal.}$), Volume given (V_{given}) and strain inside developed crystalline phase of NVBBB annealed glass matrix.

Sample Name	D (nm)	d (nm)	$a=b$ (A^o)	c (A^o)	V_{cal} $(A^o)^3$	V_{given} $(A^o)^3$	Strain
NVBBB(x=0)	6.83	1.109	3.14	1.58	15.578	336.51	0.953
NVBBB(x=1)	6.82	1.108	3.14	1.56	15.381	336.51	0.954
NVBBB(x=3)	6.64	1.112	3.16	1.57	15.677	336.51	0.953
NVBBB(x=5)	6.28	1.107	3.13	1.57	15.381	336.51	0.954
NVBBB(x=8)	5.58	1.103	3.12	1.56	15.186	336.51	0.955
NVBBB(x=9)	5.59	1.097	3.11	1.55	14.991	336.51	0.955
NVBBB(x=10)	5.59	1.097	3.12	1.55	15.088	336.51	0.955

Table 3: Peak centre and their corresponding band of origin for NVBBB glass system

Peak Centre (Wavenumber (cm^{-1}))	Assignment/ band of origin [Refs.]
~470	Vibrations due to metal cations [27,47–51]
~540	Vibrations in Bi-O bonds in BiO_6 structural units [45–48]
~690	Bending vibrations in B-O-B bonds of Borate network [51,63]
~880	Bi-O stretching vibrations in BiO_3 structural units [64–66]
~970	Stretching vibrations in B-O bonds of BO_4 structural units from tri-, tetra- & penta- borate groups [63]
~1165	Stretching vibrations in B-O bond in BO_3 structural units [47,51,63]
~1350	Asymmetric stretching vibrations in B-O bonds from BO_3 structural units [63,66]

Table 4: Optical parameters such as Cut-off wavelength ($\lambda_{cut\text{-}off}$), indirect optical band-gap (E_g) (for r=2 & 3), Urbach energy (ΔE) and refractive index (n) for NVBBB (as-prepared and annealed) glass samples.

As-prepared Glass Samples					
Sample code	$\lambda_{cut\text{-}off}$ *(nm)*	E_g *(eV) (r=2)*	E_g *(eV) (r=3)*	ΔE *(eV)*	n
NVBBB(x=0)	636.3	1.13	0.46	0.69	3.26
NVBBB(x=1)	630.2	1.21	0.60	0.84	3.19
NVBBB(x=3)	622.0	1.34	0.70	0.72	3.09
NVBBB(x=5)	595.2	1.43	0.89	0.67	3.04
NVBBB(x=8)	542.5	1.53	0.91	0.75	2.97
NVBBB(x=9)	513.7	1.67	1.03	0.74	2.89
NVBBB(x=10)	490.5	1.92	1.37	0.68	2.77
Annealed Glass Samples					
NVBBB(x=0)	606.3	1.35	0.61	0.37	3.09
NVBBB(x=1)	615.3	1.39	0.69	0.38	3.06
NVBBB(x=3)	585.5	1.40	0.81	0.46	3.05
NVBBB(x=5)	575.2	1.60	0.95	0.46	2.93
NVBBB(x=8)	534.5	1.72	1.17	0.52	2.83
NVBBB(x=9)	519.5	1.78	1.45	0.53	2.84
NVBBB(x=10)	517.5	1.85	1.41	0.56	2.80

Table 5: List of characteristic temperatures like T_g, T_x,and T_c and thermal stability (T_s) for NVBBB glass samples.

Sample Code	T_g *(± 2 ℃)*	T_x *(± 2 ℃)*	T_c *(± 2 ℃)*	T_s *(± 2 ℃)*
NVBBB(x=1)	420	480	502	82
NVBBB(x=5)	426	486	510	84
NVBBB(x=8)	428	497	513	85

CNS&E

Current Natural Sciences & Engineering